Decay spectroscopy of ^{253}No using the GABRIELA setup

Trine Wiborg Hagen
Department of Physics
University of Oslo
August, 2010

Dissertation presented for the degree of
Master in Physics

Working on this thesis for the last year and a half has been a process I have found interesting, challenging and thoroughly enjoyable. This, I think, is manly due to the people around me: always willing to offer help and assistance when needed, or a pat on the back and getting my mind onto something else at times when the work has not gone as smoothly.

I have been incredibly lucky with my thesis project. I have had the best supervisors I could ask for, and quite a few of you when it comes down to it. Well, guess it takes a village... Wealy, you really have been amazing. I have learned so much from you. Thank you for your patience and for not letting me taking the easy way out. I really have appreciated the kindness both you and Karl have shown me. Sunniva, Ann-Cecilie and Magne, thank you for your feedback, help and for always having open doors.

I have been lucky to have had the opportunity to travel a bit. I have really enjoyed these trips for many reasons, but what really has made them memorable are the people I have met. I have felt welcome and accepted, even being a blue-eyed noob and all. I've had some good times, and really appreciate having gotten to know you all; and Julien, you (and Dorota) really made Dubna fun [1].

Now, Bailey, you been a tremendous help, really. Thank you! And Alexander, you are now and will always be my ROOT guru; takk for all hjelpen.

Though it has been amazing working on this, it also has been nice to get away from it all from time to time. So, friends, family and football-team, thanks for letting me vent and getting me to think of other things. And speaking of distractions, having been able to work a bit as well has been really good for me, so Ole, thanks for being so understanding (and letting me more or less dictate my own hours).

[1] ... and I do not think many people would in general agree with me in that assessment of the place after spending that many weeks there.

Contents

List of Figures

List of Tables

Chapter 1

Introduction

One of the few questions fascinating mankind for the last thousands of years concerns the matter that makes up this world. In earlier time, from several hundred years BC, until the 18th century, this topic was based on philosophical considerations. Empedocles theorized around 450 BC that all matter consisted of units of earth, water, wind and fire, a view later supported and popularized by Aristotle's (384-322 BC). While the view of matter consisting of various degrees of the four elements was by far the dominant, another theory had been presented by Democritus in the 5th century BC. This theory did not obtain a significant following and was nearly forgotten until the 16th century. Democritus claimed that matter around us consisted of small invisible pieces, called atoms, that could be put together in different combinations with different life spans. The atoms in themselves, were indivisible with no room between and infinite in types, both with respect to shape and size. Hundreds of years passed from Democritus predictions before the idea of atoms again was paid any notice. A somewhat more modern atom theory was presented by John Dalton in 1807, and at the end of the 18th century both the electron and a positively charged particle, later named the proton by Rutherford, were discovered[1]. In 1911 Rutherford was able to experimentally determine that the atom consisted of a heavy nucleus surrounded by light electrons. Some years later Bohr modified the existing atomic model and introduced the idea of quantum states. The neutron was finally discovered in 1932 by Chadwick.

Today one of the most interesting areas within nuclear physics is the de-

[1]The electron was discovered by J. J. Thomson in 1887 and the proton by K. W. Wien the following year

termination of the limits of nuclear stability, such as the upper limit of the nuclear chart, i.e the heaviest nucleus that can be produced. The motivation for the experiment presented in this thesis is to provide necessary impute data for the search of this limit. Theoretical predictions of the location of the stability limit are based on data such as these presented in this thesis.

The atom is as of today consisting of a nucleus of Z protons and N neutrons surrounded by a cloud of electrons placed in orbitals with specific energies. An element with the chemical symbol X is identified by its composition of nucleons and can be noted as:

$$^{A}_{Z}X_{N}$$

where A is the total number of Z+N nucleons in the nucleus. For instance, lead having chemical symbol Pb and proton number 82 will in the case of the nucleus with neutron number 126 have the full notation $^{208}_{82}\mathrm{Pb}_{126}$, often written only as ^{208}Pb.

All known nuclei are placed in a diagram called the *nuclear chart*, an example of which is given in Figure 1.1. The chart is made in a coordinate system with proton number along the y-axis and neutron numbers along the x-axis. Nuclei with same Z but different neutron numbers, thus being placed horizontally with respect to each other, are called *isotopes*. *Isotones* on the other hand, are located in vertical lines as they have the same neutron number but a varying amount of protons. Nuclei with the same mass number A are named *isobars* and can be found lying on a line perpendicular to the diagonal of the nuclear chart. The nuclear chart often provides general information about the nucleus, such as neutron, proton and mass number, life-times, decay modes and the dominating transition for unstable nuclei and abundance for stable nuclei. In the chart presented in Figure 1.1, the stable nuclei are indicated by black squares in the center of the diagonal landscape. The colors in this chart indicate the half-life of the nuclei, from the black defined as stable ($>10^{15}$s) through blue (10^{10} s -10^{2} s), green (10^{1} s -10^{-2} s) and yellow (10^{-3} s -10^{-5} s) to peach (10^{-6} s -10^{-7} s) and pink colored boxed representing nuclei with half lives of order of 10^{-15} seconds and shorter. Approximately 2800 nuclei are known, and of these about 340 are found in nature. Of these, 258 nuclei are indisputably stable while the rest has been observed to undergo decay.

Lifetimes and decay modes are dependent on the structure of the nucleus.

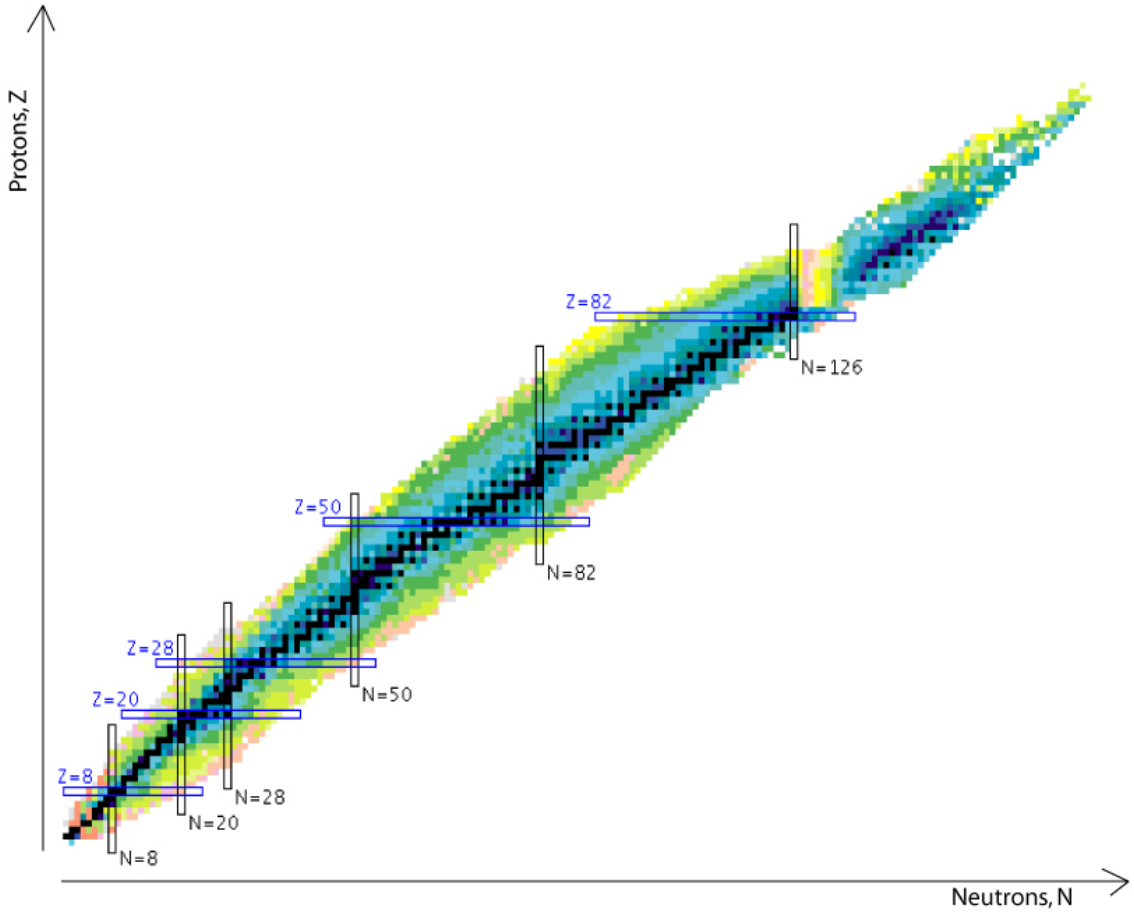

Figure 1.1: The nuclear chart [1].

In nuclear physics, one searches for information on the different nuclei with the ultimate goal of obtaining a better understanding of the inner workings of the nucleus. For instance, nuclear decay is connected to the binding energy of the nucleons. By studying the atomic masses of the nuclei a pronounced structure is seen. The binding energy of the nuclei of proton/neutron numbers 2, 8, 20, 28, 50 and 82 and also 126 for neutrons is increased compared to average numbers. These numbers are called ”magic numbers” and are marked in Figure 1.1. The magic numbers mentioned here are the spherical magic numbers. In addition to these, magic numbers also exist for deformed nuclei. With deformation, the levels of the nuclei shift, possibly resulting in large energy gaps between levels at certain deformations, thus resulting in areas of higher stability. The stability of both spherical and deformed nuclei depends on the magnitude of the shell gaps for both species of nucleons. The most stable nuclei are the ones with doubly magic numbers. When a nucleus is defined as having higher or lower stability, this refers to the half-life for unstable nuclei. With increased stability of a nucleus the half-life is also increased.

One of the least known and most interesting areas within nuclear experimental physics, is that of spectroscopy of nuclei approaching the limit of stability, like that of high mass and charge. Theoretical models are in general able to predict and reproduce experimental results for well known nuclei around the stability line. As one approaches a higher mass region, the discrepancy between theoretical predictions and experimental results increases. The theoretical challenges when it comes to the calculations of heavy elements, are mainly related to the strong Coulomb field, the large mass and large density of states. Figure 1.2 shows the experimentally determined proton levels of ^{249}Bk and the predictions made by different theoretical models. The number marked in boxes indicate the proton number for larger shell gaps. As seen in Figure 1.2 such a large shell gap is found for Z=100. This gap is reproduced by the simple Wood-Saxon model, but when using the more sophisticated models, like self-consistent mean field theories with effective interactions such as SLy, D1S and NL1, the deviations from the true levels are substantial and the prediction of shell gaps are off.

The spacing between the energy levels in the nucleus affects the stability. For magically numbered nuclei, the outermost shell is filled and the spacing to the next shell is large. The last spherical doubly magic nucleus identified is ^{208}Pb. Beyond this nucleus, the stability of the nuclei decrease

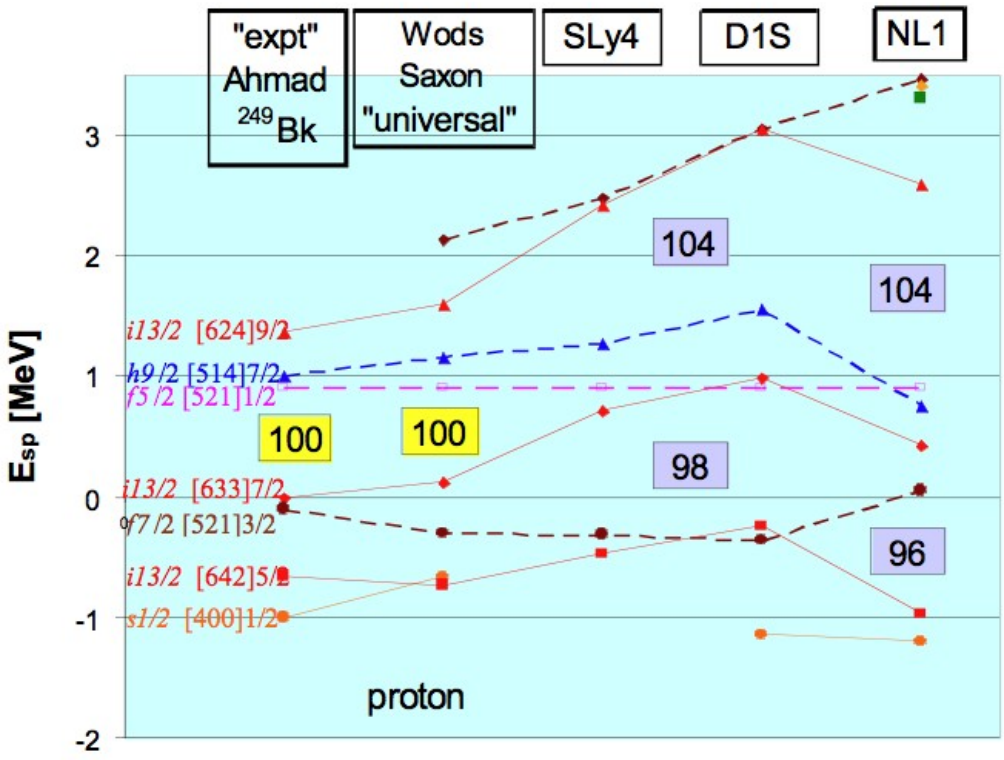

Figure 1.2: Different theoretical predictions of large shell gaps for proton number around 100 [2].

until the transfermium[2] region, an area where deformed magic nuclei are located. The existence of the next spherical doubly magic nucleus is controversial and the nucleon composition predictions varies from theory to theory. Different calculations predict different numbers, among them are Z = 114, 120 or 126 for protons and N = 172 or 184 for neutrons. The area around this possible next spherical doubly magic number is generally named *the island of stability*.

The increasing difficulty of theory to give a satisfactory reproduction of the data, and the divergence in the predictions are, to a certain degree, caused by the lack of experimental data existing for the mass region in question. Spectroscopy of heavy and super heavy elements (SHEs) is problematic due to, among other things, the difficulty of producing the nuclei.

Due to the lack of, or very little data generally available in the mass region, it is essential to confirm previous data as well as get new to test and constrain theories. In this thesis, the α decay of $^{253}_{102}\mathrm{No}_{151}$ is studied to verify previous low- statistic results and determine a previously indirectly seen transition. The motivation for the study of the given isotope in the mass region of interest is as follows: ^{253}No has the advantage of being produced with a relatively high cross section and has a lifetime suitable for decay spectroscopy. It is an odd nucleus with an unpaired neutron and the level scheme of odd isotones of lower mass are relatively well known. In odd nuclei, the levels at low excitation energy are in general caused by the excitation of the valence nucleon, and one can study the systematics of how the levels shift when protons are added. The nucleus was produced in complete-fusion reactions of a ^{48}Ca beam on a ^{207}Pb target followed by neutron evaporation. The experiment took place at Joint Institute of Nuclear Reactions (JINR) in Dubna, Russia, in the spring of 2009 and was a collaboration between many institutes in France, Slovakia, South Africa, Russia, Bulgaria, Romania and Norway. The same collaboration had studied the Nobelium isotope in a previous experiment [3] but found it worth revisiting as the electronics of the focal plane where such that isomer spectroscopy was not possible. From the previous 2004-2005 run to this run in 2009, many things have been changed in the experimental setup; the electronics, the γ-ray efficiency and the recoil transmission through VASSILISSA. This combined with a longer run time, allowed to collect much more data (nearly a factor of 10 more).

[2]Transfermium referring to the region of higher Z than that of Fermium (Z=100)

In this thesis the fundamental nuclear theory relevant to this work will be introduced and discussed in chapter 2, before moving onto a more detailed description of the experiment and setup used, see chapter 3. The analysis of and results from the research are presented and discussed in chapter 4. Finally, a summary and concluding remarks are given in chapter 5.

Chapter 2

Nuclear structure and decay

A short introduction to the theoretical interpretations of the nucleus will be outlined in addition to a discussion of nuclear decay.

2.1 Theoretical description of the nucleus

The first attempt to describe the nucleus was done by looking at the core as one unit and led to the development of the liquid drop model. This model tries to explain the nucleus by looking at the collective forces of the nucleons, describing the bulk (macroscopic) properties of the nucleus. Other models have later been developed trying to describe the more nuanced effects arising from nucleon-nucleon interactions in the core. The shell model, which treats single particle excitations, is one such model. Though the behavior of single nucleons is essential to the microscopic view that the shell model represents; collective forces, such as rotation and vibration, also have to be taken into consideration.

2.1.1 Macroscopic view

The liquid drop model

The liquid drop model was developed by Hans Bethe [4] and Carl von Weizäcker [5] in the 1930s. In the liquid drop model, the nucleus is treated as an incompressible fluid of protons and neutrons.

An important parameter in the nucleus is the nucleon binding energy. The stability of the nucleus, or lack thereof, can be explained by the nucleon binding energy. In Figure 2.1, the binding energy per nucleon is plotted as

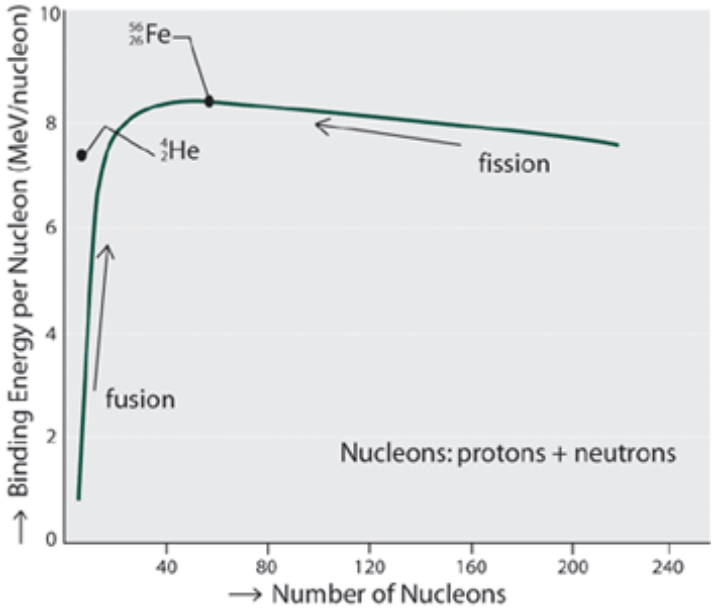

Figure 2.1: The binding energy per nucleon.

a function of nucleon number. As can be seen in this figure, the binding energy per nucleon is increased with increasing mass up to masses smaller than iron (Fe). In this low mass region, the fusion of two light systems releases energy as the binding energy of the final product is greater than the two subsystems. As marked in Figure 2.1, one light nucleus has an uncommonly high nucleon binding energy for the mass region: the $^4_2$He, also known as the α particle. For masses higher than Fe, the binding energy decreases with increasing masses. In this region, fission would be an exothermic[1] reaction as the binding energy of two lighter nuclei may be larger than one heavy nucleus.

In this macroscopic view of the nuclei, the variation in the nucleon binding energy is understood and explained by a few general parameters. An expression for the binding energy used to characterize the variation in nucleonic binding is described by the Bethe-Weizacher formula:

$$B = a_v A - a_s A^{2/3} - a_c Z(Z-1)A^{-1/3} - a_{sym}\frac{(A-2Z)^2}{A} + \delta, \qquad (2.1)$$

where B is the binding energy of the nucleus given in MeV, A is the number of nucleons and Z the number of protons (the charge of the nucleus).

[1]Energy would be released

The $a_{v,s,c,sym}$ are constants adjusted to give the best agreement with experimental results. The force that keeps the nucleus together is the strong force between the nucleons, represented by the first term in the equation, $a_v A$. With increased mass, this volume effect will increase linearly. The nuclear force has a short range and the nucleons will only interact with their closest neighbors and as the nucleon density is roughly constant, each nucleon has approximately the same number of neighbors, thus contributing with about the same amount of binding energy. To this approximation some corrections have to be made to take additional aspects into account. Firstly, in the volume term discussed, a constant contribution from all nucleons is assumed. This is not valid for the surface nucleons, giving rise to a reduction term of $-a_s A^{2/3}$ as the surface area of the nucleus is proportional to $A^{2/3}$. Secondly, in addition to the binding energy, another force is present in the nucleus. The coulomb repulsion between the protons must be taken into consideration. The nucleus is here assumed to be represented by an uniformly charged sphere as each proton repels all others. The reduction in binding energy due to the Coulomb repulsion effect is given by $a_c Z(Z-1)A^{-1/3}$. The two remaining terms in equation (2.1) are not caused by the energy of a charged liquid droplet but nucleon-nucleon interactions. Especially for light nuclei: a symmetric distribution of protons and neutrons will make the nucleus more stable, as can be seen by the placement of stable nuclei in the nuclear chart in Figure 1.1. The term $-a_{sym}\frac{(A-2Z)^2}{A}$ favors nuclei with $Z = A/2$. The importance of the term is reduced for large A as the neutron-proton ratio must be increased to withstand the increasing relative strength of the Coulomb force for heavier nuclei. The last term, δ, accounts for the tendency seen for two nucleons of the same type to couple pairwise to especially stable configurations. When both Z and N are odd, binding energy can be gained by converting one of the odd protons into a neutron or vice versa. By doing this, the converted particle is able to pair with its odd partner. The pairing energy δ is positive for even Z and N, negative for odd Z and N and zero for odd A.

Using the previously discussed expression for the binding energy B, the semiempirical mass formula is obtained:

$$M(Z,A) = Zm(^1H) + Nm_n - B(Z,A)/c^2. \tag{2.2}$$

where $Zm(^1H)$ is the number of protons multiplied with the proton mass, Nm_n is the equivalent for neutrons, $B(Z,A)$ is the binding energy given in equation (2.1) and c is the speed of light in vacuum. Although this expression will not predict any new phenomena in nuclear physics, it is a

first attempt to understand the systematic behavior of a nuclear property, in this case the binding energy.

The liquid drop model and the semiempirical mass formula give a relatively good representation of the more coarse general structural changes of the nucleus as the nucleon number increases. The advantages of the liquid drop model is in its relative simplicity and in giving a general understanding of the macroscopic properties of the nucleus; it is also the only model giving a reasonable description of fission. The weak points of the liquid drop model is that it can only be used to say something about how the general characteristics of nuclei will be influenced by an increase of nucleons. It does not predict the stability of deformed nuclei or 'stable' heavy elements and does not take into account more subtle differences in the structure of the nuclei. A model developed to give a more nuanced view of the nucleus, looking at interactions on a more microscopic level is the shell model.

2.1.2 Microscopic view

The shell model

Using the semiempirical mass formula to calculate the expected binding energy and comparing this to experimentally obtained results, one may present the results as in Figure 2.2. The separation energy increases gradually with N or Z except for a few sharp drops. The drops in separation energy occur at the same particle numbers for both protons and neutrons. The drops occur at Z or N = 2, 8, 20, 28, 50, 82 and N=126. As mentioned in the introduction, these numbers are referred to as 'magic numbers'. A successful nuclear theory must be able to explain this effect.

Atomic theory based on the shell model has provided remarkable clarification of the complicated details of atomic structure. In atomic theory, the properties of atoms are, by part, caused by the number of electrons in the outmost orbital. The filling of atomic orbitals follow the Pauli exclusion principle, which states that two electrons can not have the same quantum numbers. In principle this means that there is a fixed number of electrons that can fit in a given energy state or orbit. Atoms with filled orbitals are less reactive, or more stable, than when this is not the case. To be able to explain nuclear structure, a similar model was developed where one of the basic assumptions was that the protons and neutrons are separatly distributed over certain energy-states subjected to the Pauli exclusion

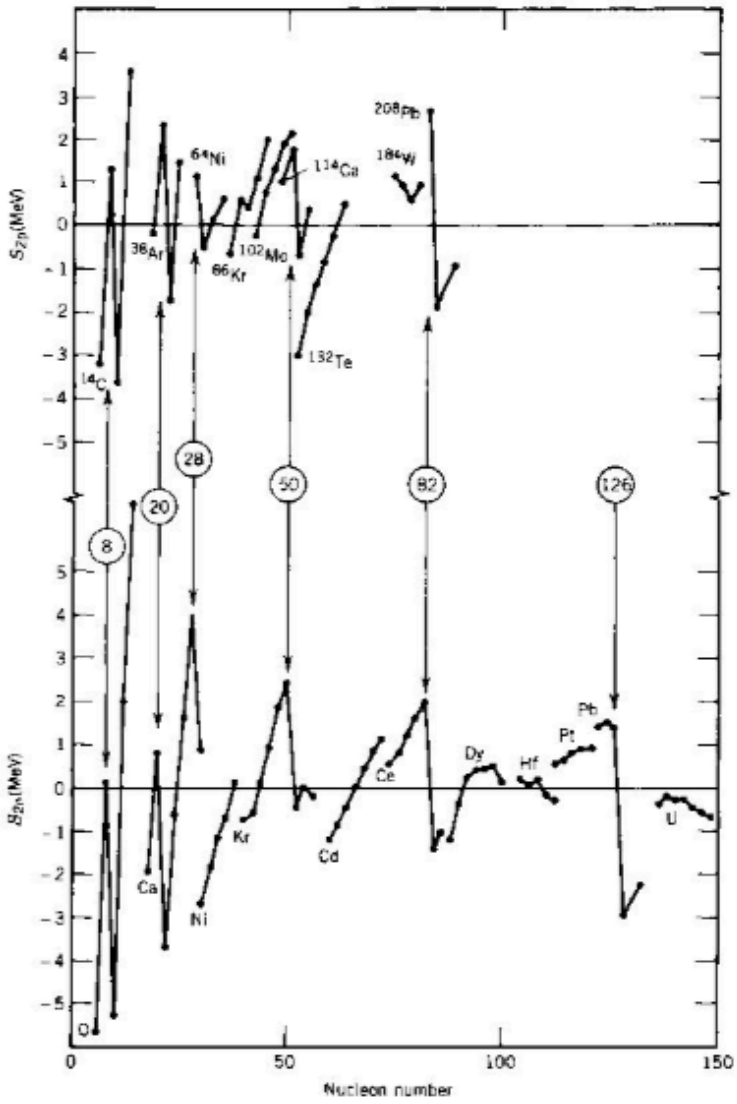

Figure 2.2: The top part of the figure shows the two-proton separation energies with constant neutron number. The bottom part shows the two neutron-separation energy of a sequence of isotopes. The data plotted are differences between predictions of the semi-empirical mass formula and measured values [6].

principle. Like atoms, nuclei may also have excited states and nucleons may be added or removed from the nucleus. In this theory, the sharp discontinuities in the separation energy seen in Figure 2.2 correspond to the filling of major shells.

The fundamental assumption of the shell model is as follows:

> The motion of a single nucleon is governed by a potential caused by all of the other nucleons [6].

With this fundamental assumption, the nucleons can be allowed to occupy the energy levels of a series of sub-shells. To find the energy of the shells a potential must be determined, as can be done by solving the three dimensional Schrödinger equation of an infinite well and the harmonic oscillator. As neither the infinite well nor harmonic oscillator potential are good approximations, an intermediate form of the two potentials, called the wood saxon potential (a mean field potential), shown to the left in Figure 2.3, is used. The large shell gaps, indicated by the circled numbers representing the cumulative number of nucleons in the figure, does not correspond to the 'magic numbers' determined experimentally.

To further develop the theory, again a concept from atomic theory was used: the spin-orbit splitting. Although the origin of nuclear spin-orbit splitting is different from the atomic case [2], there is strong experimental evidence for a nucleon-nucleon spin-orbit force. An inclusion of such a potential was shown in the 1940s, by Mayer, Haxel, Suess and Jensen, to give a proper separation of the sub shells. For this work, Mayer and Jensen were awarded the Noble Price in 1963. The spin-orbit splitting is given by:

$$\kappa < l \cdot s > . \tag{2.3}$$

Here, the $l \cdot s$ factor is the one causing the reordering of the levels. The symbol κ is a strength parameter that in general is set to a constant value. The total angular momentum j is given by $j = l + s$ where s is the spin projection of a single nucleon, which is $\pm \frac{1}{2}$, and l is the angular momentum giving the sub-shell. The degeneracy of each level, i.e. the number of nucleons that can be put in each level, is $2(2j + 1)$.

The shell model can predict structures in the nucleus caused by single nucleons and filling of shells. Single particle exited levels are obtained by the

[2] For atomic electrons, the splitting of spin-orbit is caused by electromagnetic interactions, which is not the case for the nucleus.

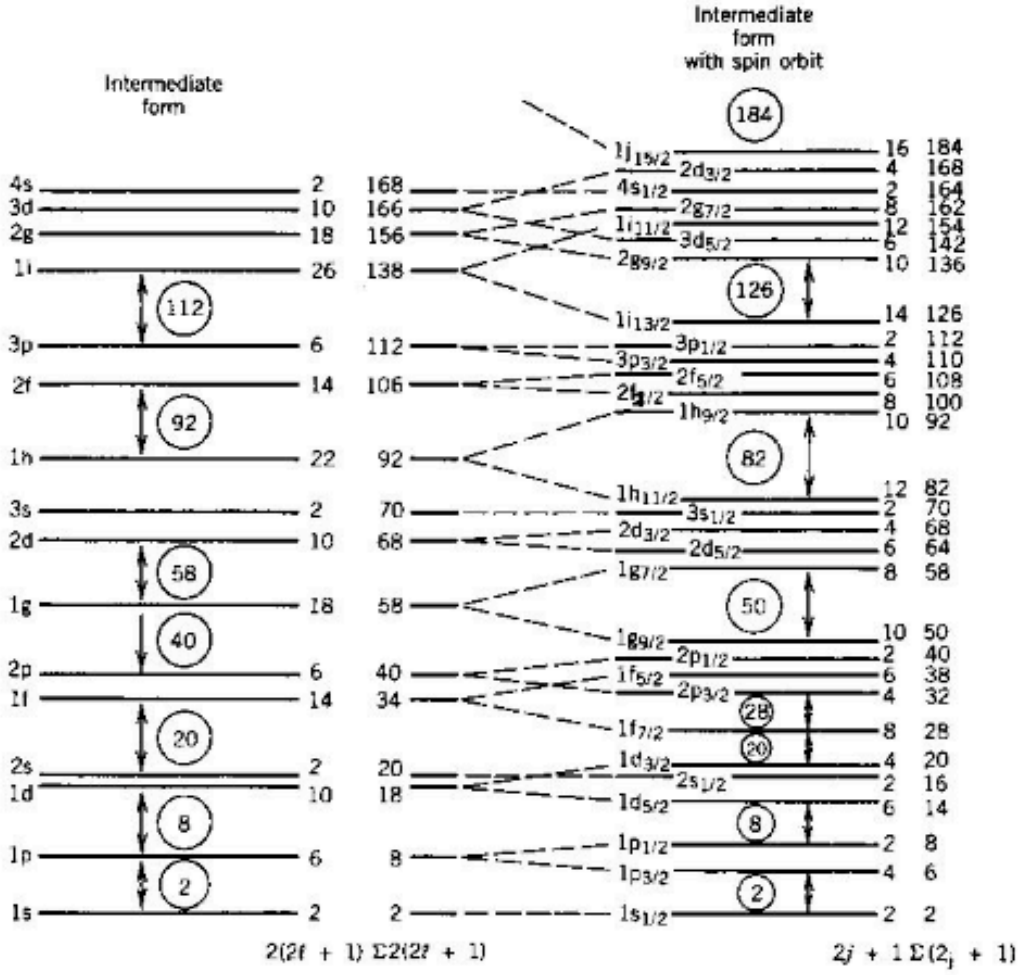

Figure 2.3: Left: Shell structure obtained by using the Woods-Saxon potential. Right: The effect of adding the spin-orbit splitting interaction. The capacity of each level is indicated to its right. Large gaps occur between levels that are associated with closed shells. The circled numbers indicate the total number of nucleons at each shell closure. The shell effect is quite apparent and the magic numbers are reproduced [6].

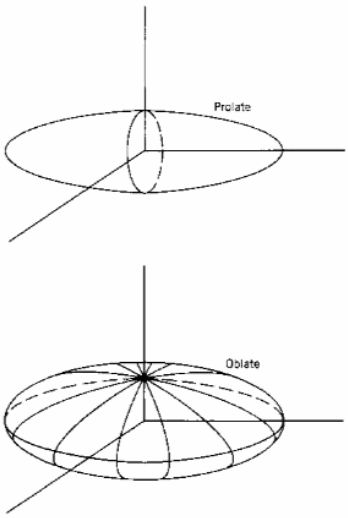

Figure 2.4: Equilibrium shapes of nuclei with permanent deformations. These sketches do not represent snapshots of a moving surface at a particular instant in time but show the static shape of the nucleus [6].

excitation of nucleons up to higher lying orbitals and cause excited band structures in the nucleus. In addition to this, excited states will also be created by collective effects like vibration and rotation of the system as a whole.

Deformation and nuclear rotation

For nuclei with non-spherical equilibrium shapes, also called *deformed nuclei*, rotational motion can be observed. The deformed shape is determined by nucleons in rapid internal motion[3] in the nuclear potential. A measure of the degree of deformation is given by the deformation parameter β

$$\beta = \frac{3}{4}\sqrt{\frac{\pi}{5}}\frac{\Delta R}{R_{av}}, \tag{2.4}$$

where ΔR is the difference of the semi-major and semi-minor axis and for the average radius, R_{av}, it is customary to use $R_{av} = R_0 A^{1/3}$, where $R_0 \approx 1.2$ fm and A is the number of nucleons. Given $\beta > 0$, the nucleus will have a prolate ellipsoid shape as see in the upmost sketch in Figure 2.4. The bottom sketch in the same figure shows an oblate ellipsoid, which

[3]Although the rotation is rapid, it is still sufficiently slow so that the effect on the nucleon orbits is small.

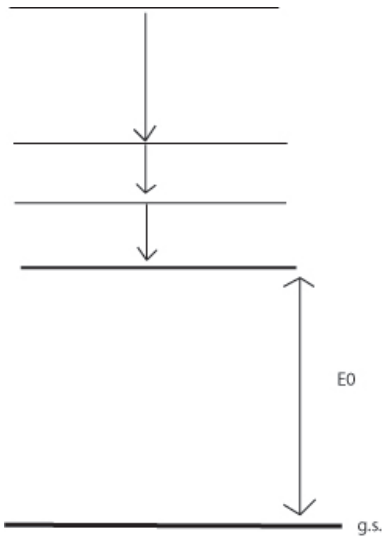

Figure 2.5: Rotational bands built on an excited level of energy E_0.

has deformation parameter $\beta < 0$.

A rotating object has a kinetic energy given by the following equation:

$$A = \frac{1}{2}\mathcal{I}\omega^2, \tag{2.5}$$

where $\mathcal{I}$ is the moment of inertia and ω is the angular velocity. The energy of a rotating object[4] reads:

$$E = \frac{\hbar^2}{2\mathcal{I}}(I(I+1) - K(K+1)) + E_0. \tag{2.6}$$

For an even-even nuclei the K dependance is ignored as K=0. The angular momentum quantum number I corresponds to adding rotational energy to the nucleus and will create excited states known as rotational bands. The rotational bands are built on top of a single particle state with energy E_0, as sketched in Figure 2.5. An estimation of a sequence of states can be found by solving equation (2.6) for different angular momentums.

2.2 Nuclear decay modes

Radioactivity was discovered in 1896 by Henri Becquerel. In the three following years it was noted that the decay rate of pure radioactive sub-

[4] An exception is for the case when K=1/2 where strange things may occur.

stances decreased exponentially. Some years later, it was understood that radioactivity represented changes in the individual atoms and not changes in the sample as a whole. As the decay is statistical in its nature, it is impossible to predict when any given atom will disintegrate. The *disintegration constant*, λ, gives the probability for the decay of an atom per unit time. This probability is constant, and is thus independent of the time passed since the atom was created. The expression for λ is:

$$\lambda = -\frac{(dN/dt)}{N}, \tag{2.7}$$

where N is the number of radioactive nuclei present at the time t and dN is the number of nuclei decaying within a time interval dt. If no new nuclei are introduced into the sample, this ratio will be constant. By integrating equation (2.7) and solving it with respect to the amount of radioactive specimen at the time t, one gets the exponential law of radioactive decay:

$$N(t) = N_0 e^{-\lambda t}, \tag{2.8}$$

where N_0 is the number of nuclei present at time $t = 0$. The half-life $t_{1/2}$ is the time necessary for half of the nuclei to decay. The half-life is given by:

$$t_{1/2} \;=\; \frac{ln(2)}{\lambda}. \tag{2.9}$$

The mean lifetime τ represents the average lifetime of an individual nucleus and is defined as the expectation value of the time needed for an initial population of N_0 radioactive nuclei to decay to $1/e$ of the original number.

$$\frac{N}{N_0} = \frac{1}{e} = e^{-\tau\lambda}, \tag{2.10}$$

$$ln(e^{-1}) = -1 = -\tau\lambda, \tag{2.11}$$

$$\lambda = \frac{1}{\tau}. \tag{2.12}$$

Experimentally, it is the mean lifetime of the nucleus that is measured, as is discussed in Appendix A. By combining the equations (2.9) and (2.12) one gets the following relationship between the mean lifetime (τ) and the half-life ($t_{1/2}$):

$$t_{1/2} = ln(2)\tau \tag{2.13}$$

Several types of decay modes may be in competition for one nucleus. Though the decay probability depends on several nuclear properties, one

term is energy dependent. The decay probability is higher the more energy that is released in the decay. With increased decay energy, there will be more ways for the decay products to share energy and a larger number of final states to decay to. The decay where the most energy is released is in fission. Although fission is energetically possible for relatively light nuclei, this decay channel will not be probable for nuclei lighter than A $\sim$ 250. In fission and α decay the α-particle or the fission product has to surmount or tunnel through a barrier caused by centrifugal force dependent on the angular momentum of the α-particle or fission product in addition to a potential well, called the Coulomb barrier, restricting these types of decay modes.

2.2.1 Alpha decay

Alpha decay is a process where an α particle ($^4_2\mathrm{He}_2$) is emitted from the nucleus. The decay process is:

$$ {}^{A}_{Z}X_N \rightarrow {}^{A-4}_{Z-2}X^{\bullet}_{N-2} + {}^{4}_{2}\mathrm{He}_2, \tag{2.14} $$

where X decays into a daughter nucleus $X^{\bullet}$. The α-decay mode becomes increasingly important for heavier nuclei. With increasing mass of the nuclei, the Coulomb force will become more dominant as this force increases with Z^2, while the nuclear binding force will increase linearly. The α particle has a tightly bound structure and thus a low mass compared to the mass of its separate constituents. The energy released in the α decay comes from the decrease in the mass of the system.

In the decay process there must be a conservation of energy:

$$ m_X c^2 = m_{X^{\bullet}} c^2 + T_{X^{\bullet}} + m_\alpha c^2 + T_\alpha \tag{2.15} $$

The left side of the equation is the mass energy of the nucleus before it α-decays. This energy must be equal to the energy of the total system after the decay, including the kinetic energy $T_{X^{\bullet}}$ and T_α of the daughter nucleus and α particle and the mass energy of the products $\mathrm{X}^{\bullet}$ and α. The net energy released in the decay process is called the Q-value.

$$ Q = (m_X - m_{X^{\bullet}} - m_\alpha)c^2 \tag{2.16} $$

This value is also equal to the total kinetic energy given to the decay fragments, and is expressed as:

$$ Q = T_{X^{\bullet}} + T_\alpha + E^*_{X^{\bullet}} \tag{2.17} $$

where $E^*_{X\bullet}$ is the excitation energy of the daughter in the case where it is left in an excited state. The kinetic energy of the daughter, $T_{X\bullet}$, represents the recoil of the nucleus as the α is emitted. The equation can be approximated [5] as:

$$Q = \frac{M_{mother}}{M_{daughter}} T_\alpha + E^*_{X\bullet} \tag{2.18}$$

M_{mother} and $M_{daughter}$ being the mass (number of nucleons A) of the mother and daughter.

2.2.2 Fission

The fission of a nucleus is primarily a result of the increasing Coulomb-binding energy ratio for heavy nuclei. In fission, a heavy nucleus splits into two smaller nuclei. The fission products are not uniquely determined but have a mass distribution around about $A \approx 95$ and $A \approx 140$ for the two fragments. Fission occur when the Coulomb barrier is not able to hold the nucleus together. At high energies, this barrier is thinner and relatively easy to penetrate. The height of the Coulomb barrier is about 220 MeV, which is roughly equal to the energy released in fission decay. For spontaneously fissioning nuclei, the energy released in the decay is somewhat lower than the height of the barrier, making the existence of the original nucleus possible. The barrier is here thin enough to be penetrated. Fission may also occur in to the production of excited states or compound-nuclear states. In such intermediate forms, induced fission may compete successfully with other decay modes if the energy is close to the top of the barrier.

2.2.3 Beta decay

A nucleus with an excess of either protons or neutrons can correct the inequality of nucleon type by converting the excess nucleon type to the other. For example, a proton can be converted to a neutron in a proton-rich nucleus or vise versa if the nucleus is neutron rich. This process may occur in three possible ways. Each process involves another charged particle to

[5] The approximation is due to neglecting the binding energy of the daughter and the α particle to equate $\frac{M_\alpha}{M_{daughter}}$ to $4/A$

conserve electric charge.

$$n \rightarrow p + e^- \quad (\beta^- decay) \tag{2.19}$$
$$p \rightarrow n + e^+ \quad (\beta^+ decay) \tag{2.20}$$
$$p + e^- \rightarrow n \quad (electroncapture, EC) \tag{2.21}$$

In all three processes a neutrino is also emitted. The neutrino is necessary to conserve lepton number and energy but does not have an electric charge and its inclusion in the decay process does not effect the identity of the other final particles.

2.2.4 Gamma decay

After β or α decay, the nucleus is sometimes left in an excited state. Whether this is the case depends on the overlap of the wave function between the ground states of the mother and daughter nuclei. In an even-even nucleus (no unpaired nucleon), decay directly to the daughters ground state is probable (0^+ to 0^+). However, if the ground states are not compatible, the de-excitation may go through several excited states. An excited state may decay by the emission of γ radiation. A γ ray is a photon of electromagnetic radiation originating in the nucleus.

The transitions between the states are characterized by the energy E_γ, the photon angular momentum, the order of polarity L and the change of parity $\Delta\pi$. The energy of the emitted γ-ray is given by the difference of energy in the initial and final energy level,

$$E_\gamma = E_i - E_f. \tag{2.22}$$

The possible orders of multipolarity for the transition is related to the change in angular momentum by

$$\mid I_i - I_f \mid \leq L \leq I_i + I_f \tag{2.23}$$

The multipolarity of a transition is determined by L and $\Delta\pi$. For an electric multipole (EL) transition the following selection rule applies:

$$\Delta\pi(EL) = (-1)^L \tag{2.24}$$

while for the magnetic multipole transition, we have

$$\Delta\pi(ML) = (-1)^{L+1} \tag{2.25}$$

For example, if I_i=$\frac{3}{2}$ and I_f=$\frac{5}{2}$, then the possible orders of multipolarities are:

$$\begin{aligned} |\,\frac{3}{2}-\frac{5}{2}\,| \;&\leq L \leq\; \frac{3}{2}+\frac{5}{2} \\ 1 \;&\leq L \leq\; 4 \end{aligned}$$

The radiation field would in this case consist of a dipole ($L = 1$), a quadrupole ($L = 2$), an octupole ($L = 3$), a hexadecapole ($L = 4$) or a mixture of these. Whether the type of radiation emitted is electric or magnetic is determined by the relative parity of the final levels. If there is no change in parity, then $\Delta\pi$ = no and the radiation field must have even parity. If there is a change in parity between the initial and final state, then the radiation field has odd parity. The electric and magnetic multipoles differ in their parities. Electric transitions have even parities if L = even while magnetic transitions have even parities if L = odd. A $\Delta\pi$ = no transition will consist of even electric multipoles and odd magnetic multipoles. The reverse is the case if $\Delta\pi$ = yes. Given no change in parity in the example given, the possible multipole transitions would be $M1$, $E2$, $M3$ and $E4$. In the case where either the initial or final state has angular momentum 0 then only one pure multipole transition is emitted. If both are 0 then radiative transitions are not permitted. The state may decay with internal conversion (see next section).

The Weisskopf estimates provide a reasonable relative estimation for comparison of the transition rates. The formulae to calculate probabilities of EL and ML transitions, $\lambda(EL)$ and $\lambda(ML)$, can be found in [6]. The Weisskopf estimates for the lower order multipoles are as follows:

$$\begin{gathered} \lambda(E1) = 1.0 \text{ x } 10^{14} A^{2/3} E^3 \\ \lambda(E2) = 7.3 \text{ x } 10^{7} A^{4/3} E^5 \\ \lambda(E3) = 34 A^2 E^7 \end{gathered}$$

$$\begin{gathered} \lambda(M1) = 5.6 \text{ x } 10^{13} \mathrm{E}^3 \\ \lambda(M2) = 3.5 \text{ x } 10^{7} A^{2/3} E^5 \\ \lambda(M3) = 16 A^2 E^7 \end{gathered}$$

Here, A is the number of nucleons. The energy of the γ emitted is E, and is given in MeV. The transition rate λ is given in s^{-1}. These estimates for transition probabilities are not to be taken as true theoretical calculations

to be compared to measured values, but can be used to draw general conclusions about transition probabilities. Firstly, the lower multipolarities are dominant. By increasing the order of polarity by one, the probability of transition will decrease with an order of 10^5. The second conclusion that can be drawn from the Weisskopf estimates is that for a given order, the electric radiation is more likely than the magnetic radiation by a factor of two in medium and heavy nuclei.

The Weisskoph unit, w.u, is the difference between the measured transition rate and the theoretical Weisskoph estimate:

$$w.u = \frac{measured}{weisskopf}. \tag{2.26}$$

If the w.u is large, the state is likely to be a collective state.

2.2.5 Conversion electrons

Internal conversion is an electromagnetic process that competes with γ-ray emission. The electromagnetic multipole fields in the nucleus interact with atomic electrons and cause one of the atomic electrons to be emitted. The transition energy, ΔE, is in this case the kinetic energy T_e of the electron plus the binding energy, B_e. The binding energy is the energy required to knock the electron loose from its shell. The transition energy is thus as follows:

$$T_e = \Delta E - B_e. \tag{2.27}$$

The energy of the emitted electron will vary with the atomic orbital it was originally situated in due to differences in binding energy for the different orbitals. After the emission of a conversion electron the nucleus is left with a vacancy in one of the electronic shells. This vacancy will be filled by an electron from a higher lying orbital, creating a new vacancy that again has to be filled. In this process characteristic X-rays may be emitted. For this reason, in the γ spectrum of a nucleus that can decay by conversion electrons, X-rays are usually present at the low-energy end of the spectrum. A competing channel to the emission of X-rays is the emission of Auger electrons. In this process, the excess energy is absorbed by an electron, which will then escape the nucleus. The atomic Auger-decay can occur in any stage of de-excitation of the atom.

In some cases, internal conversion will be highly favored over γ decay while in other cases γ decay is by far the dominating decay mode. The

likelihood of electron emission relative to γ emission is defined by the *internal conversion coefficient* α:

$$\alpha = \frac{\lambda_e}{\lambda_\gamma}, \tag{2.28}$$

where λ_e is the decay probability for internal conversion and λ_γ is the probability of decay by γ-ray emission. Experimentally, the conversion coefficients are found by :

$$\alpha_{trans} = \frac{I_e \cdot \epsilon_\gamma}{I_\gamma \cdot \epsilon_e}, \tag{2.29}$$

Here, I_e and I_γ are the number of electrons and γ rays detected for the given transition while ϵ_γ and ϵ_e are the efficiency of the detectors at the given energy. The internal conversion coefficient is independent of the details of the nuclear structure[6] but will depend on the atomic number of the atom, the energy of the transition and its multipolarity. Non-relativistic calculations of internal conversion coefficients for electric and magnetic mulitpoles give the following equations:

$$\alpha(EL) \cong \frac{Z^3}{n^3}\left(\frac{L}{L+1}\right)\left(\frac{e^2}{4\pi\epsilon_0\hbar c}\right)^4\left(\frac{2m_e c^2}{E}\right)^{L+5/2}, \tag{2.30}$$

$$\alpha(ML) \cong \frac{Z^3}{n^3}\left(\frac{e^2}{4\pi\epsilon_0\hbar c}\right)^4\left(\frac{2m_e c^2}{E}\right)^{L+3/2}, \tag{2.31}$$

where Z is the atomic number of the atom where the conversion takes place, n is the principal quantum number of the bound electron wave function, L is the multipole order and E is the transition energy. The terms $\frac{e^2}{4\pi\epsilon_0}$ and $\hbar c$ are fine structure constants where e is the electron charge, c the speed of light, $\hbar$ is Planck's constant divided by 2π and ϵ_0 is the vacuum permittivity. These approximations given in equations (2.30) and (2.31) reveal a number of features of the probability of internal conversion versus that of γ-ray emission. First of all, the conversion coefficient has a strong Z-dependence. Due to the proportionality of Z^3, the conversion process is more important for heavy nuclei than for light nuclei. The $1/E$ dependence implies a rapid decrease in probability for conversion electrons with higher transition energies. An increase in multipole order will lead to a rapid increase of the conversion probability due to the part powered by L. For transitions of high polarity, internal conversion may be far more

[6]Though this is normally the case and the basis for theoretical calculations, anomalous conversion coefficients may occur due to nuclear structure effects like retardation, see Appendix B.

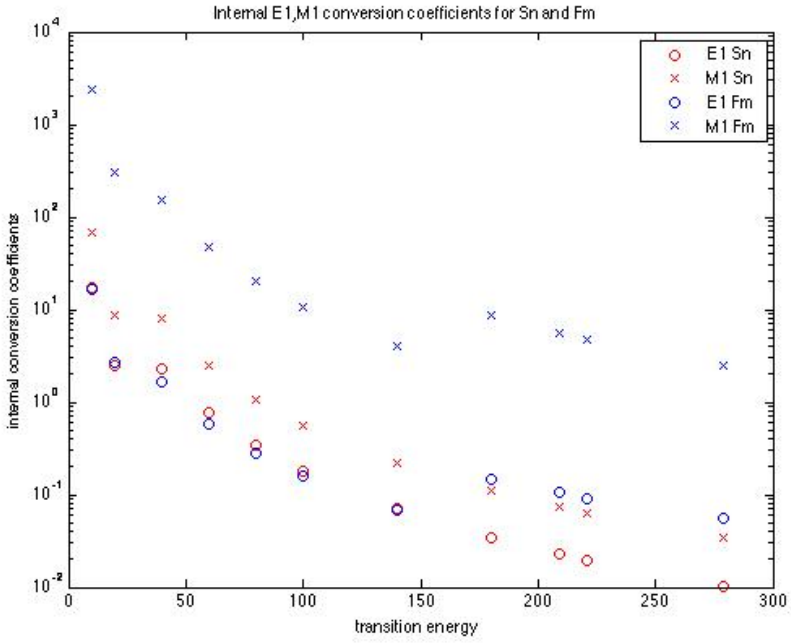

Figure 2.6: Total conversion coefficients for $E1$, $\circ$, and $M1$, x, transitions for Z=50 (red) and Z=100 (blue) nuclei.

probable than γ emission. A fourth variable that will effect the coefficient, is the number of the atomic shell from which the electron is knocked out since the coefficient decrease with $1/n^3$. Given these dependencies one can expect a relatively high K-shell conversion coefficient for low-energy, high multipolarity transitions in heavy nuclei.

Figure 2.6 shows the relationship between the conversion coefficient with respect to energy for $M1$ and $E1$ transitions for Sn (Z=50) and Fm (Z=100). The data are taken from the Bricc database [7]. As can be seen in the figure, the conversion coefficient increases with Z and is reduced as the energy increases. Further, it can be seen that the coefficient is higher for $M1$ transition than $E1$ transition. Also, the probability for internal conversion is higher for K-shell electrons and will be reduced for orbits farther away from the core. The increase in conversion coefficients in Fm between transition energies 140 keV and 180 keV is due to the transition energy surpassing the binding energy of the K-shell electron ($E_{binding(Fm)}(K) \sim 142$ keV).

Since the conversion coefficients strongly depend on the character of the

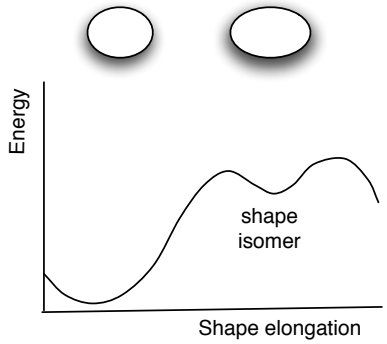

Figure 2.7: Isomeric state caused by shape elongation.

transition, the multipolarity and electric or magnetic character can be determined by measuring the ratio of electron to γ-ray intensities. This information is then used to establish or constrain the spin and parity of nuclear states.

2.2.6 Isomeric decay

Although excited states in the nucleus generally decay almost instantaneously, there are some sates with relatively long (measurable) lifetimes. If the half-life of γ emission for a specific state is significantly longer than normal ($\sim 10^{-9}$ s), the state is called an isomeric state and the transition is known as an isomeric transition. Isomeric states occur when a state is ill matched with possible states it may decay too. A nucleus being in an isomeric state will be trapped in a secondary energy minimum that may occur for certain values of shape elongations, spin or the spin projection onto the symmetry axis. Figure 2.7 shows a sketch for such a minimum for an elongated nucleus. When located in such energy pockets, the change of spin, shape or orientation will be difficult, resulting in a state that will survive for a long time before decaying.

In experimental nuclear physics, the identification of isomeric states are essential. Overlooking such a state can lead to errors in the interpretation of the quantum structure of the nuclei and also influence the structural interpretation of daughter nuclei. Ordering of single-particle states, deformations and collective correlations are among the underlying structures that isomeric states may reveal.

Chapter 3

Experimental techniques

3.1 Nuclear Spectroscopy

Spectroscopy can be divided into 2 parts, prompt and decay spectroscopy. In prompt spectroscopy, radiation is detected at the target position, while in decay spectroscopy the phenomenon of interest is the delayed decay of the produced nucleus. A schematic setup for the different spectroscopy types is sketched in Figure 3.1. The difference between the two types of spectroscopy stems from where the detector arrays are set up. In prompt spectroscopy, the immediate decay after the production of a nucleus is detected, giving information of the energy levels in the produced compound nucleus. Decay spectroscopy looks at the isomeric states of the nucleus and levels in the daughters. The nuclei produced at the target position are filtered in a separator to reduce the amount of undesired reaction products and select the products of interest. Spectroscopy is only possible if the lifetime of the nucleus (or isomeric state) is longer than the time it takes to go through a separator and be implanted into a detector. The particle beam intensity used for the different spectroscopy types differ. In prompt spectroscopy the beam intensity must be low for the detectors to be able to handle the event rate[1]. In decay spectroscopy, the wanted products are selected in a separator and radiation hitting the detector system where the recoil is implanted is not that intense. In this type of spectroscopy high beam intensity is preferable.

The experiment analyzed in this thesis was obtained by using decay spectroscopy. Figure 3.2 shows part of the detector setup used. As nuclei are produced and separated, they will end up being implanted into a seg-

[1]The reaction rate - and hence radiation level - at the target is very high.

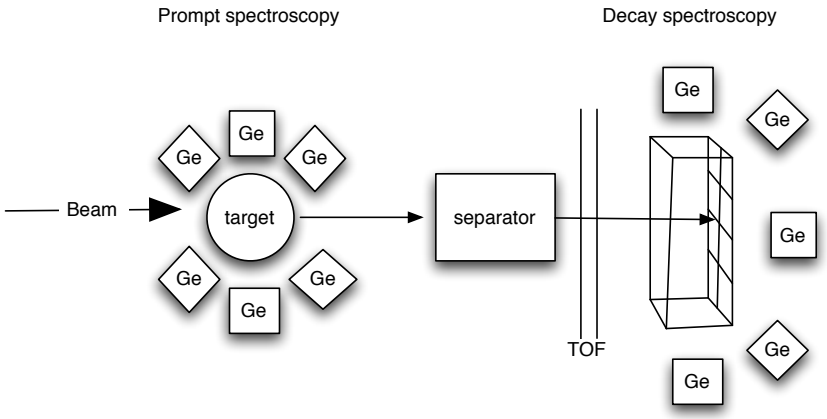

Figure 3.1: Sketch of the detector setups for prompt and decay spectroscopy. Prompt spectroscopy detects γ-rays at the target position where the nuclei of interest are produced. Decay spectroscopy detects all types of radiation associated with the decay of the nuclei and are placed after a separator, thus further away from the target station.

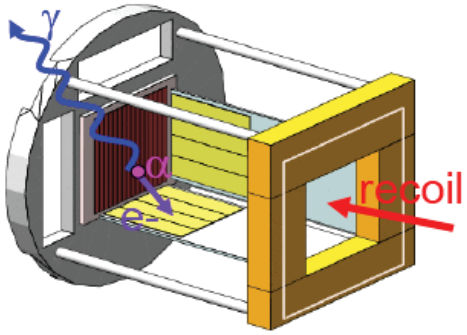

Figure 3.2: Sketch of the particle detection system. The nuclei produced (recoils) are implanted into a segmented detector placed at the focal plane of the separator (brown). The implanted nuclei may decay by fission or by emission of α, β, γ or conversion electrons. Electrons and α particles escaping the focal plane detector will be detected in the tunnel detector (yellow)

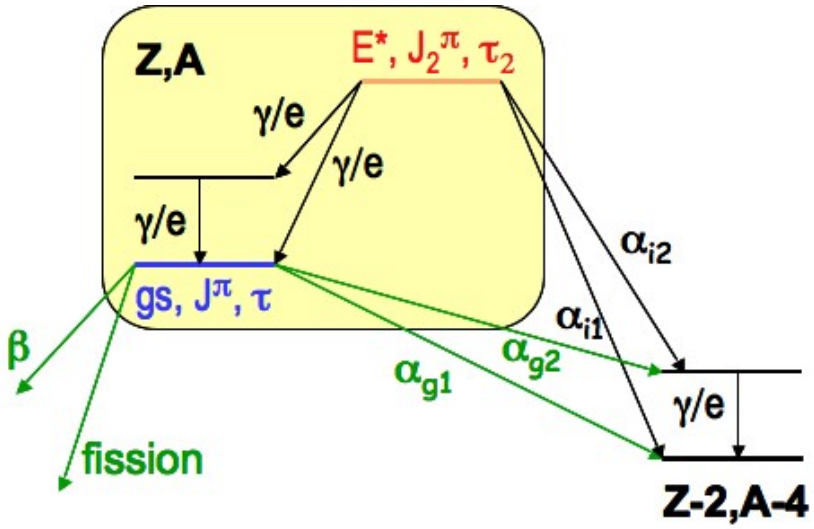

Figure 3.3: Sketch showing the different types of decay a nucleus may undergo

mented detector placed at the focal plane of the separator. In this detector the kinetic energy of the nuclei are registered as well as the α energy of later decay. As the nucleus decays, γ-rays and conversion electrons may be emitted. The γ-rays are detected in the Ge detectors surrounding the focal plane detector. The conversion electrons are registered in a tunnel detector, sketched in Figure 3.1, and more detailed in Figure 3.2. In the latter figure, the tunnel is represented by two of four yellow walls, each segmented into four strips.

Decay spectroscopy is further divided into two parts, depending on whether the state is isomeric or not. The following section gives a quick overview of these two types of decay.

3.1.1 Decay spectroscopy

Figure 3.3 shows the decay of the unstable nucleus, Z, A. The red line marks an isomeric state, with excitation energy E^*, spin and parity J_2^π and a mean life time τ_2. This state may decay to the ground state, gs, either via an excited state or directly by the emission of γ or conversion electron. Another possibility for the decay of the isomeric state is by α decay to the ground state or an excited state in the daughter, Z-2, A-4. The ground state in the mother, Z, A, can undergo β, α decay or fission. The α decay may be

directly to the ground state of the daughter or can feed an excited level. Experimentally, these decay types are studied by looking at α-γ coincidences in the case of prompt α decay and delayed γ-ray emission following the recoil implantation in the case of the decay of isomeric states.

3.2 Production of heavy elements

3.2.1 General characteristics

After the discovery of radioactivity and up to around 1940, heavy elements where discovered and studied through radioactivity of uranium, U, and thorium, Th, that are found in nature. The creation of heavier elements was done between 1940-1952 by using neutron beams. Capture reactions on U targets and subsequently β decay produced elements up to Z=100. When this method was reaching its limit for production of heavier elements, light ion beams were tried. Hot fusion reactions where used to create element with Z=101-106 before cold fusion became popular. The elements Z=107-112 were created by cold fusion reactions before the return of hot fusion for the production of elements Z=114, Z=116-118.

Over the last 40 years, complete-fusion reaction has been the most promising method for creating super heavy elements (SHE). In this type of reaction, where compound nucleus evaporation products are created, a particle beam is accelerated up to a given energy before hitting a target. The beam particles and target particles fuse into an excited compound nucleus (CN) which will subsequently emit one or several light particles like neutrons, protons and α particles before decaying by the emission of γ-rays. This evaporation-residue (ER) is the desired channel, but is not the only possible nor the dominating one. As the beam particles impinge on the target, they will in most cases pass through without interacting or scatter due to Coulomb interactions with the target particles. Transfer reactions, where some nucleons are transferred, have higher probability when actual impact occurs than the fusion of the particles. In the cases where fusion occur and a CN is created, the highly excited compound nucleus will de-excite by emission of particles, as described for the ER channel, or it may fission. In every step of the de-excitation by nucleon emission, fission will be a competing channel and in general the dominating one. The probability for fission increases with beam energy as the excitation energy of the nucleus is increased making the nucleus less stable.

In the fusion of target and beam, all the mass of the bombarding particle is transferred to the target nucleus creating a CN. The excitation energy of the compound nucleus, E^*_{CN} is determined by:

$$E^*_{CN} = \Delta E_{kin} + Q_{fusion} \tag{3.1}$$

$$\tag{3.2}$$

where ΔE_{kin} is the change in total kinetic energy in the reaction and Q_{fusion} is the Q-value of the reaction.

$$Q_{fus} = (m_{projectile} + m_{target} - m_{cn}) \cdot c^2 \tag{3.3}$$

where $m_{projectile}$, m_{target} and m_{cn} are respectively the mass of the projectile, target and compound nucleus.

Conservation of momentum gives:

$$m_{cn} \cdot v_{cn} = m_{projectile} \cdot v_{projectile} + m_{target} \cdot v_{target} \tag{3.4}$$

$$\Rightarrow v_{cn} = v_{projectile} \frac{m_{projectile}}{m_{cn}}, \tag{3.5}$$

where m_{cn} and v_{cn} is the mass and velocity of the compound nucleus, $m_{projectile}$ and $v_{projectile}$ is the mass and velocity of the beam and m_{target} and v_{target} are the values for the target.

Given conservation of energy, the difference in kinetic energy before and after the fusion of the beam and target can be deduced. The velocity components $v_{projectile}$ and v_{cn} for the beam and recoil respectively, are in the direction of the beam (z-component into the plane, perpendicular to the DSSD), so that

$$\Delta E_{kin} = \frac{1}{2}(m_{projectile} v^2_{projectile} - m_{cn} v^2_{cn}). \tag{3.6}$$

The expressions used are the classical expressions and can be used if the velocities are less than $\sim 10\%$ of the speed of light.

Inserting (3.5) into equation (3.6) one gets the following expression:

$$\Delta E_{kin} = \frac{1}{2}(m_{projectile} v^2_{projectile} - m_{cn}(v_{projectile} \frac{m_{projectile}}{m_{cn}})^2) \tag{3.7}$$

$$= \frac{1}{2} m_{projectile} v^2_{projectile} (1 - \frac{m_{projectile}}{m_{cn}}) \tag{3.8}$$

$$= E_{beam}(1 - \frac{m_{projectile}}{m_{cn}}). \tag{3.9}$$

As mentioned, there are two different types of fusion methods: hot and cold. Combining light ions and radioactive targets gives rise to so-called hot-fusion reactions as the compound nucleus will be left in a highly excited state, $E^*_{hot-fusion} \geq 40$ MeV. In cold fusion reactions magic numbered or highly bound targets such as Pb and Bi are fused with ions heavier than Ar ($Z = 18$). As these targets are tightly bound, a large amount of energy is required to break up the initial bound system and transform it into a less bound system. The excitation energy of cold fusion reaction is typically of the order of $E^*_{cold-fusion} \leq 20$ MeV. For instance, an example of hot fusion is

$$^{22}\text{Ne} + ^{238}\text{U} \rightarrow ^{260}\text{No}^*.$$

With a beam energy of 117 MeV, the kinetic energy, ΔE, of the CN is 107 MeV while the Q_{fusion}-value is -56.3 MeV. The compound nucleus has 50.8 MeV excitation energy.

$$^{28}\text{Ca} + ^{208}\text{Pb} \rightarrow ^{256}\text{No}^*$$

is a cold fusion reaction. Using a beam energy of 213 MeV, the values $\Delta E = 173$ MeV, $Q_{fusion} = -153.8$ MeV and $E^*_{CN} = 19.3$ MeV are obtained. The ERs of interest in these reactions are ^{254}No and ^{255}No. The beam energy in the two methods is different and chosen so that the correct ER will be produced, and is in the cold fusion drastically higher than that used for the hot fusion. Looking at the excited CN produced, the excitation energy is a lot higher for the hot fusion as the change in binding energy is larger for the cold fusion. The production of hot compound nuclei is easier than using the more tightly bound target as is the case for cold fusion, but when a CN is created, due to the low excitation energy, the cold CN is less probable to fission.

3.2.2 Recoil production at Joint Institute of Nuclear Reactions (JINR)

The experiment discussed in this thesis took place at the Joint Institute of Nuclear Reactions (JINR), located in Dubna, Russia. The accelerator at JINR is a U-400 cyclotron that produces pulsed beams. Degrader foils of Aluminium (Al) and titanium (Ti) are used to vary the beam energy and the energy is controlled by measuring the energy of ions scattered at a given angle (30°). The typical energy spread of the beam is $\approx 1\%-1.5\%$.

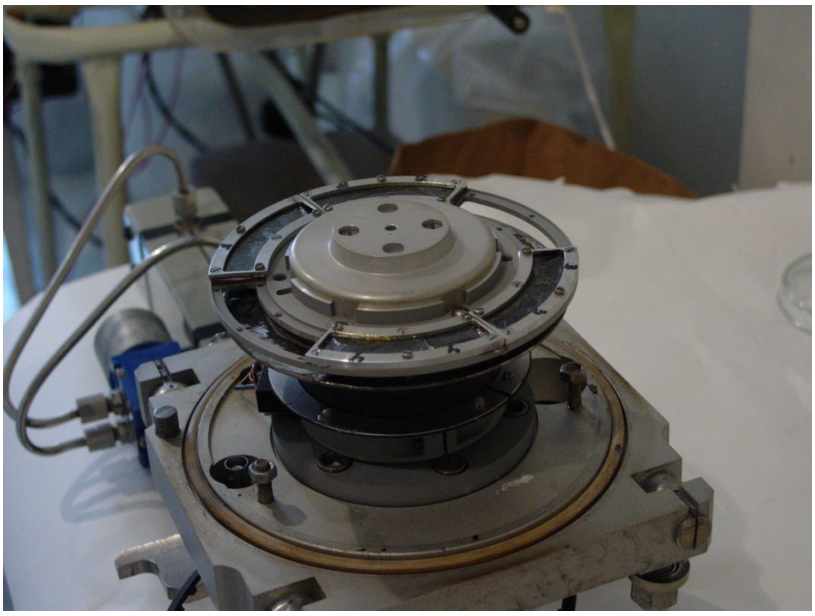

Figure 3.4: Picture of the target wheel

The target is mounted on a rotating wheel, shown in Figure 3.4, to avoid melting of the target due to high beam intensity. A stationary target would not be able to stand the generated heat produced with beam intensities of 10^{12}-10^{13} s^{-1}. The rotation of the wheel is synchronized with the pulsation of the cyclotron beam to ensure that the beam hits the target and not the spokes. Targets with 2 different different thicknesses[2] (350 $\mu g/cm^2$ and 680 $\mu g/cm^2$) where used with a 1.5 μm Ti backing.

Kinematics and cross section

The cross section, σ, is a measure of the probability of the occurrence of a type of reaction. The cross section is measured in barn, b, which equals $10^{-24}cm^2$. Figure 3.5 shows the relationship between the σ for the number of neutrons evaporated, xn, as a function of excitation energy of the compound nucleus, E^*_{CN}, for the ^{48}Ca+^{207}Pb reaction. The CN created is ^{255}No. The B_{Bass} marked in red in the figure is the Bass barrier, which is the minimum beam energy needed to overcome the Coulomb potential barrier between the beam and the target. In a classical system, fusion or transfer reactions would not be possible below this barrier. The optimal

[2]The use of two target thicknesses is not ideal as the thickness will effect the energy spread, but necessary as there where not enough targets of one thickness.

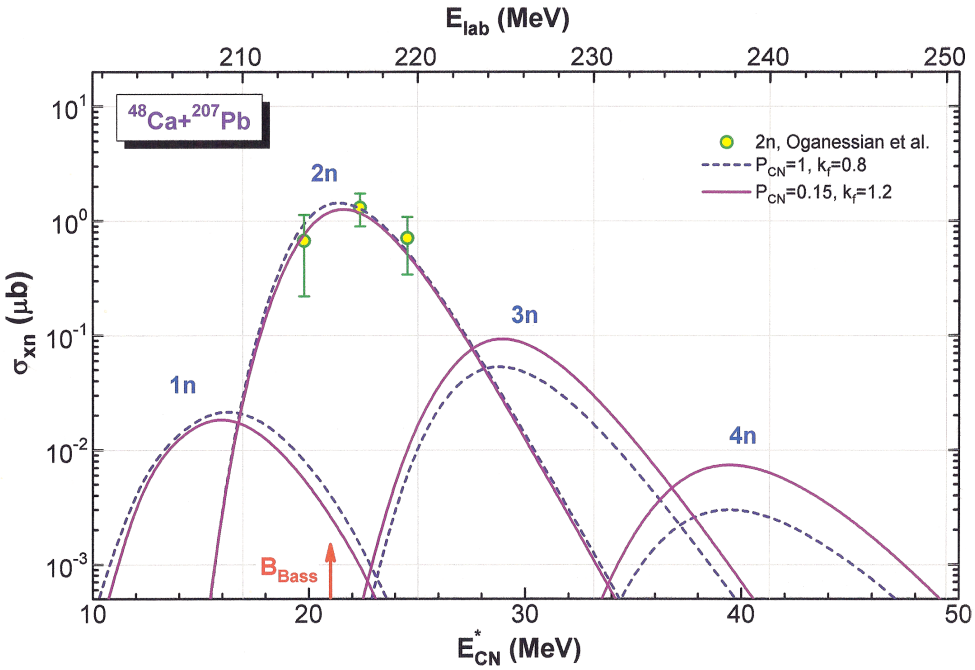

Figure 3.5: Cross sections for different neutron evaporation channels in the fusion reaction ^{48}Ca + ^{207}Pb as a function of excitation energy of the compound nucleus E^*_{CN}. The symbols correspond to experimental data while the lines are results of different calculations. Courtesy of Alexander Yeremin [8, 9].

Nucleus	mass (u)
^{255}No	255.09324
^{207}Pb	206.975872
^{48}Ca	47.952533

Table 3.1: Masses used to determine optimal beam energy for the creation of ^{253}No [1].

beam energy is, as can be seen in the figure, of a slightly higher value than that of this barrier. The cross section of the ER created is highly dependent on the excitation energy of the CN ^{255}No. It should also be noted that for a given excitation energy, different ERs are likely to be produced as the cross section areas overlap. For instance, at an excitation energy of the CN of 30 MeV, the dominant ER would be the result of the 3n-evaporation giving ^{252}No, but the 2n-channel creating ^{253}No would also be present.

The desired nucleus in this work is ^{253}No and from Figure 3.5, one can read off that the highest production cross section is for E^*_{CN} = 21 MeV. Using the equations (3.9) and (3.1) the ideal beam energy can be calculated:

$$E_{beam} = (E^*_{CN} - Q_{fusion})\frac{1}{1 - \frac{m_{^{48}Ca}}{m_{^{255}No}}} \tag{3.10}$$

The mass of the components are given in Table 3.1. Using equation (3.3) to calculate the Q-value of the fusion and the relationship 1u = 931.502 MeV/c^2, the ideal mid-target[3] beam energy of the experiment is found to be $\sim$ 215 MeV (which correspond to E_{Lab} in Figure 3.1). The mid-target beam energy used was slightly higher, approximately 220 MeV, see Figure 3.5

3.3 Experimental details

The reaction used in the experiment was the ^{207}Pb(^{48}Ca,2-3n)$^{252-253}$No reaction, where a ^{207}Pb-target was bombarded by a ^{48}Ca beam creating a ^{255}No compound nucleus that evaporated 2-3 neutrons creating $^{252-253}$No ERs. The run time for the experiment was $\sim$ 19 days. Of the order of 90 000 α particles from $^{253(254)}$No[4] and $\sim$6600 ^{252}No αs were detected in the focal plane detector setup VASSILISSA. At the average mid-target beam energy of $\sim$220 MeV, the average cross section is $\sim$300 nb for ^{253}No and $\sim$20 nb for ^{252}No as can be read of Figure 3.5.

[3]The mid-target energy is the average beam energy in the middle of the target. The original beam energy had a value of $\sim$233 MeV but was reduced by interaction in the Ti backing and in half the thickness of target.

[4]The true number of ^{254}No produced was estimated by subtracting a simulated α spectrum from the experimental one, see Appendix C, and was found to be close to 10000, thus the number of ^{253}No observed was 80000.

3.4 Experimental setup

As previously discussed, the dominant channel in the de-excitation of the ER is fission. The low production rate combined with γ-ray and conversion electron background from the fission fragments lead to a low production rate of the desired ERs. The low ER production rate combined with the high background fission fragments create, would make it impossible to distinguish the ERs without further electromagnetic sorting of the reaction products. At the JINR the separator VASSILISSA is used to identify the ER while removing unwanted background reactions, transfer and fission products and unreacted primary beam.

3.4.1 VASSILISSA

The kinematic separator VASSILISSA was installed in 1987 and was designed for the observation of heavy evaporation residues. VASSILISSA is a system which spatially separates the trajectories of recoil nuclei, multinucleon transfer reaction products and beam particles. This is done by the usage of three electrostatic dipoles where particles are separated due to differences in their energy and ionic charge.

In the first dipole, the recoil nuclei are deflected 8° while the full energy beam projectiles pass through almost unperturbed and are stopped in a beam stop, the Faraday cup. In the second and third dipole the desired ERs are further separated from scattered projectiles and other background particles. The focusing of the beam is done by two triplets of wide aperture magnetic quadrupoles. The first focusing segment is located just behind the target. It focuses the evaporation recoils knocked out from the target and shapes the recoil flux into a quasi-parallel beam. The second triplet follows the electrostatic deflection segment and serves to collect the recoils into the focal plane detector. The particles leaving the target have to be within a $\approx \pm 4^{\circ}$ angle in the vertical and horizontal directions to be accepted by the separator. The deviation of energy and charge tolerated is of the order of 15%.

The efficiency of the separator depends on the reaction. In reactions where the ERs have a similar energy and ionic charge as the unwanted products, the separation will not be as efficient as if the difference is large. When a particle has made it through VASSILISSA, it then has to be registered by the focal plane detector used. The detection of the ER is dependent on the size of the detector as the recoils exiting VASSILISSA have a relatively

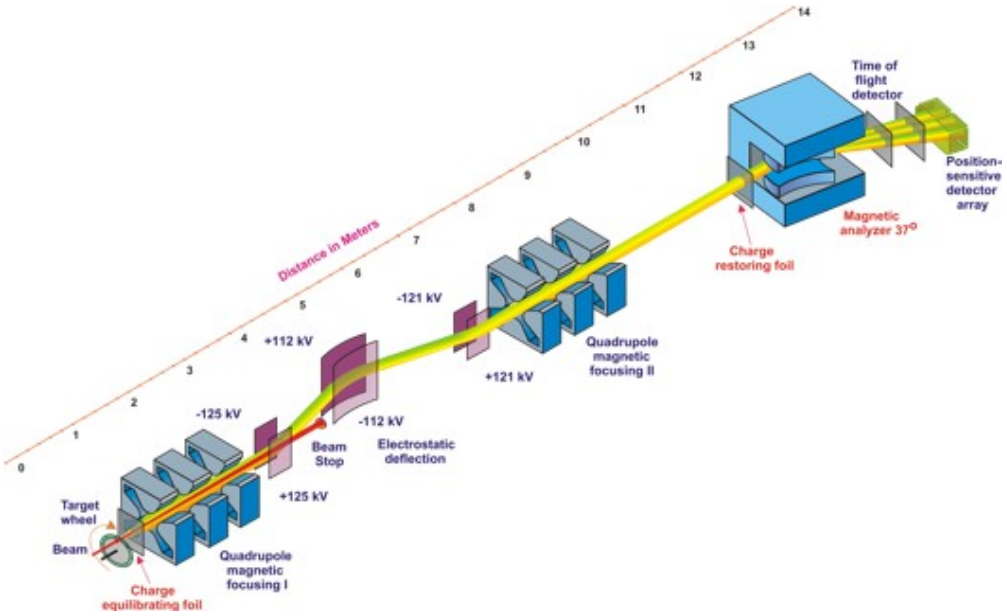

Figure 3.6: The setup of the separator VASSILISSA [10].

large spatial resolution, which results in recoils missing the detector. In this experiment the efficiency of the ER separation was 15 %, i.e. if 100 ERs were produced at the target, 15 of these were detected in the focal plane.

3.4.2 The GABRIELA detector setup

GABRIELA stands for Gamma Alpha Beta Recoil Investigations with the ELectromagnetic Analyzer VASSILISSA and is shown in Figure 3.7. It is a detector system designed to register the possible events as the nuclei of interest are implanted in the focal-plane detector and decay. GABRIELA consists of several different detectors. The recoils are implanted into a double strip silicon detector (DSSD), which is the focal plane stop detector where the kinetic energy of the recoils and its particle decay is registered. In addition to the DSSD, there are seven germanium detectors surrounding the focal plane to detect γ-rays from de-excitation, a tunnel detector that measures conversion electrons and escaped αs from the focal plane and a Time-Of-Flight (TOF) detector system that registers the speed of the recoils.

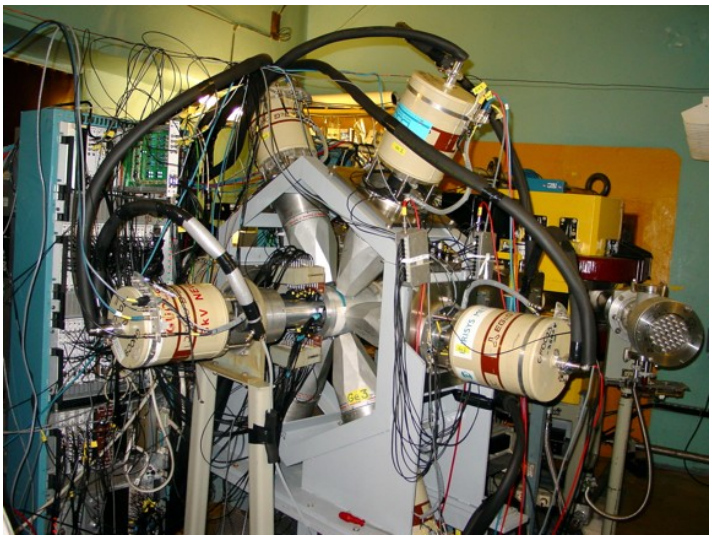

Figure 3.7: GABRIELA: Gamma Alpha Beta Recoil Investigations with the ELectromagnetic Analyser VASSILISSA [11].

Time-of-flight (TOF)

The TOF measurements are performed by measuring the time difference between the signals made by the recoil as it passes through thin gold-plated mylar foils. As the recoil passes through the foil, cascades of electrons are released. These electrons are accelerated in an electric field and bent by a magnet into an array of multichannel plates (MCP). There are four different plates. The TOF is set to be the difference in time between the signals from MCP 2 and 4 as is sketched in Figure 3.8. The passage through the TOF not only deteriorates the energy resolution but also reduces the detection efficiency as some recoils will miss the DSSD. The TOF measurements are however necessary to distinguish between recoil and α events and, combined with energy measurements, make it possible to separate ER from the background. The background is here defined as transfer, scattered beam and other unwanted products that have made it through the VASSILISSA separation.

The Double Sided Silicon Detector (DSSD)

At the focal plane the DSSD is situated. This detector is a silicon detector with a thickness of 300 μm. A silicon detector is a type of semiconductor detector. The DSSD consists of a silicon crystal, with strip sensors on each side orthogonal to each other. The strips divide the rather large area of the

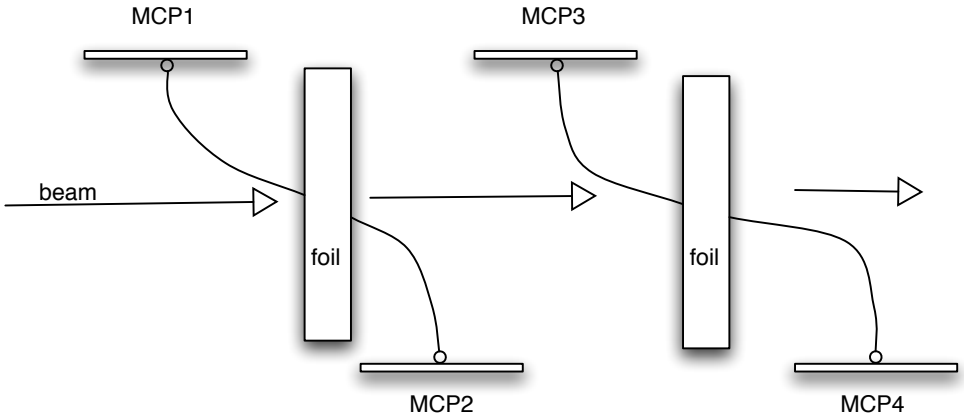

Figure 3.8: Sketch of the time-of-flight detector. As the beam passes through two foils, electrons are emitted and give rise to signals in the multi-channel plates.

detector into smaller sections. Each has its separate readout channel so that one plane measure the x and the other the y coordinate of the point of implantation. As charged particles interact with the silicon, electron-hole pairs are created along the interaction path as energy is deposited in the detector. A bias voltage is applied creating an electric field over the crystal collecting the electrons on one side of the detector (n-side) and the holes at the other (p-side) as the electrons and the holes can move through the crystal. As two signals of the same size can be detected on each side of the detector the position of the particle interaction can be determined by the location of the strip showing the signal. The DSSD used consisted of 48 strips on each side. The front of the detector has horizontal strips, giving the y-coordinate, while the strips of the back have a vertical orientation where x-coordinates can be determined. Information from 16 strips are handled by one amplifier, which makes a total of six amplifiers used.

The resolution of the DSSD is found by fitting a Gaussian to an α peak. Different background levels before and after the peak as well as bad charge collection giving rise to a low-energy tail is taken into consideration in the fitting. The ^{216}Th α peak is caused by solely the energy of the α, and is shown in Figure 3.9. The resolution, σ, is 2.48$\pm$0.009 channels, corresponding to $\sim$30 keV.

Figure 3.10 shows how the nuclei that pass through VASSILISSA hit the

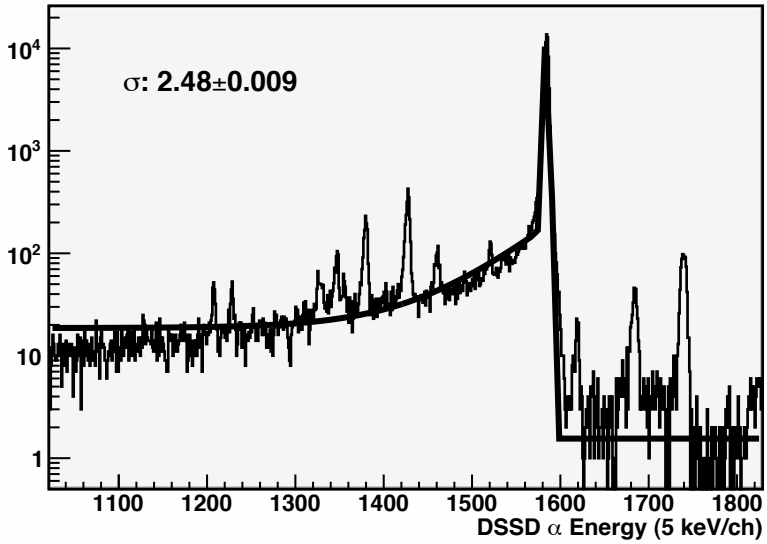

Figure 3.9: Resolution of the DSSD detector.

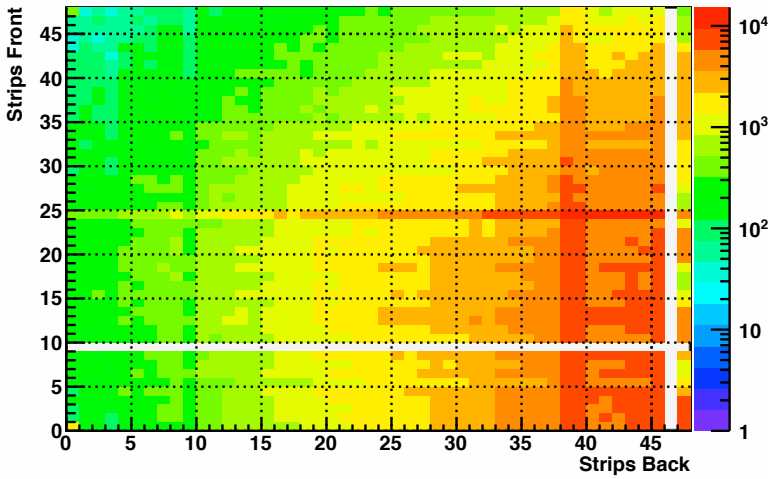

Figure 3.10: Scattered beam and recoils on the DSSD.

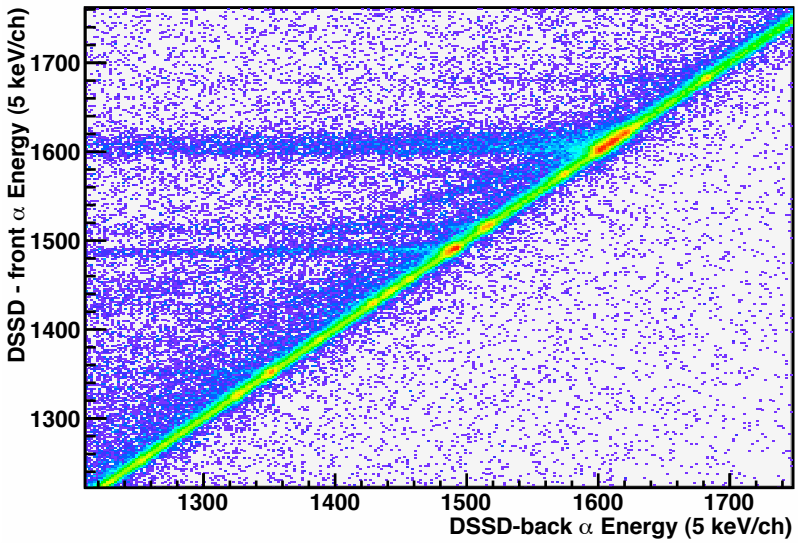

Figure 3.11: Energy detected in the front and back of the DSSD. An ideal detector system should have all count on the diagonal line, where energy detected in the back is equal to the energy detected in the front.

DSSD. The counts represent the amount of hits registered as recoils in each pixel in the DSSD. Some whole strips may have less or no counts. This is caused by missing channels or slight differences in thresholds or noise. The scattered beam is hitting the detector in the lower right corner.

Figure 3.11 shows the energy detected in the front and the back strip for correlated front and back signals. Ideally the same amount of energy should be detected in the front and the back of the DSSD. The energy registered may not be the full energy of the signal which leads to loss of statistics. Reasons for the variation of energy detection for the front and back side of the DSSD are discussed in Appendix D. In general, there is a larger probability that the energy registered in the front side of the DSSD is the full kinetic energy. The energy detected in the front is the value used.

The tunnel detector

Surrounding the DSSD stop-detector in the direction of the incoming recoils is a tunnel of silicon detectors. The tunnel detectors used where segmented Si detectors with 32 strips chained 4 by 4. These detectors where used to measure emitted particles escaping the stop detector. The escaped

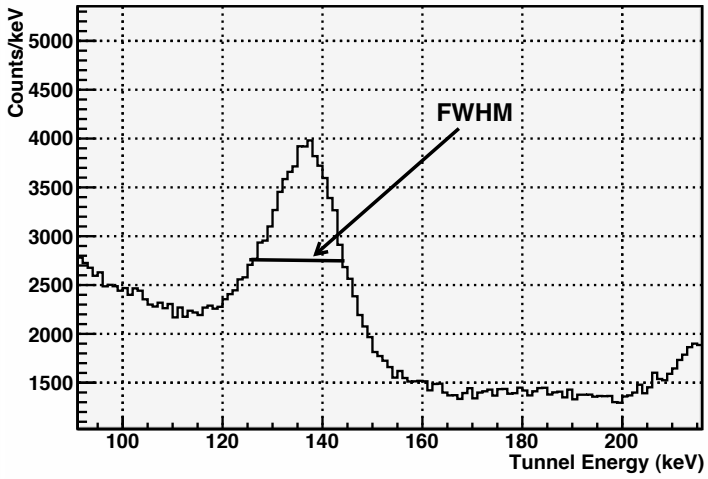

Figure 3.12: In-beam electron resolution of the tunnel detector at 135 keV. The resolution given is the value of the Full Width Half Maximum (FWHM), and is found to be $\sim$ 20 keV.

particles consist primarily of conversion electrons, but also α, β and fission products are present. A large portion of these particles will be detected at short distances from the stop detector. The particles detected close to the DSSD detector will have suffered more straggling than particles detected further upstream, as the particles detected close to the DSSD will in general have travelled further in the stop detector. The effect of straggling on the energy resolution has been shown, by using Geant4 simulations [11], to be smaller compared to the degradation expected from the leakage current of the detector. For electrons with energies above 500 keV, implantation depth will have almost no effect on the straggling. As electron energies are reduced below 100 keV, the detection efficiency and resolution will be reduced due to the straggling effect. With energies under 50 keV straggling will cause a major effect. To reduce the lower detection limit and increase the resolution at low energies, it is possible to place a degrader foil in front of the stop detector to reduce the implantation depth. Leakage current can be minimized, thus improving the energy resolution, by cooling[5] the detector. This was however not done due to the usage of a chamber with no room for fluid inlet/outlet. The lack of cooling caused the in-beam resolution obtained to be worse than usual: 20 keV at 135 keV instead 10-11 keV obtained in previous experiments where cooling was used. The reso-

[5]Alcohol of temperature -40°- -80° is normally used as coolant.

lution, given by the full width half maximum (FWHM), was found to be $\sim$ 20 keV and is shown in Figure 3.12.

Germanium detectors

The focal plane stop detector is surrounded by seven Ge detectors. Six of these γ detectors are placed inside BGO Compton shields and form a ring around the detector chamber with a focal point on the upstream side of the stop detector. The suppression shields serve two purposes. The first is to improve the peak to total ratio by vetoing events for which a γ-ray undergoes Compton scattering out of the Ge detector. This method makes it possible to identify weak lines in the spectrum, which otherwise would have been buried under the Compton background of more intense lines. The second purpose is to reduce background events. This is done by vetoing events for which γ-rays emitted from the concrete walls (mainly ^{40}K) interact in the germanium detectors. The seventh detector, called "Shorty", is placed as close as possible to the stop detector. To increase its proximity to the focal plane detector, the distance between the Ge-crystal and the Al end-cap has been reduced from $\sim$ 4 cm to $\sim$ 5 mm. The resolution of the germanium detectors where found using a γ ray source, and gives a $\sim$ 2.0 keV FWHM value at 222 keV.

Efficiency of germanium and the tunnel detectors

The efficiency of a detector, ϵ, is energy dependent and can be found by looking at the relationship between the amount of radiation the detector is exposed to in a time period, I_{real}, to the amount detected, $I_{experiment}$. The relationship between the variable is:

$$I_{experiment} = I_{real} \cdot \epsilon(E) \tag{3.11}$$

The efficiency of the detection of electrons is given in Figure 3.13. The simulation was done in 2004 [11], where the dimensions of the tunnel detector where 50x50 mm^2 with a 500 μm thickness. The tunnel used in this experiment has an area of 61x61 mm^2 and with two sides with a thickness of 740 μm and 715 μm and two with 1 mm. As seen in Figure 3.13, the efficiency of the new setup is higher than the 2004 simulations. As the area of the detector is increased, the efficiency of the detector also will increase. The thickness of the detectors will influence the variation of efficiency with radiation energy. Electrons with higher energy reach further into the detector. By increasing the thickness of the detector, the probability of detecting high-energy electrons will be improved. The updates of

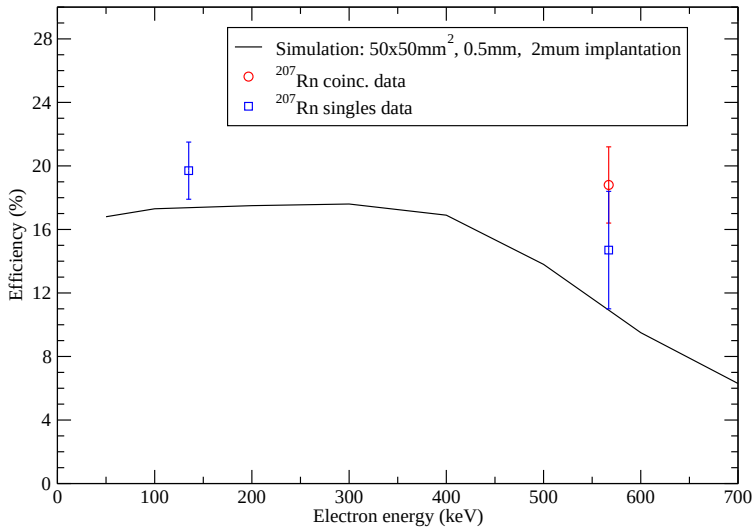

Figure 3.13: Efficiency of the tunnel detector. The 2007 measurements give the experimental value of the tunnel used in this work, while the 2004 simulations where based on a tunnel with other dimensions. Courtesy of Lopez-Martes.

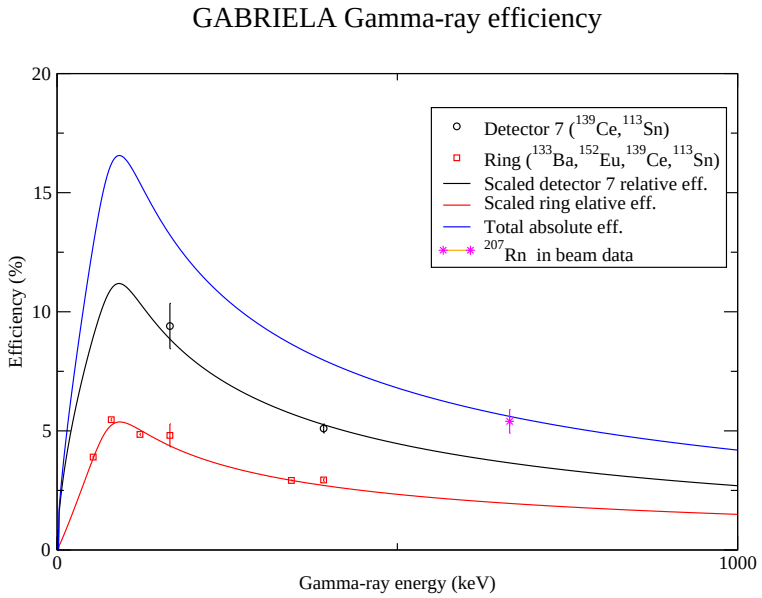

Figure 3.14: Gamma-ray efficiency as a function of energy for the GABRIELA set-up. Courtesy of Lopez-Martes.

the tunnel detector from the simulation gives rise to the effects discussed, as can be seen in Figure 3.13. The efficiency of the tunnel detector is approximately constant within the electron energy range of interest in the reactions discussed in this thesis, and will therefore be set to a fixed value:

$$\epsilon_e(E) = 18\%. \tag{3.12}$$

Figure 3.14 shows the efficiency of the γ detectors. The spectrum is obtained by looking at the variation of radiation detection at different energies to get the shape of the efficiency curve before determining the real efficiency distribution by fitting the curve to measured detector efficiency at certain energies. The efficiency of the γ detection will vary strongly with the energy of the photon and can be read off from the data of Figure 3.14.

3.5 Data processing

To be able to extract information from the recorded data, I had to write a sorting program. The program was written from scratch, using C/C++

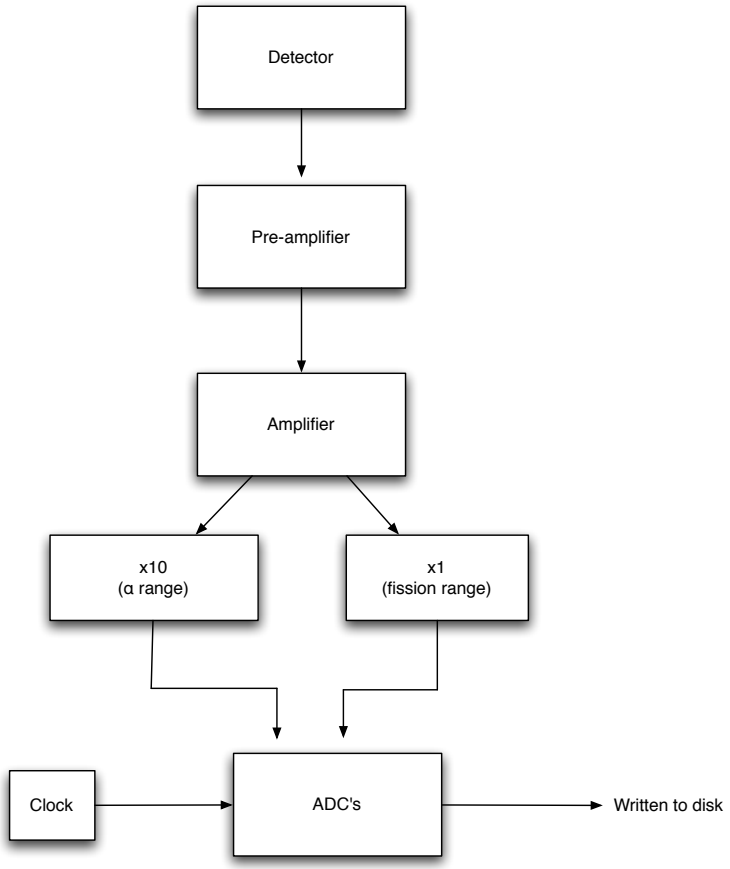

Figure 3.15: Sketch of the electronics setup used.

with ROOT [12] functions. The following sections give a description of the raw data and the general structure of the program.

3.5.1 Total data readout

Figure 3.15 shows a simple sketch of the hardware used. For the particle detectors, a signal of strength proportional to the deposited energy is registered in a detector. The voltage signal is given a first amplification in a pre-amplifier and is at this point represented by an electric pulse. The height of this pulse is related to the energy deposited in the detector. The pulse is then further processed in the hardware to give it a shape where the amplitude of the pulse can be determined. In the process of shaping the signal, a shape time is set. With longer shape time, the signal will be delayed, but higher energy resolution is obtained. Before such an analog

Figure 3.16: The data is stored in a section consistent of five words.

signal is converted to a digital one, the signal is further amplified if this is desired. In the analog-to-digital converter (ADC), the event is marked with a time-stamp provided by an external clock. The signal is now consisting of the information of data stored, detector of origin and time. The data is stored in a temporary storing unit. Several units were used to store the data from different detector sections (γ, tunnel, DSSD, TOF). In the electronics, no event-builders where incorporated so the data is directly written to disc when the temporary storing sections are emptied. When sorting the data, the code has to take the possible randomness of the data-stream into consideration. Due to no event building and several locations for storing, events occurring in a given (true) time order may not be written in chronological order in the data stream.

There are 5 words written to disk per event registered. Figure 3.16 shows a sketch of the words with information type marked. The fist word, *type*, is a number between 0 and 47 representing the ID of a given ADC. The list of the ADSs used is given in Appendix E. The 2 next parts of information represent the time stamp. The time is given in two words, a low time *gts*, and a high time, *gth*. The timestamp for the event is found by the relationship

$$time = gth \cdot 65536 + gts, \tag{3.13}$$

where 65536 is the maximum count number of the clocks. At 65536 the ghs will reset and gth will be increased with one. When the high time reaches this number this clock will also reset. One tick on the clock is one μs in time. The time stamp is divided into high and low time as the total time may lead to overflow of the variable. The fourth word, *fission*, is only in use for detector segments that require more than one level of amplification for the same signal. Signals of one amplification is given in this variable, while another is given in the word *ener*. This 5th word is in general the variable where the signal from the detector is stored, this being the energy, TOF or other information the given ADC is set to collect. The need for

radiation	Energy range
α	5-10 MeV
recoil	10-50 MeV
fission	$<$ 250 MeV
con. electrons	30 - 500 keV
γ	20 keV - 2 MeV

Table 3.2: Energy range for signals of interest. The effective energy range for recoils will in reality not extend far beyond 20-25 MeV as discussed in Appendix D.

several amplification ranges is demonstrated in Table 3.2, where the energy range for the recoils and the different decay modes are shown. As the energy region of interest varies, the different detectors have different amplification to best see the desired signals. In the tunnel detector and the DSSD, two different amplifications are used to accommodate 2 different energy ranges. In the tunnel, the conversion electrons are of interest, but α particles escaping the DSSD will also be implanted into the tunnel. The electron range in the tunnel has x10 the amplification of the tunnels α range. The DSSD originally had an α and a fission range. The energy range of the recoil is within the same amplification as the α due to effects in the DSSD as discussed in Appendix D. In the later run, the amplification of the DSSD was altered, obtaining α and electron ranges by the adding a second pre-amplification stage.

The data is originally in binary format. In the following section, the numbers shown in the left column is data from a part of the data stream. One line shows the information given from one registered event. To get the correct data, two and two numbers of each word have to be swapped as can be seen in the column to the right.

Raw	Swapped
07 00 bd 75 90 6c c7 75 15 08	00 07 75 bd 6c 90 75 c7 08 15
07 00 d8 78 90 6c e2 78 a8 08	00 07 78 d8 6c 90 87 e2 02 a0
15 00 7c 7b 90 6c 86 7b a0 02	00 15 7b 7c 6c 90 72 86 02 a0
19 00 00 80 45 9d 57 3a 90 6c	**00 19 80 00 9d 45 3a 57 6c 90**
07 00 8c 83 90 6c 96 83 4e 04	00 07 83 8c 6c 90 93 96 04 4e
07 00 61 85 90 6c 6a 85 f0 03	00 07 85 61 6c 90 85 6a 04 4e
18 00 85 87 90 6c 8f 87 8d 01	00 18 87 85 6c 90 87 8f 01 8d

18 00 aa 88 90 6c b3 88 57 0e	00 18 88 aa 6c 90 88 b3 0e 57
07 00 eb 9a 90 6c f5 9a 2f 03	00 07 9a eb 6c 90 9a f5 03 2f
07 00 29 9f 90 6c 33 9f 7d 03	00 07 9f 29 6c 90 f9 33 03 7d
1b 00 19 a0 90 6c 22 a0 fa a0	**00 1b a0 19 6c 90 a0 22 a0 fa**
1e 00 19 a0 90 6c 1e 80 8e 80	**00 1e a0 19 6c 90 80 1e 80 8e**
07 00 1c a0 90 6c 2e a0 74 05	00 07 a0 1c 6c 90 0a 2e 05 74
07 00 78 a1 90 6c 82 a1 7c 07	00 07 a1 78 6c 90 a1 82 07 7c

The data has to be monitored as, for instance, a cable giving the time to one of the ADCs may loosen during the run. By using a hexadecimal form[6], time errors are relatively easy to detect. The time for the signal marked from ADC 00 19 is off: the high time is 9d 45 while the previous and following ADC data have a lower high time 6c 90, indicating an error of the clock. In the section given, the only signal of interest is the 00 1b (ADC 27) and 00 1e (ADC 30) and the accompanying TOF signal. ADC 27 gives a recoil signal registered in the front of the DSSD and ADC 30 is giving the corresponding back signal. There are TOF signals before and after the recoil in the data stream. In this case, the time difference to the TOF before the recoil in the data stream is 240 μs while the TOF event following the event is registered 3 μs after the DSSD event. The recoil is always correlated to the TOF closest in time.

The majority of the data written to disc is not of interest, as is the case for TOF signals from scattered beam and signals from background γ-rays. The sorting program is designed to detect the relatively few events of interest from the masses of data without relevance for the analysis. The following four lines are the type of data the sorting program is searching for.

Raw	Swapped
02 00 ac be 18 e4 7c b0 d6 b4	00 02 be ac e4 18 b0 7c b4 d6
04 00 ad be 18 e4 7e b0 d4 b4	00 04 be ad e4 18 b0 7e b4 d4
18 00 bb be 18 e4 c2 be 29 02	00 18 be bb e4 18 be c2 02 29

[6]The hexadecimal system is a numeral system with a base of 16 with symbols 0-9 representing the first 10 values and a-f giving the values 10-15. (a=10, b=11, etc). Transformation from a number of base-16 to a base-10 is done, as b=11 and d=13, by:

$$75bd = (7 \cdot 16^3) + (5 \cdot 16^2) + (11 \cdot 16) + (13) = 30141 \tag{3.14}$$

stripID	ADC 1(4)	ADC 2(5)	ADC 3(6)
0	0	1	2
1	6	7	8
2	12	13	14
3	18	19	20
4	24	25	26
5	30	31	32
6	36	37	38
7	42	43	44

Table 3.3: Physical strip numbers a function of ADC channel number stripID (for stripID-=0-7) for different ADC modules. The ADC number in bracketed indicates the type for the back face of the DSSD.

17 00 b2 be 18 e4 c8 be 3b 01 00 17 be b2 e4 18 be c8 01 3b

The first two events, with type 2 and 4, are signals from the front and back of the DSSD. The signals are in coincidence, with 1 μs between them. The position of the implantation and decay is given in the data stream by two variables: $type$ and $stripID$. The type-number represents an ADC module. Signals from the front are marked by type 26, 27 and 28 for the recoil event and 1, 2 and 3 in the case of detection of an α particle. The readings from the back are given by the type 29, 30 and 31 for recoil and 4, 5 and 6 for α, making the signal in the example an α-event. The stripID-number correspond to the channel number of the ADC, as 1 ADC handles the data from 16 physical strips in the DSSD. The correspondence between stripID and physical strip number is not straightforward as no 3 neighboring strips are handled by the same ADC. The numbering scheme is illustrated in Table 3.3 and Table 3.4. In sorting the data, an event registered in a position x (signal from the back), y (signal from the front) in the DSSD, is placed in the same position in matrices that virtually represent the real detector. The following is the algorithm used to find the physical position of the origin of an α signal.

```
int strip[8]={8,9,10,11,12,13,14,15};
int place[8]= {1,3,5,7,9,11,13,15};

Front:
if ( type <4){
```

stripID	ADC 1(4)	ADC 2(5)	ADC 3(6)
8	3	4	5
9	9	10	11
10	15	16	17
11	21	22	23
12	27	28	29
13	33	34	35
14	39	40	41
15	45	46	47

Table 3.4: Physical strip number s a function of ADC channel number stripID (for stripID-=8-16) for different ADC modules. The ADC number in bracketed indicates the type for the back face of the DSSD.

```
if(stripID<8){
IDF=(type-1)+(6*stripID);  //strips 0-7
}
if( stripID>7 && stripID<16){
for(int i=0; i<9; i++){      //strips 8-15
if(strip[i] == stripID){
int a= place[i];
IDF=(type-1)+(3*a);
}//end if
}//endfor
}//end else

Back:
if (3<type && type<7){
if(stripID<8){
IDB=(type-4)+(6*stripID); //strips 0-7
}if(stripID>7 && stripID<16){
for(int i=0; i<9; i++){          //strips 8-15
if(strip[i] == stripID){
int a=place[i];
IDB=(type-4)+(3*a);
}//end if*/
}//end for
}//end else
```

For the first 8 strips, stripID and type can be used directly to calculate the real position of the signal, while the variables *strip* and *place* must be used to calculate the position of $stripID > 7$. The calculated strip from the front of the detector is named IDF while the strip position of the back is named IDB. In the example from the data, the first signal of the α is from the front side of the DSSD as the type given is 2. The stripID is the first symbol of the fifth word, b=11, for the particular signal. The physical strip numbers in the front and the back of the DSSD are given by:

$$IDF = (2 - 1) + (3 * 7) = 28$$

and

$$IDB = (4 - 4) + (3 * 7) = 21.$$

The pixel where the decay occurred is thus found to be (21,28). The energy of the α is given in the 4th word (fission-range) and 5th word (α-range) and is coded in 12 bits. The channel of the α-range detected at the front is 4d6=1238, while the channel number registered in the fission-range is 124, which is roughly a tenth of the α range. The amplifiers gains have been tuned so that 1 channel $\sim$ 5 keV(α-range), giving an α energy of 6190 keV. The last two events of types 18 and 17 corresponding to the ADCs 24 and 23 are both signals from γ-ray detectors. The four data signals are in coincidence, though their times vary within 6 μs. The main reason for the time variation of originally coincident events is the late stage in the hardware where the time stamp is given. The time stamp is tagged to the signal at the time of peak determination in the ADC. Different processing times of the signals in the ACDs affect the time stamp given and have to be corrected for in the sorting code. In addition to this, it is worth mentioning the use of the relatively coarse time intervals of μs. The GABRIELA system was not created for γ-ray spectroscopy but made for detection and life time determination of SHEs for which the time step intervals are sufficient. If the time stamp was given at an earlier point in the data processing, the time window for coincident events would be drastically improved but still be of the order of several μs. The width of the coincidence window needed strongly affects the amount of random correlations made in the sorting.

3.5.2 Event correlations

Prompt coincidences

The different correlations studied for coincident event are as follows:

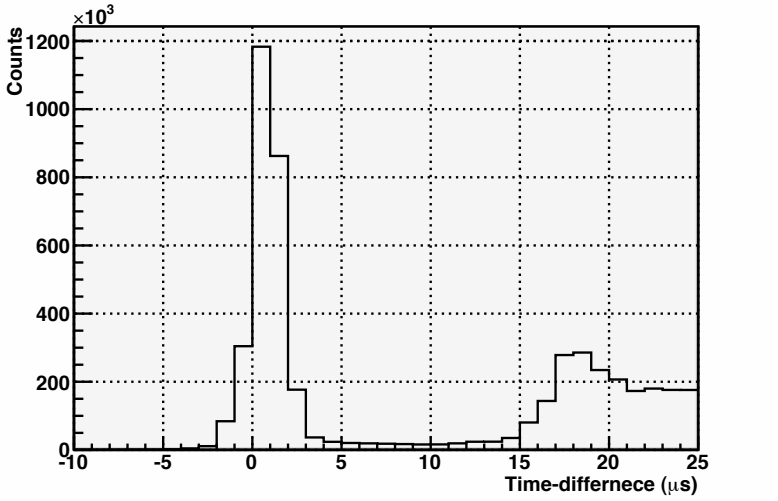

Figure 3.17: Time difference between 2 events registered in the tunnel detector. The peak centered around 0 μs represents coincident events.

α-γ and α-electron. By looking at electrons and γ-rays emitted at the same time as an α particle, one can see the transitions in the excited daughter nucleus. To ensure that all events are found, correlations are looked for each time an α and γ or electron is detected. The events are correlated by setting a time gate in the software.

electron-electron, γ-electron and γ-γ. For these correlations a time gate between the two last γ-rays or electrons detected, or the last γ-ray and electron, has been applied.

α- γ-γ, α-electron-electron and α-γ-electron. In addition to a requirement of time correlation between, e.g., two electrons, a further requirement on the time correlation with an α is set.

Position and time correlations

The required time gates are found by plotting the time difference between the events of interest as shown in Figure 3.17 in the case of 2 events registered in the tunnel detector. The peak in the figure centering around $\sim$0 μs arises due to coincident events. The time gate set for electron-electron correlations is $\pm$ 3 μs.

To find the lifetime of a nuclear state and to calibrate the tunnel detector, the time between implantation and decay is plotted as a function of decay energy. This is done both for the detection of α decay in the DSSD, by position correlation, and for electrons in the tunnel.

In the later runs of the ^{48}Ca beam on the ^{207}Pb target, an extra preamplifier was added to the front-end detector of the DSSD. By doing this, information about fission was lost in these runs, but a low-energy signal from conversion electrons can be observed. Detecting conversion electrons in the DSSD hasproven to be an efficient way of searching for isomer decays [13]. Unfortunately, as only the front strips were equipped with added amplification, no signal for these low-energetic electrons were detected at the back strip, resulting in the loss of the y-coordinate. Although the data obtained by doing this could not be used in the isomer analysis, the proof of principle was demonstrated.

3.5.3 Analysis program

The structure of the sorting program is sketched in Figure 3.18. As data is read, it is first sorted according to which detector the signal originated from and sent to its respective function. There are different functions for the different detector segments.

Recoil

An event is tagged as a recoil when a signal from the DSSD detector is registered with a gate in hardware triggered by a signal from TOF detector. The function handling these events identifies the position of the signal, sets requirements on time correlation of the signal from the front and back and stores the information in variables for later use.

Alpha

Figure 3.19 shows the steps done in the code each time an α is detected. As for recoils, when an α signal is detected in the DSSD, the front and back signals are paired with the signal from the opposite face of the detector by time correlation if the energy of the signals are above a set threshold. The energy of the front is then calibrated and the x and y coordinates of the signal is determined. To be able to find the lifetime of ERs, the time between implantation and decay has to be determined. The α particle has a relatively short range, and is likely to be detected in the same pixel as

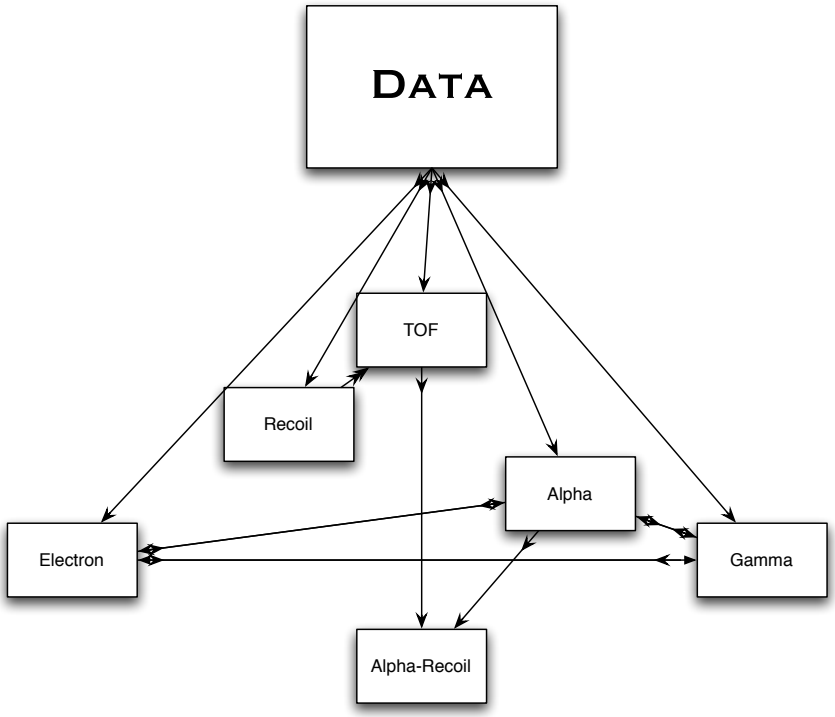

Figure 3.18: Structure of sorting program for correlation of prompt decays and mean decay times. The recoil-α correlations are made in the function marked 'Alpha-Recoil' after the recoil is paired with correct TOF value.

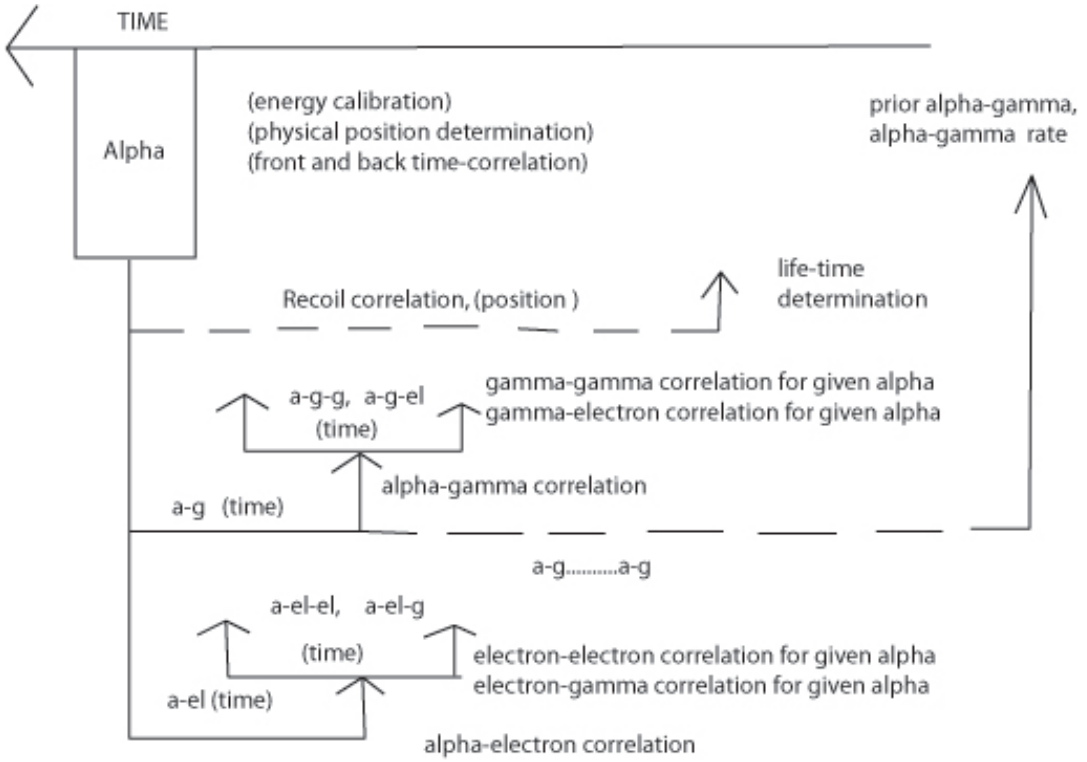

Figure 3.19: Schematic representation of actions taken in the sorting program when an α signal is detected.

where the ER was implanted. By making a matrix where the time between implantation and decay in the same pixel is saved as a function of α energy, and provided the half-life are such that the probability of another recoil being implanted in the same pixel is low, one can identify the ER by its decay and determine the half-life of the nucleus. When a nucleus α-decays, if the daughter is left in an excited state, prompt emission of γ-rays and/or conversion electrons will follow[7]. The electrons and γs may be registered before the α in the data stream. The time-stamps of the last γ and electron registered are compared to the time of the α to correlate the decays. It is also interesting to look for cascades. If the last γ or electron is found to be in coincidence with the α, also prior electron and γ signals are tested for time correlations. To be able to determine the random rate of coincidences, the rate of α-γ coincidences need to be determined. When two coincident events are found, the time since the last event-correlation of this type is noted and an average time between the events can be estimated.

Time-Of-Flight (TOF)

The TOF of a recoiling ion combined with the measure of its kinetic energy in the DSSD can improve the background rejection of unwanted reaction products and scattered beam. This is important for the determination of half-lives and possible isomeric states. The problem with connecting the right TOF to the recoil is that the TOF-value comes after the recoil in the data stream and the TOF detector has the highest rate. This problem has, in this sorting code, been solved by saving all TOF values within a fixed timeframe. The method used is sketched in Figure 3.20.

When a TOF is detected in the data stream, the time difference to the last recoil detected (box marked *Recoil* in Figure 3.20) is tested. If the TOF is within the time window set, the value is temporarily stored as is indicated by the gray boxes. When a TOF signal is found to be outside the time gate, indicated by the blank box, the TOFs saved with the lowest time-stamp is correlated to the recoil. The same procedure is followed if a new recoil is registered before TOF correlation of the previous event, taking into account the possibility of RECOIL-TOF...RECOIL- sequences in the data stream.

When the right value of TOF is connected to its recoil, a recoil-TOF relationship can be determined by finding the desired ERs (good recoils) in

[7] Assuming the excited state in the daughter is not an isomeric state.

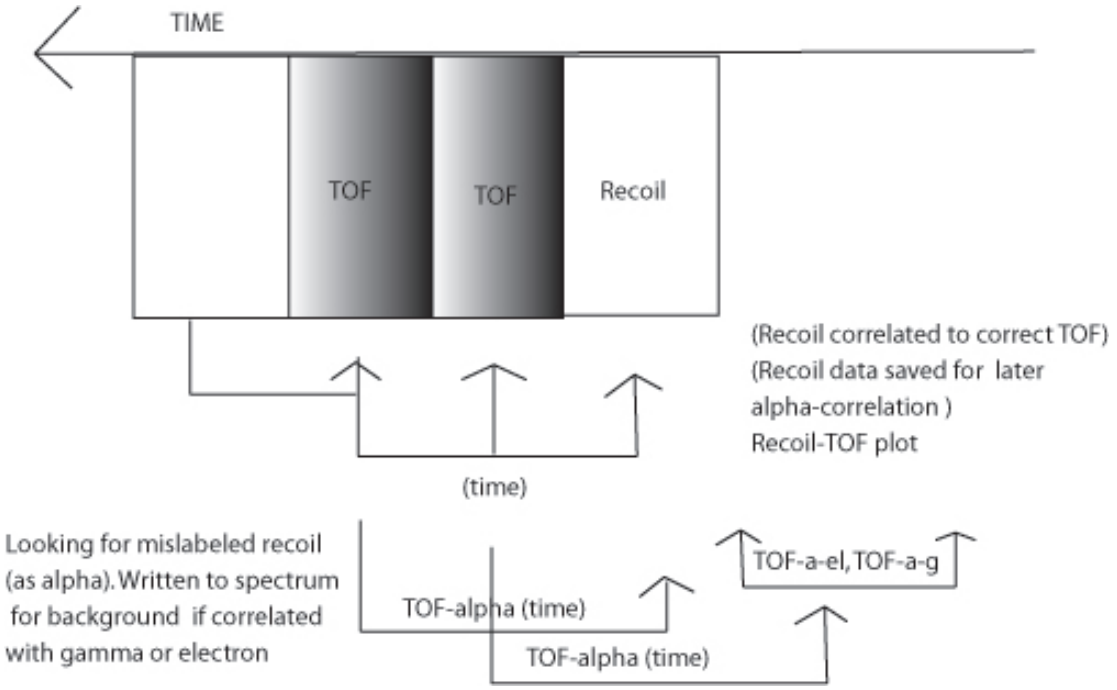

Figure 3.20: Schematic representation of actions taken in the sorting program when the TOF detector registers an event.

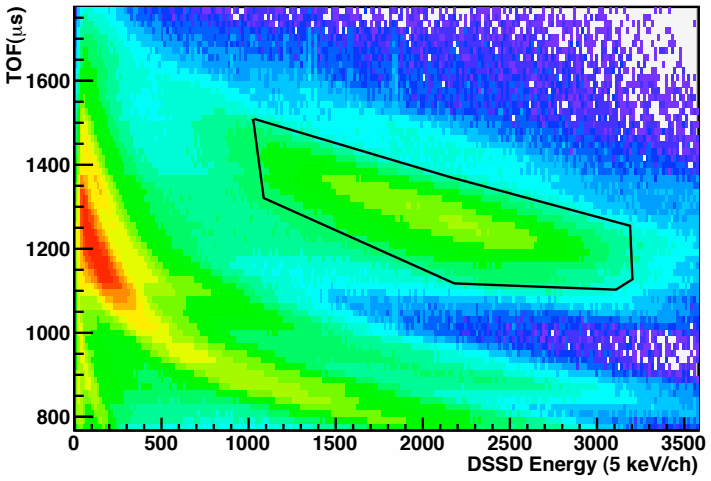

Figure 3.21: Cut of good recoils for ^{48}Ca on ^{174}Yb run.

the plot and making an appropriate cut, as is indicated in Figure 3.21 for the ^{48}Ca on ^{174}Yb run. In later runs of the sorting code, only recoils with an energy-TOF relationship within the cut will be used.

In the hardware, recoils are gated by the presence of a TOF in coincidence. While this in general works, sometimes the gates do not trigger as they should resulting in recoils being registered as αs. The TOF signal may, though being overlooked as a gate in the hardware due to timing problems[8], still have been registered and written to file. If this is the case, further gating can be done in the code to reduce the background as random events in the germanium and tunnel detectors are correlated to mislabeled recoils. The software gating is done, when a TOF is detected, by looking back in time for an α within the time window set for correlation. If such an "α" is found, the event is written to a ROOT matrix if it is in coincidence with a γ or electron. These background matrices can later be subtracted from the α-γ and α-electron correlation spectra.

Tunnel and γ detectors

Signals from the germanium and tunnel detectors are processed in their respective functions in a similar fashion. The sketch in Figure 3.22 is valid for signals detected both in the tunnel and the γ detectors. The correlations made are in general the same as when an α is detected, as the correlations have to be made for every possible ordering of events in the data stream.

When a γ is detected, it is tested for time-correlation to the last α detected. If a coincidence is found, possible further coincidences are looked for in the prior γ detected and the last electron registered. The originally detected γ signal is also tested for coincidence with prior γ and if found, further with respect to α and electron signals to get the γ-γ-α/electron correlations. Similar correlations are looked for in the event of γ-electron-γ/α. The time between two γ events is also registered to be used for γ rate determination.

Similar correlations are made in the tunnel detector, looking for electron-α-electron correlations and so on.

[8]The gate arrives too late.

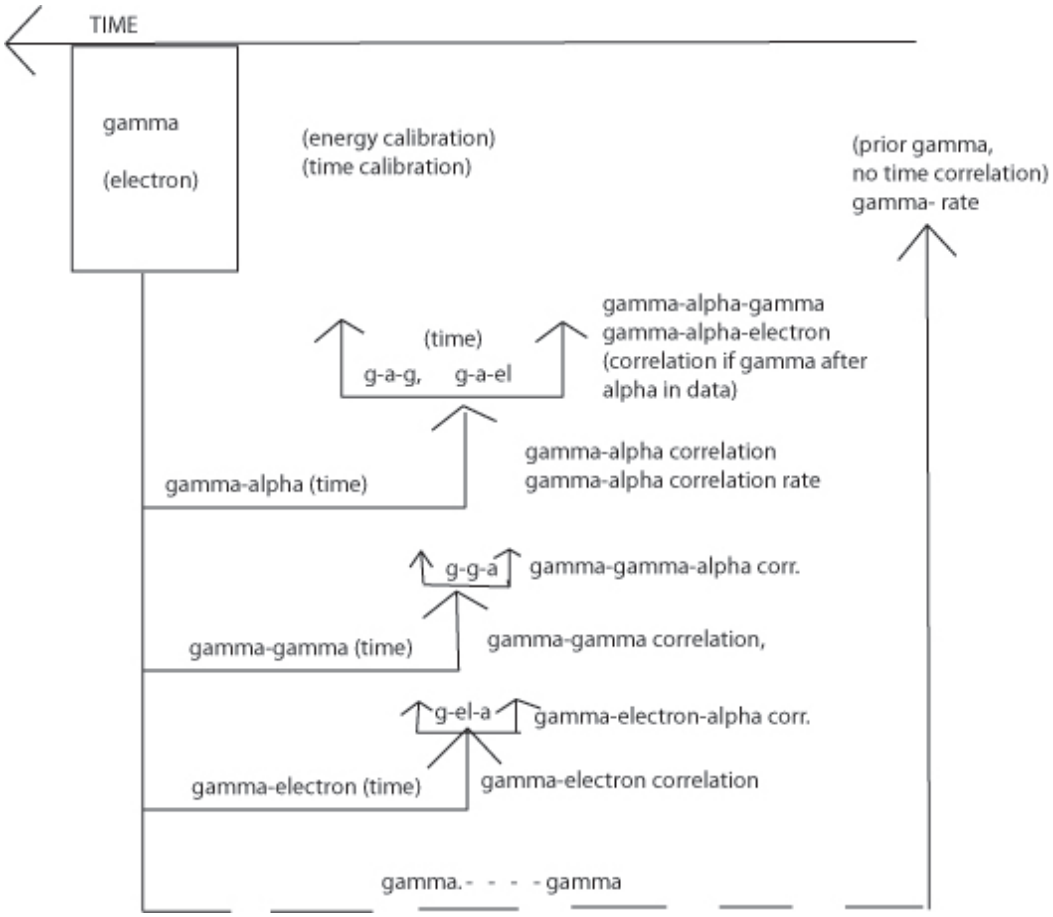

Figure 3.22: Correlations looked for in the sorting code when a γ-ray or electron is detected.

3.6 Calibration

3.6.1 Energy

There are three different parts of the GABRIELA setup that must be calibrated; the focal plane detector, the γ-ray detectors and the tunnel detector. To be able to calibrate these different parts it is necessary to use three different sources. For the calibration of the tunnel and the DSSD it is important to calibrate in beam, thus implanting the source in the silicon detectors. By reproducing the energy deposition of a run, effects like the energy loss of ΔE caused by interactions in the entrance window of the detectors and straggling of electrons in the DSSD before escaping will be identical in the calibration and the runs. The focal plane detector strips are calibrated by producing known α emitting nuclei and implanting them into the DSSD. The γ detectors surrounding the focal plane detector are calibrated with a γ source, while the calibration of the tunnel detector, nuclei that emit conversion electrons implanted in the DSSD.

The detectors are calibrated by finding the position of the known peaks and using linear regression to find the offset and gain for each strip. This is done by using the linear relationship

$$E = a_0 + a_1 \cdot Ch \tag{3.15}$$

where E is the energy of the particle or γ ray, Ch is the channel where the energy is registered, a_0 is the offset and a_1 is the gain. The calibration assumes an approximately linear response of the detector with respect to energy in the energy range of interest. A linear approximation is a very good approximation for the electronics used.

Calibration of the focal plane detector

For the calibration of the DSSD, the well-known reaction used was a ^{48}Ca beam on a ^{174}Yb target, creating the compound nucleus of ^{222}Th. This compound nucleus is highly exited and will evaporate particles. The mid-target beam-energy, E_{beam}, used in this experiment was approximately 220 MeV.

The projectile, ^{48}Ca, has a mass of 47.952533 u[9]. The compound nucleus created, ^{222}Th, has a mass of 222.0184541 u and the mass of ^{174}Yb is 173.938859

[9]The atomic mass, u, is given as: 1u=931.502 MeV/c^2.

u. The equations (3.1), (3.3) and (3.9) are classical expressions that can be used to calculate the excitation energy of the compound nucleus in the case where $v \ll c$ [10]. The velocity of the projectile can be found by solving equation (3.8) with respect to $v_{projectile}$, resulting in the expression:

$$v_{projectile} = \sqrt{\frac{2\Delta E_{kin}}{m_{projectile}(1 - \frac{m_{projectile}}{m_{CN}}) \cdot u}} \tag{3.16}$$

The velocity obtained by this equation is given in units of c. For the calibration run, the velocity of the projectile is found to be $\sim 0.1c$. As $v \ll c$, the compound excitation energy can be calculated as follows:

The kinetic energy is:

$$\Delta E_{kin} = 220(1 - \frac{47.952533u}{222.0184541u}) \approx 172\text{MeV}. \tag{3.17}$$

The change of mass is

$$\varphi_{fus} = ((47.952533u + 173.938859u) - 222.0184541u)c^2 \tag{3.18}$$

$$\approx -0.127u \cdot c^2 = -0.127 \cdot 931.502 = -118\text{MeV} \tag{3.19}$$

giving the excitation energy of the compound system:

$$E^*_{CN} = 54\text{MeV}. \tag{3.20}$$

The average binding and kinetic energy of the evaporated neutrons is about 10 MeV[11]. Due to the fact that neutrons do not have to fight their way through a Coulomb barrier, they are in general[12] the most likely particles to evaporate. Other possibilities are one proton and several neutrons evaporating or the emission of an α particle. The available energy for evaporation is approximately 54 MeV, which indicates evaporation of 5-6 nucleons. Possible candidates for recoils produced in the reaction are given in Table 3.5.

To calibrate the spectrum, it is first necessary to identify the α lines. This is

[10] The velocity of the projectile, v, must be approximately 0.1c or smaller where c the speed of light.

[11] $\sim$8 MeV binding energy + $\sim$2 MeV kinetic energy.

[12] In some cases α channels may be dominating.

	energy α	half-life $t_{1/2}$
^{218}Th	9666	109 ns
^{217}Th	9250	0.252 ms
^{216}Th	7921	0.028 s
^{217}Ac	9650	69 ns
^{216}Ac	9072	0.33 ms
^{218}Ra	8389	25.6 μs

Table 3.5: Isotopes likely to be created by a ^{48}Ca beam on a ^{174}Yb target with the beam energy used. The nuclei decay through α decay with the given energy and half-life.

done using the α-energies from the α-recoil correlated events and matching them to their half-lives. The flight time through the separator is in the order of μs. Nuclei with half-lives less than a few μs will therefore most likely not be seen in the spectrum. Figure 3.23 and Figure 3.24 show the decay schemes of the possible created recoils. Though α evaporation is present, the evaporation of neutrons is by far the dominant channel giving a high production yield for thorium recoils. In the decay schemes the lifetimes, type of decay and α energies are indicated. The number in parenthesis is the yield of the decay type or probability of an α of the given energy being emitted.

To check the identification of the ERs, their associated decay times are used. The time difference between recoil implantation and subsequent α decay as a function of decay energy is plotted in Figure 3.25. The lines at different positions in the y-direction in the spectrum corresponds to different half-lives of the nuclei. In Figure 3.25, a long search time between recoil implantation and α decay is used, which results in a band of random correlations at large times. This effect is caused by correlating the α decay with the wrong recoil implant signal. This may be the case if the recoil and the α are detected in neighboring pixels, the recoil is not tagged and registered as an α or the mean lifetime is too long resulting in random correlations. Another effect seen in the figure worth mentioning is the curving of the lines at low times. If the time between the implantation of the recoil and its α decay is too short, the energy of the α particle will artificially be increased or decreased due to overshooting or undershooting of the corresponding amplifier signals. For calibrating, peaks that are

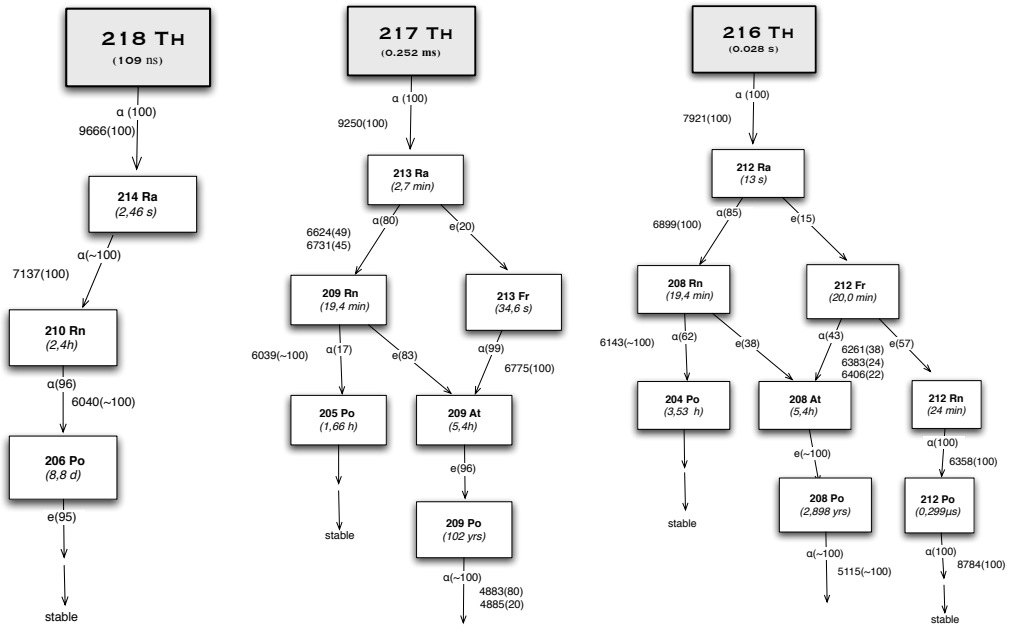

Figure 3.23: Decay chains with origin in ER likely to be produced in the calibration run by neutron evaporation.

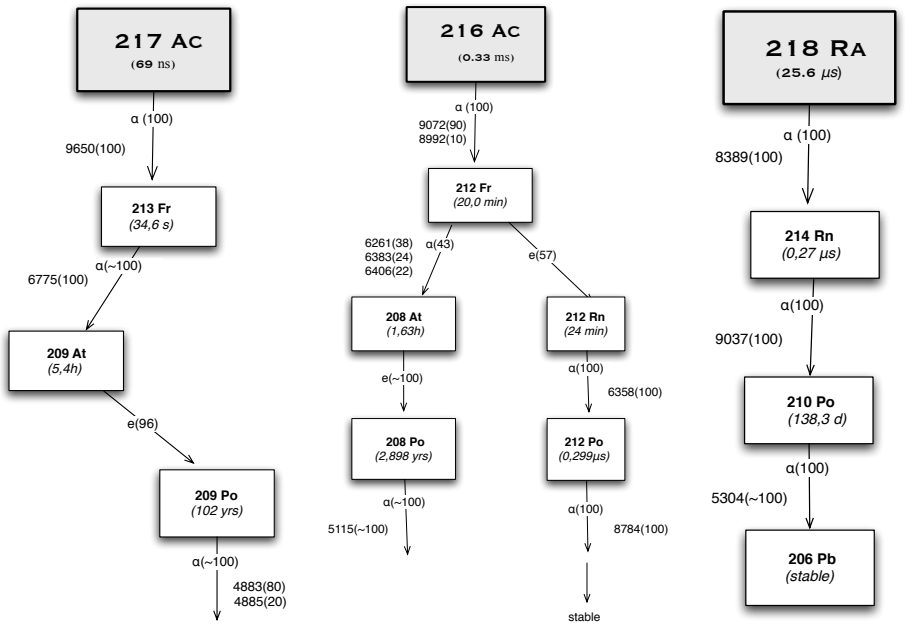

Figure 3.24: Decay chains with origin in ER likely to be produced in the calibration run by the evaporation of neutrons and proton or α.

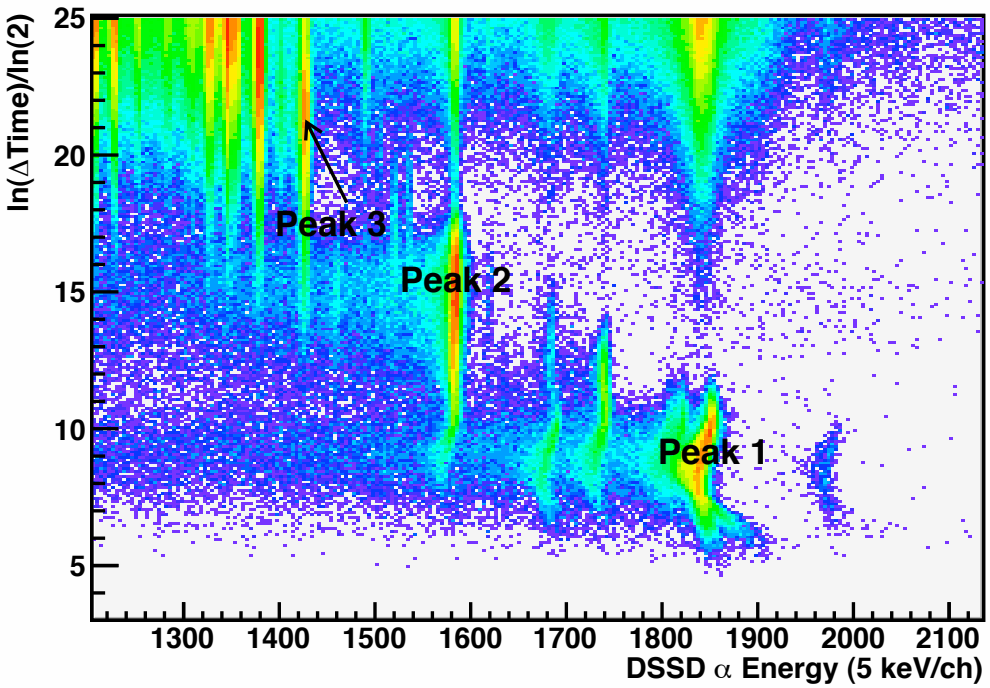

Figure 3.25: The α energy of the ERs plotted in relation to the decay time of the nuclei. Three strong decays with decay times outside the random time range are marked for first identification. The choice of scale change is explained in Appendix A. The value noted on the energy axis is an approximate value as the spectrum is uncalibrated and the dispersion was set to about 5 keV per channel.

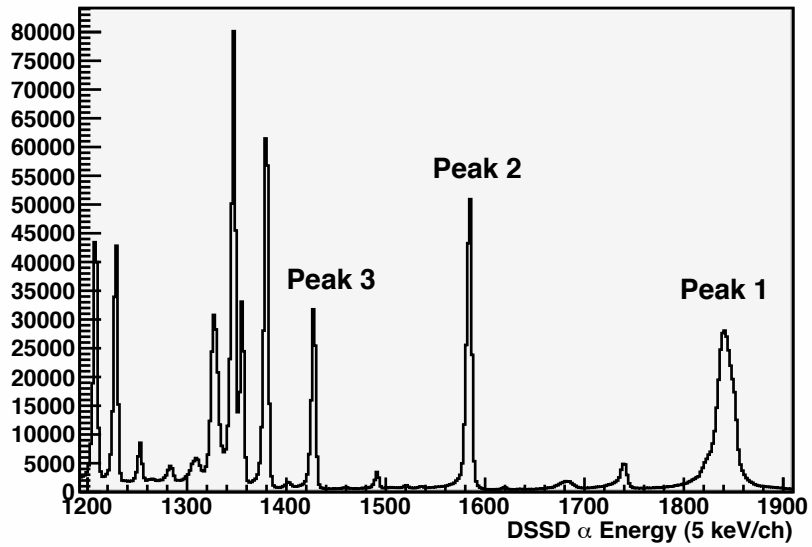

Figure 3.26: The α spectrum with the peaks 1, 2 and 3 marked (see text). The value noted on the energy axis is an approximate value.

not influenced by this effect were used. The counts affected by the artificial alteration of the energy can be removed from the spectrum by setting proper time gates.

In Figure 3.25 three peaks are marked. The peaks are shown in the energy projection in Figure 3.26. The dispersion is approximately 5 keV per channel. To be able to identify the α signal registered, the information given in the decay schemes ofe Figure 3.23 and Figure 3.24 and the decaytime information for the detected αs in Figure 3.25 must be combined.

The mean lifetime τ for the αs produced in the ^{174}Yb+^{48}Ca run can be identified in Figure 3.25. Figure 3.27 shows the time distribution of events in peak 2 of Figure 3.26. The corresponding lifetime, τ, can be determined by the relation:

$$\tau = 2^y, \tag{3.21}$$

where y is the time-value at which the time distribution peaks (see Appendix A and [14, 15]). The time-value in question for the given α decay is around 15. The fitting program used render the τ value that corresponds to a half-life of 0.02645$\pm$0.00009 s. Similar calculations are made and half-lives determined also for peak 1 and 3. Tabel 3.6 shows the α energy, half-

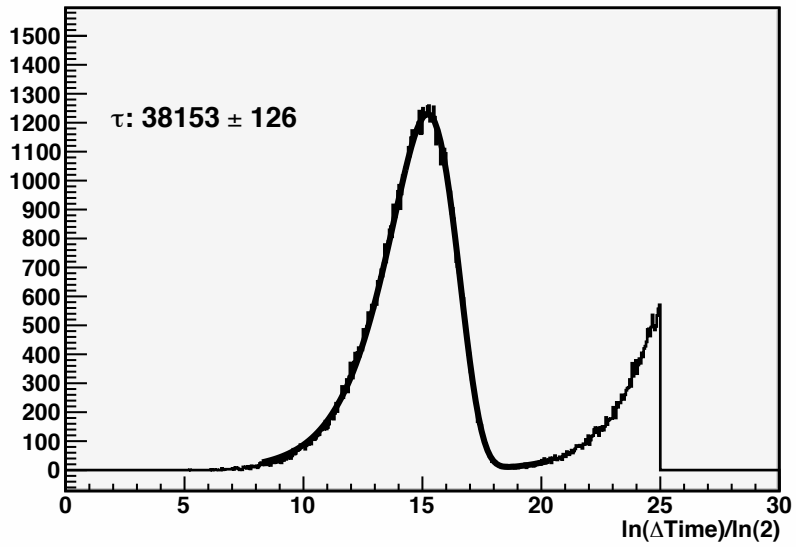

Figure 3.27: Distribution of decay times for peak 2 of Figure 3.25. The tail to the right of the peak is caused by random correlations at high times.

lives and identity of the three previously undetermined peaks. The identities where found by comparing experimental results as given in the table to theoretical values given in the decay schemes in Figure 3.23 and Figure 3.24. By comparing the half-lives of the decay and the estimated energy, the peaks can be identified. By getting a basic calibration on the basis of the above mentioned peaks, the true channel-energy relationship can be determined and further identification of the α peaks seen in Figure 3.25 is possible.

	Ch	measured E	τ	measured $T_{1/2}$	Identification
Peak 1	1862	9310 keV	548.2±0.4	0.380±0.003 ms	^{217}Th
Peak 2	1604	8020 keV	38153 ±126	0.02645 ±0.00009 s	^{216}Th
Peak 3	1451	7255 keV	3583654 ±2469	2.4844 ±0.002 s	^{214}Ra

Table 3.6: Measured values and identification for peaks marked in the calibrated Figure 3.25 and Figure 3.26. The energies used are from spectra before calibration and are thus given as approximate values and will vary somewhat from the true transition energies.

In Figure 3.28, the ERs produced are identified by their α decay. The high energy signals are caused by summation of α decays that may occur if the lifetime of the daughter is very short. This decay may then be registered at the same time as the decay of the mother thus combining the energy of the two decays. This can be the case with ^{219}Ac and the daughter ^{215}Fr, as noted in the figure.

Calibration of the γ detectors

To calibrate the γ detectors, a ^{152}Eu source was used. In Appendix F the level schemes of the decay of ^{152}Eu is given and the transitions with the highest yield identified. An identified γ calibration spectrum is given in Figure 3.29. The source used was not placed in the middle but moved around the detector matrix. A difference in peak intensities will vary with the amount of material the γ ray had to travel through before being registered in the detector. This would result in high-energy lines being stronger than low energy lines with similar yield.

Calibration of the tunnel

To calibrate the tunnel detector, the reaction ^{164}Dy(^{48}Ca,xn)$^{212-x}$Rn is used. The ^{207}Rn nucleus is known to have a 181 μs isomer, which decays by emission of conversion electrons. The decay scheme of the isomer is shown in Figure 3.30.

By looking at coincident γ-rays detected in the germanium detectors and conversion electrons detected in the tunnel as shown in Figure 3.31, one can see that the $E2$ transition with energy of 665 keV is by γ decay coincident with the 234 keV $M2$ decay by emission of conversion electrons. The two peaks from conversion electrons are from electrons emitted from the K and L shells. The binding energy of higher lying levels are not much lower than the L shell. These events are registered on the tail of the peak caused by the L conversion. The nuclear binding energy of the relevant orbitals in ^{207}Rn are given in Table 3.7. The energy of the peaks are given by equation 2.27 and are found to be:

$$T_e(K) = (234 - 98.3970)\text{keV} = 135.603\text{keV} \quad (3.22)$$
$$T_e(L1) = (234 - 18.0480)\text{keV} = 215.952\text{keV} \quad (3.23)$$

In figure 3.32, the peaks marked $T(K)$ and $T(L)$[13] are shown. To better

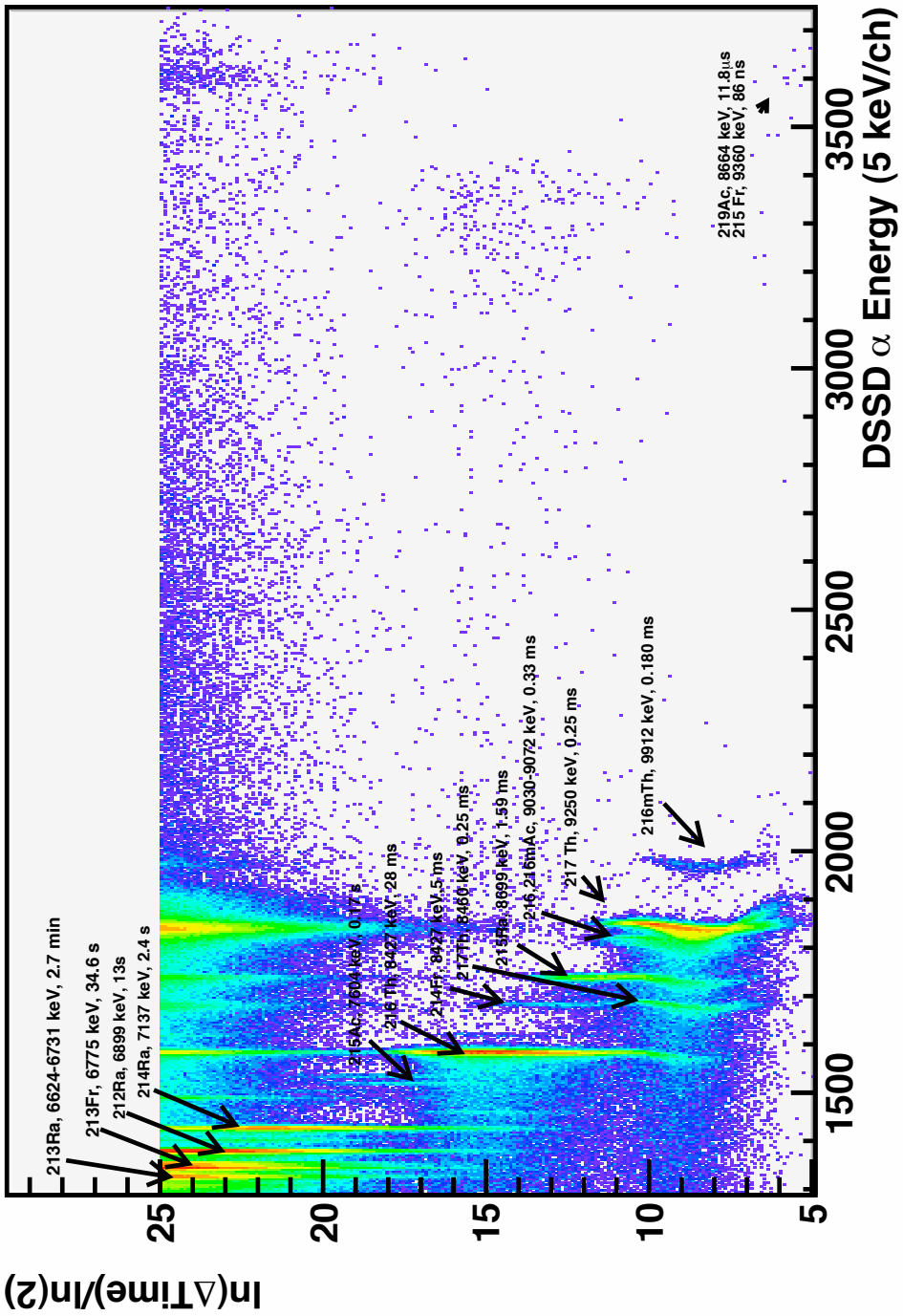

Figure 3.28: Time between recoil implantation and subsequent α decay as a function of α-decay energy observed in the reaction ^{174}Yb(^{48}Ca,xn)$^{222-x}$Th. The main channels have been identified and are marked with arrows.

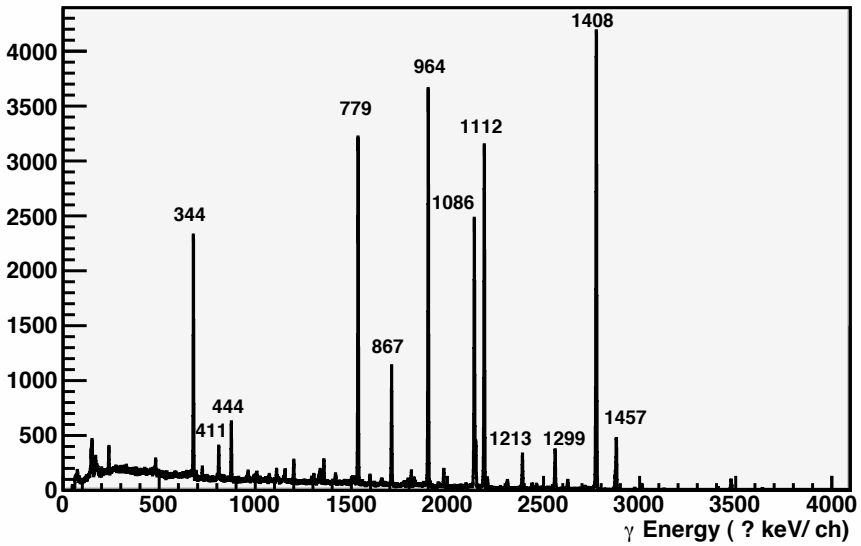

Figure 3.29: The uncalibrated γ spectrum from one of the Ge detectors with the strongest transitions in ^{152}Eu identified. As the spectrum is uncalibrated, the energy per channel relationship is unknown.

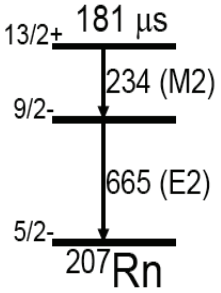

Figure 3.30: Level scheme of the isomeric decay of ^{207}Rn [16].

orbital	binding energy (keV)
K	98.3970
L	18.0480

Table 3.7: Atomic electron binding energies for Rn (Z=86).

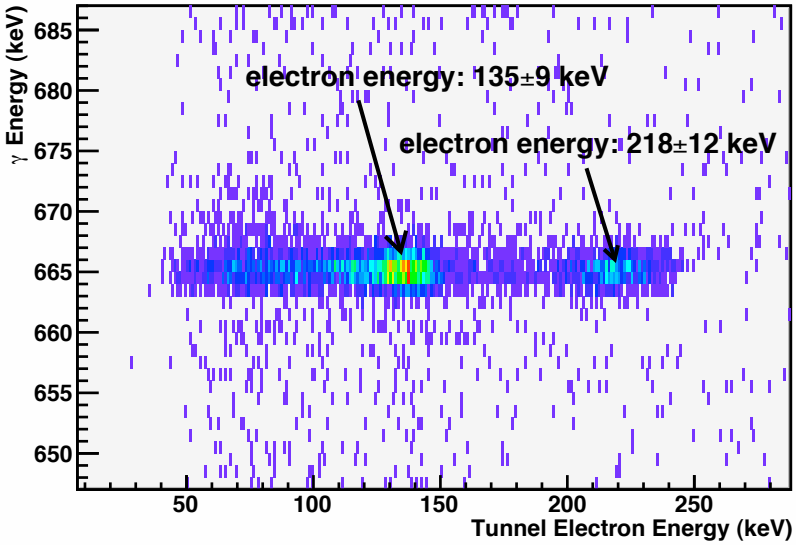

Figure 3.31: Gamma - conversion electron coincidences in the isomeric decay of ^{207}Rn. A time gate between recoil implant and decay has been set to reduce the amount of random coincidences.

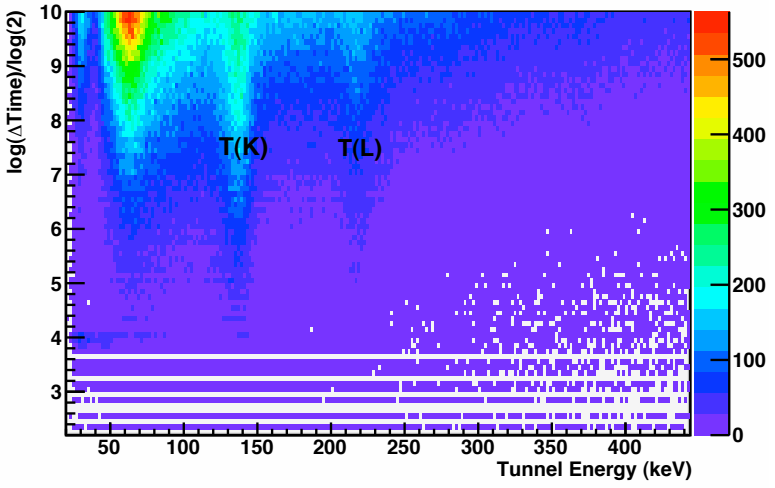

Figure 3.32: Difference in time DeltaT between the last ER detected in the DSSD and an electron detected in the tunnel detector as a function of tunnel energy.

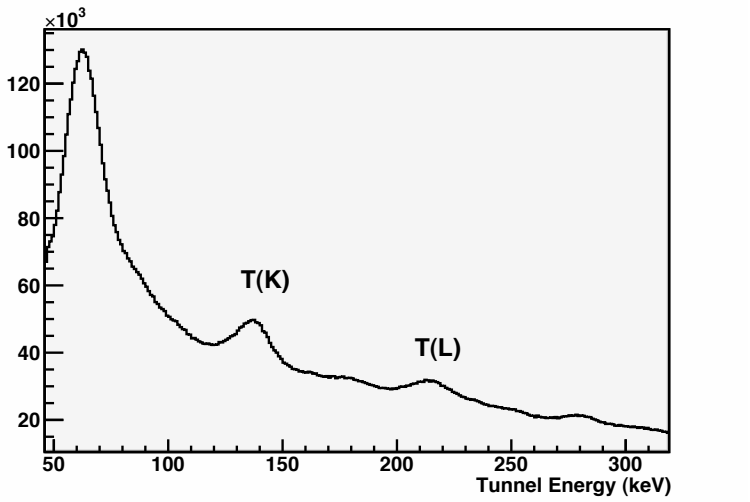

Figure 3.33: Energy spectrum of electrons detected in the tunnel without any condition on the time difference between the detection of ERs and electrons.

see the time difference, the scale used on the y-axis is $\frac{ln(\Delta Time_{electron-recoil})}{ln(2)}$. The signal looked for are blobs in the lower part of the spectrum and are marked in Figure 3.32. These are the peaks used for the gain-matching of the tunnel detector. To calibrate the tunnel detector, one looks at the decay times (time between recoil and electron detected in tunnel) as a function of electron energy. The amount of background is large. This can be seen in Figure 3.32[14] (as the strong peak coming down around 50 keV) and even clearer in Figure 3.33. The background is caused by αs escaping the DSSD and reaction products and scattered beam not sorted out by VASSILISSA. As can be seen in Figure 3.34, the background is drastically reduced by setting a maximum time difference allowed between electron and recoil signal. With the time requirement, another decay can be distinguished as seen in Figure 3.34. Though ^{207}Rn is the dominating ER channel, ^{209}Rn will also be created. This isotope decays by a converted 377-keV transition [17], giving the K-conversion signal as marked in the figure.

[13] In the calculation of kinetic energy of the electron emitted from the L-orbital, $T(L)$, the binding energy of the $L1$ shell was used. This will be the most intense conversion line as the 234 keV is an $M2$ transition. L conversion of an $M2$ character is mainly on the $L1$ shell.

[14] The empty bins in the spectrum are caused by the use of a logarithmic scale. By using a logarithmic scale, mismatch between bin numbers in the figure and channels for detection occurs at small bin numbers.

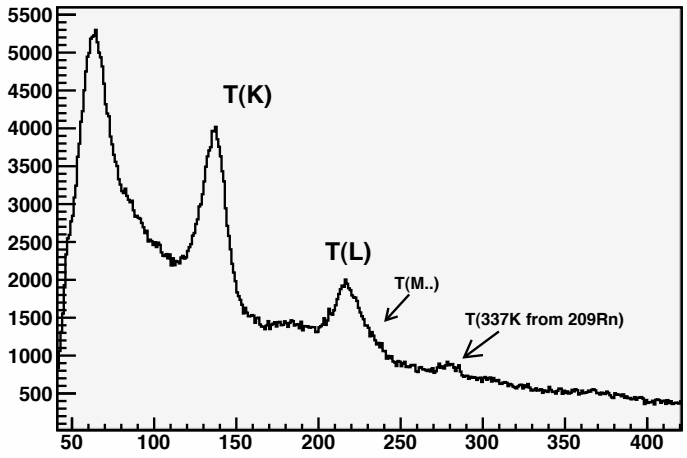

Figure 3.34: Energy spectrum of electrons detected in the tunnel with a requirement on the maximum time difference between detected ERs and electrons.

Figure 3.35 shows the γ-rays detected as a function of time elapsed since the last good recoil was detected. The γ line at 665 keV is stronger than the one at 234-keV as it is of $E2$ type and has a stronger γ-ray emission yield than the 234-keV $M2$ transition. The 511-keV γ line is quite strong and is expected as ^{207}Rn and ^{209}Rn may decay by β+ [18]. In β-decay where a positron is emitted, the positron and an electron in the detector will annihilate and create two 511-keV γ-rays, causing the strong 511-keV γ line seen in the figure.

3.6.2 Time calibration

The different amplifiers may have different shaping times or the length of the path of the signal from detection to registration may vary. This will lead to small variations in the time stamps registered of the event. To be able to set correct time gates for event-correlation, it is important to correct for time variations in the signal caused by the electronics. The time calibration of the γ detectors will be discussed here.

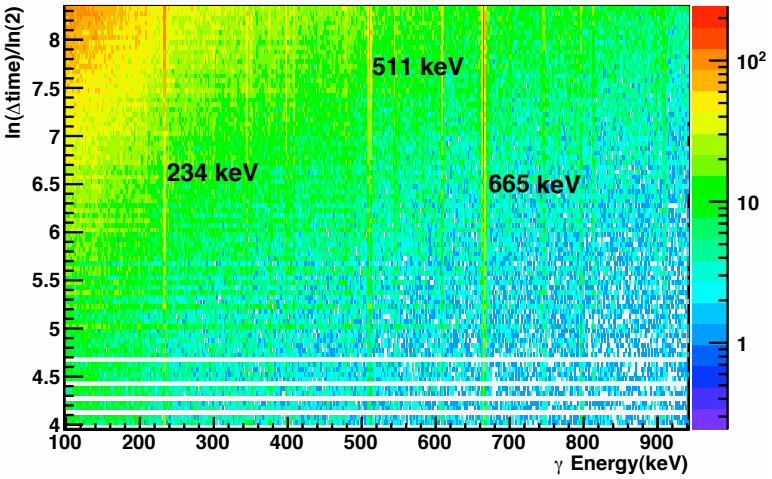

Figure 3.35: Similar plot as in Figure 3.32 for γ-rays, i.e the time difference DeltaT between the last ER detected in the DSSD and an γ detected as a function of γ energy.

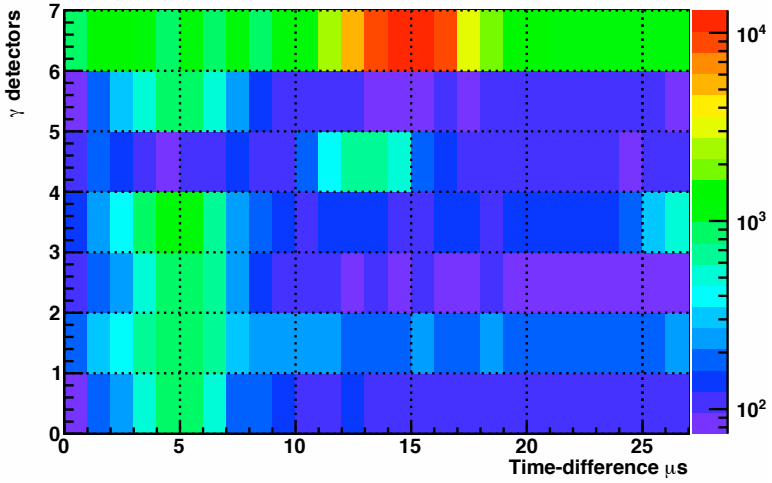

Figure 3.36: Plot of the time differences between an event in a Ge detector and an event in the DSSD. The y scale represent the Ge detector channel number.

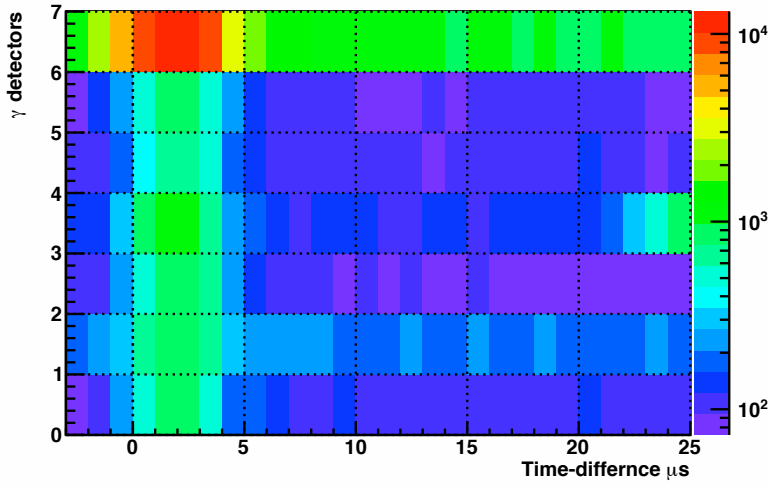

Figure 3.37: Same as in 3.36 after time alignment.

Difference in shaping times for the germanium detectors

The rise/fall time of the γ detectors varies. 'Shorty' had a lot longer shaping time to obtain a better energy resolution. This detector is placed parallell to the incoming beam and has the largest count rate as it covers a larger part of the solid angle. To be able to correlate the γ detectors in time, the variation in the time registration for the different γ detectors are corrected for. The correction of time can be estimated by looking at the plot of the time difference between γ-rays and recoil or α as seen in Figure 3.36. In the figure several of the detectors are centered around 5 μs. There are two detectors that differ from this, one peaking approximately at 15 μs and one around 13 μs. The detector in channel 7 is "Shorty". As seen, the counts of this detector is much larger than the other detectors. The second detector that has a large time variation from the other can be seen in channel 4. Figure 3.37 shows the calibrated time spectrum for the γ detectors.

Time walk

In a coaxial Ge detector, the rise time of the signal depends on the incident γ-ray energy. Figure 3.38 shows a simplified sketch of a germanium detector. When radiation is absorbed in the detector, as indicated by the stars marked 1 and 2, the energy deposited is transferred to electrons and holes in the germanium crystal. The electrons are accelerated through the crystal by an electric field, represented by lines, towards the finger shaped

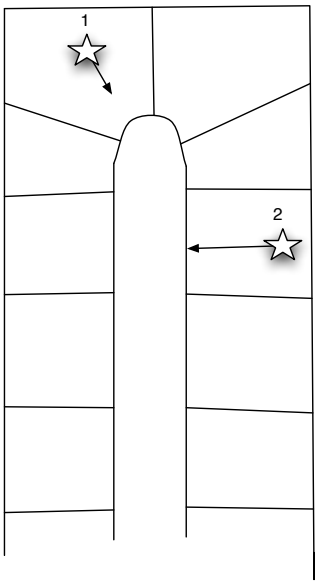

Figure 3.38: Absorption of γ-rays in a Germanium detector.

anode in the center of the detector while the holes drift towards the cathode. The uniformity and the strength of the electric field will be different for positions in the front of the detector, where interaction 1 is indicated, from the field in the coaxial part of the detector, along-side the finger. The strength of the field will affect the velocity of the charges as a weaker field will lead to a decrease in velocity. With a smaller velocity of the electrons, the charge collection time, and hence the peaking time of the amplified signal, will be delayed compared to the average charge collection time in the coaxial part of the detector. Since low-energy photons mainly interact in the front part of the detector, this time delay or time walk is observed for low-energy γ-rays.

The affect of the difference in processing time for signals for γ-rays of different energy can be seen in Figure 3.39. The figure shows the time difference between α and γ events. The strong line centered around Δt=0 at higher energies are the coincident α - γ. At low γ energies the time difference between the coincident α and γ signal is increased as the processing time of the γ-ray interaction is altered. This time walk will affect the data as coincident events of low γ energies will fall outside the coincident time gate if no corrections for this effect is made.

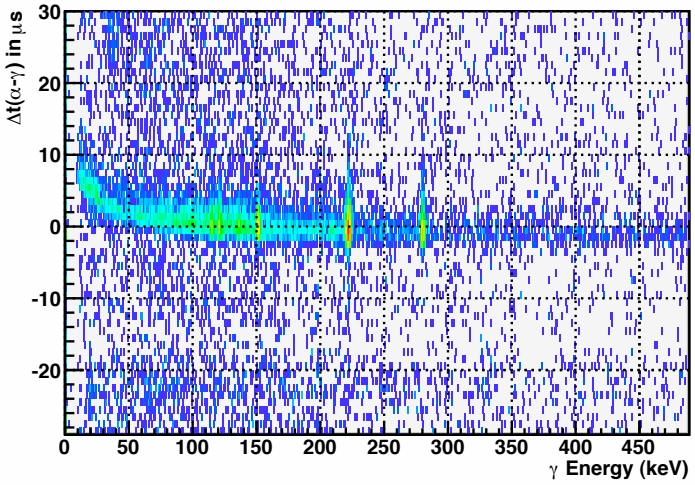

Figure 3.39: Time between the detection of an α and a γ-ray in the decay of ^{253}No. The time walk of the coincident γ-rays is visible below 150 keV.

Chapter 4

Decay spectroscopy of ^{253}No and its daughters

4.1 Properties of ^{253}No

Nobelium consists of 102 protons and a varying number of neutrons depending on the isotope. Twelve different Nobelium isotopes have been produced with determinable half-lives. The mass of the isotopes rages from 250 to 262 nucleons, with half-lives varying from 250 μs to 58 min. The discovery of Nobelium was first claimed by an international group working at the Nobel Institute of Physics in Stockholm. The results from the Stockholm group however, were not in accordance with results obtained at Berkeley, USA, in 1958. The Berkeley results where reproduced in Dubna, Russia, in 1965 confirming the discovery. The name however, set by the Stockholm group was kept.

In 1967, ^{253}No was determined to be an α emitter with an α energy of 8.01 MeV and having a half-life of about 105 seconds, [23]. This isotope decays to ^{249}Fm. In the daughter, γ-rays and conversion electrons have been observed. Hessberger *et al.* [19] reported 279-, 220-[1] and 150 keV $E1$ transitions from an excited level in ^{249}Fm. Further study of this isotope was presented in the paper by A. Lopez-Martens *et al.* [3]. Here, two new excited states were argued to be the first members of the ground state rotational band, and were found to have the energy of 129 and 58 keV. Another single-particle state of spin-parity 5/2+ and energy 211 keV was believed to be seen, although not seen as a γ-ray. Conversion coefficients for the 279-, 221-, 150- and 129 keV transitions were also measured. By compari-

[1] The energy of this transition is in other experiments found to be 221 keV

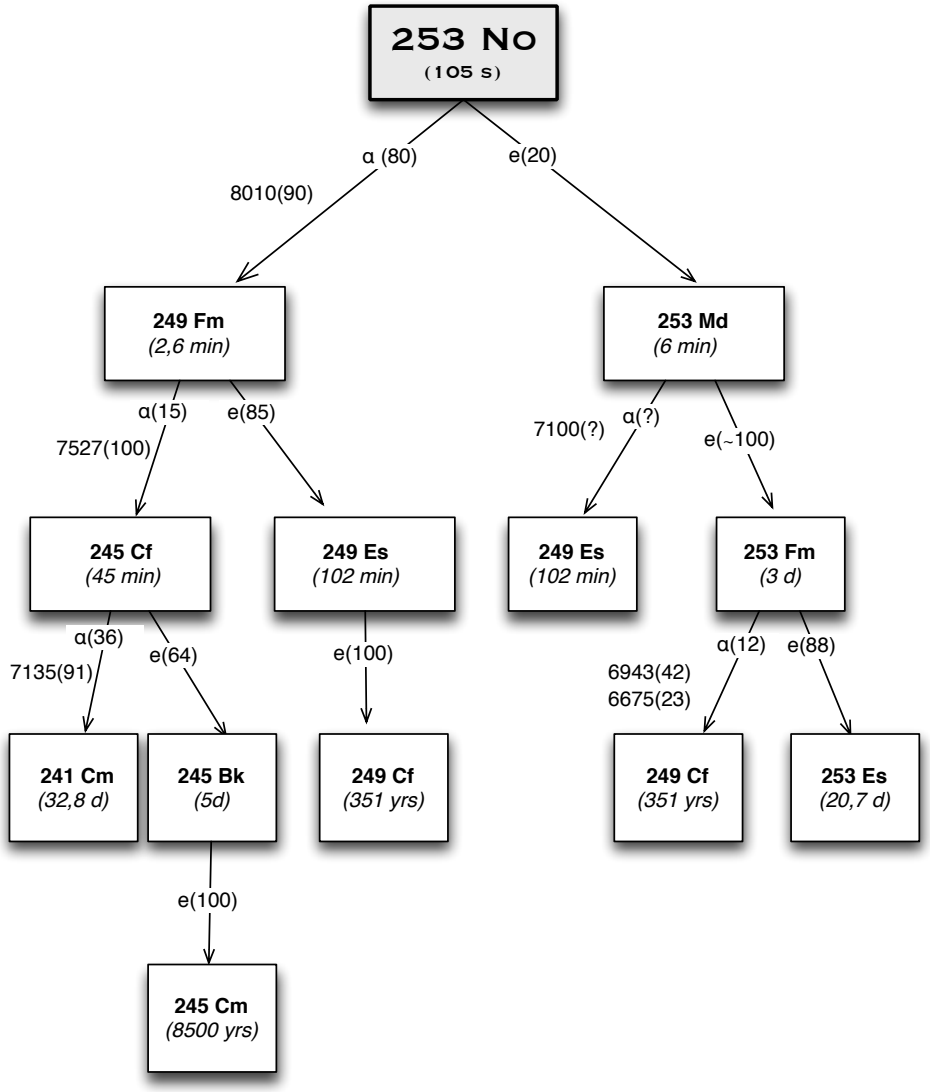

Figure 4.1: Decay chain starting with ^{253}No. The time given in parenthesis under the isotope identification gives the half life of the nucleus while numbers given outside the boxes represent the dominating α energy of the α decays. The decay types are labeled with α for α decay, e for β decay and sf for spontaneous fission. The number in parenthesis outside the boxes gives the yield of the decay.

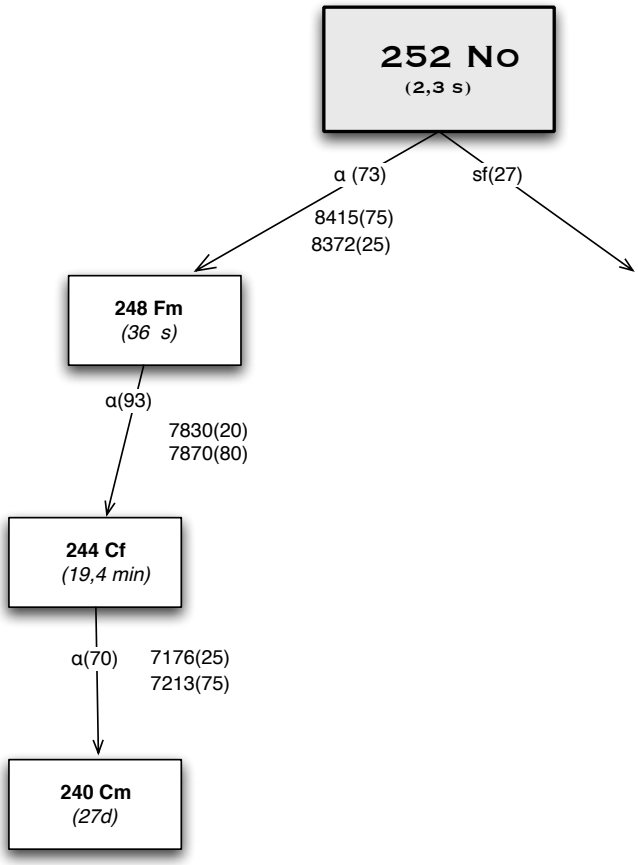

Figure 4.2: Decay chain starting with ^{252}No.

son of experimentally determined conversion coefficients with theory, the character of the 221 keV and 150 keV decays were confirmed to be of type $E1$. The 279 keV conversion was also argued to be $E1$, although with an unusually large conversion coefficient. The 129 keV transition was found to be of $M1$ or $E2$ character. The 211 keV transition was thought to be $M1$, pure or mixed with $E2$ or a pure $E2$ on the basis of the experimental $LMN+$ conversion coefficient. However, by looking at the X-ray excess problem, which will be discussed in section 4.2.3, the conclusion made by Lopez-Martens *et al.* [3] was that the transition could be pure $M1$.

The motivation for the experiment of this thesis was, by part, to confirm these previously obtained results.

In the ^{48}Ca + ^{207}Pb reaction the isotopes produced are ^{252}No and ^{253}No (^{254}No), though mainly ^{253}No, as discussed in section 3.2.2. With the basis of the nuclear chart and other databases [20], decay chains as shown in Figure 4.1 and Figure 4.2 can be determined. As noted in Figure 4.1, ^{253}No will decay 80%[2] via α decay to ^{249}Fm. ^{249}Fm will again decay either through α decay or by electron capture. The products of these reactions are again unstable. Numbers noted alongside the arrows are the listed α energies of the decay. By finding the relative intensity of an α signal compared to another α in the chain, the observed α-lines can be identified.

4.2 Analysis

4.2.1 Products from run

The selection of recoils and determination of half-life

A problem in complete-fusion reactions is that the ratio of good recoil to background is very low. To be able to distinguish the ERs from the background, it is essential to first of all have a good separator that will reduce the background dramatically. Secondly, it is necessary to select good recoils on an event by event basis, as previously discussed. Figure 4.3 shows the recoil energy-TOF plot with the following requirement set: If an α particle is detected with an energy that corresponds to the decay of ^{252}No

[2]This number is the tabulated value taken from [7], although the EC branch of ^{253}No has been found to be $\sim$30% [21], a conclusion supported by other findings [3].

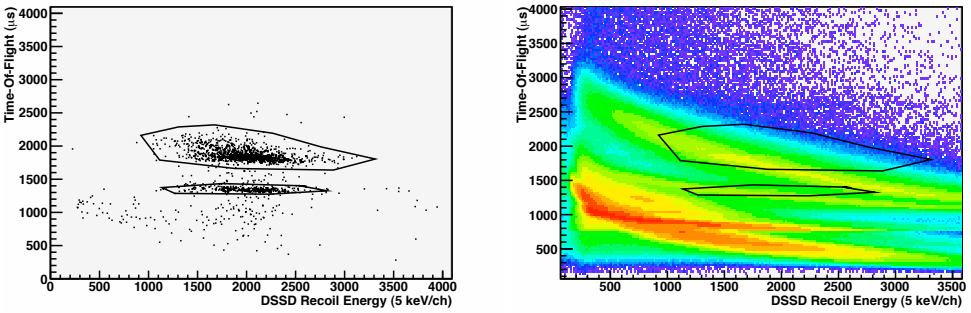

Figure 4.3: TOF vs recoil energy plots. The figure to the left is obtained by gating on ^{252}No recoils (see text for details) and allows to determine the TOF-recoil energy contours for ERs. The figure to the right shows the same plot for all the recoils detected during the run. The ER contours are shown in both plots.

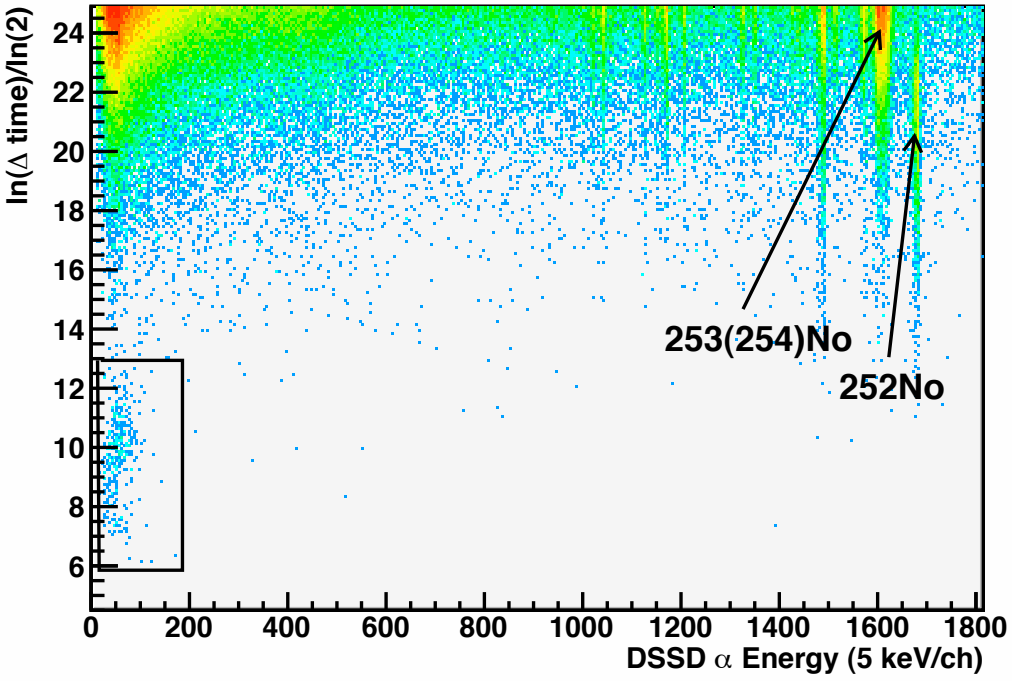

Figure 4.4: Energy and decay time of recoils registered within the cut of good recoils drawn in Figure 4.3.

with a decay time outside the random time range (i.e ln(Δ time)/ln(2)<22 in Figure 4.4), the energy of the last recoil registered in the same pixel as the α is plotted with relation to its time of flight. By doing this selection it is, as seen in the left spectrum in Figure 4.3, possible to distinguish the energy-TOF relationship of the α signal from the wanted Nobelium isotopes from other reaction products. A cut is made around the area where the energy-TOF relationship is that of the ERs. In Figure 4.3, two cuts are marked. This is caused by a change of amplification of the TOF-value during the run. Different cuts are used for different files during the sorting. The reaction products in the whole banana-shaped area in the figure to the right are transfer products, i.e target particles that have interacted with the beam, while the large area of high intensity at the lower left of the spectrum is caused by scattered beam. Scattered beam represent the majority of events detected in the DSSD. The positioning of the areas of the good recoils are again marked in the right plot in Figure 4.3. The selection of recoils with respect to the energy-TOF relationship is important for lifetime determinations and the determination of isomeric decay.

The data in the lower left corner in Figure 4.4 within the rectangle is caused by conversion electrons, Auger electrons and/or x-rays depositing energy in the DSSD. The signal in question has its origin in the decay of isomeric states in the recoil.

A problem with α-recoil correlations that arises with the Nobelium data, is the ”long” half-life giving a relatively large probability of a new implanted recoil in the pixel before the previous one has decayed. This will lead to an α being correlated to a recoil which was not the one undergoing the decay. The random recoil-α rate can be seen as the green continuous line at the top of the spectrum in Figure 4.4. The random coincidences becomes significant already after a mean lifetime of 10 seconds (ln(Δtime) / ln(2)=23.3) and increases with higher time intervals. The plot is cut off around 50 s, (ln(Δtime) / ln(2)=25), as the correlations at this point are of random nature. The lifetime of ^{253}No is about 100 s, or 1.7 min, making lifetime determination of this isotope impossible in this experiment. However, ^{252}No is also created in this experiment but with a smaller cross section. This isotope will decay either by spontaneous fission or α decay. The α energies, of 8.42 and 8.37 MeV, are located around channels 1674 and 1684 in Figure 4.4 with a higher yield for the 8.42 MeV transition. The lifetime of ^{252}No found in the literature is 2.3 s [22]. With this short lifetime it is possible to estimate the approximate lifetime experimentally. The mean lifetime of ^{252}No is found by projecting onto the y-axis of Figure 4.4

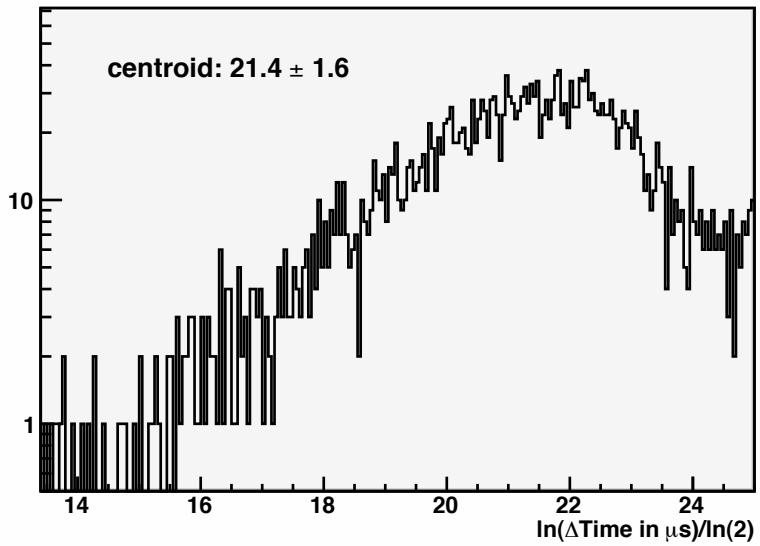

Figure 4.5: Distribution of the decay times of ^{252}No.

the slice corresponding to ^{252}No α particle energies. The result is shown in Figure 4.5.

The half-life is related to τ as given in equation (2.13). The mean lifetime τ for ^{252}No is 2 $^{21.4\pm1.6}$ as the scale on the y-axis is:

$$\frac{ln(\Delta time_{(recoil-alpha)})}{ln(2)} \tag{4.1}$$

in μs. The choice of scale and its relation to the mean time is explained in Appendix A. The experimentally determined half-life is 2.3$\pm$0.17 s, which is in perfect agreement with the literature value.

Identification of the α spectrum

The identification of some of the αs observed in the run are displayed in Figure 4.6. The background level is rather large, and is, by part, caused by recoils mislabeled as α particles as indicated by the red line. The αs identified are the main ones from the decay of ^{253}No and ^{252}No. Also ^{254}No is produced, see Appendix A, but its energy is such that it overlaps with the signal from ^{253}No. ^{254}No decay with α decay of energy 8.1 MeV, which is within the energy range of the ^{253}No α group. It is not possible

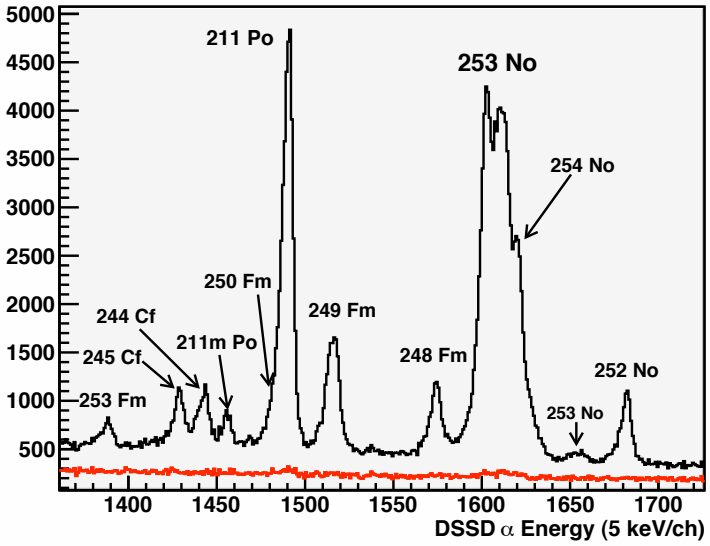

Figure 4.6: The α spectrum obtained by the ^{207}Pb(^{48}Ca,2-3n)$^{252-253}$No reaction. The red line indicates the background level caused by recoils mislabeled as α particles

to distinguish the two isotopes as their half-lives do not drastically differ (55 s for ^{254}No [23]). However, the presence of ^{254}No does not affect the analysis of the ^{253}No decay as the ground state of ^{254}No has been observed to mainly decay to the ground state of ^{250}Fm with no coincident emission of γ-rays or conversion electrons. Some of the αs are created by the decay of other isotopes produced in this run or long-lived remains from previous runs.

4.2.2 Decay of excited states and correlations of decay modes

After the decay of the ER, the daughter is likely to be in an excited state and may decay by prompt emission of γ-rays and/or conversion electrons. To be able to say something about the decay scheme of the nucleus, it is essential to find correlated γ-rays, electrons and electron-γ events. Coincident de-excitation events represent steps in the same de-excitation chain (cascade).

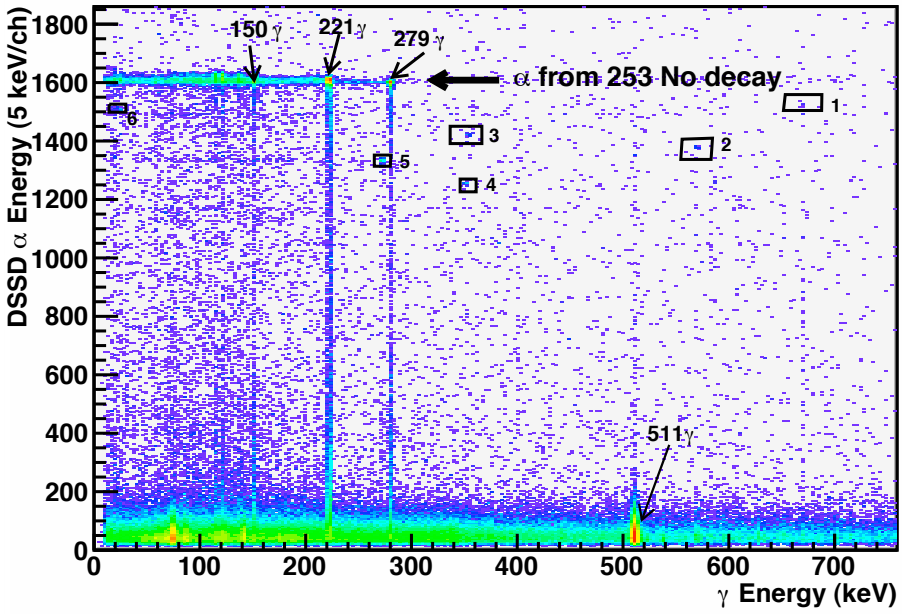

Figure 4.7: Prompt α-γ coincidence matrix.

The α-γ and α-electron correlation spectra

Figure 4.7 shows the γ events registered correlated to their respective α particle. The horizontal line around channel 1600 on the y-axis are α signals from the decay of ^{253}No. For the strong γ signals at, among others, channel 221- and 279 keV, there are stripes going down from the true α value to the bottom of the spectrum. The recoil is implanted in the DSSD at a given depth. As the implantation depth is shallow, it is possible for the α to escape the detector if emitted in a certain direction. The stripes are partly caused by α-particles escaping the DSSD with a varying fraction of its energy. Another effect causing the stripes is the energy sharing between several detector strips or charge loss due to characteristics of the detector.

The boxes marked in Figure 4.7 with numbers 1-6 are weaker observed α-γ correlations that will be discussed in section 4.2.4. Also, the strong γ line of energy 511 keV is marked indicating the presence of β decay in the chains of the produced recoils. The electron energy loss in the focal plane detector will be registered as an α. The very low α energies in the bottom of spectrum in Figure 4.7 can be caused by escaping αs or signals from electrons.

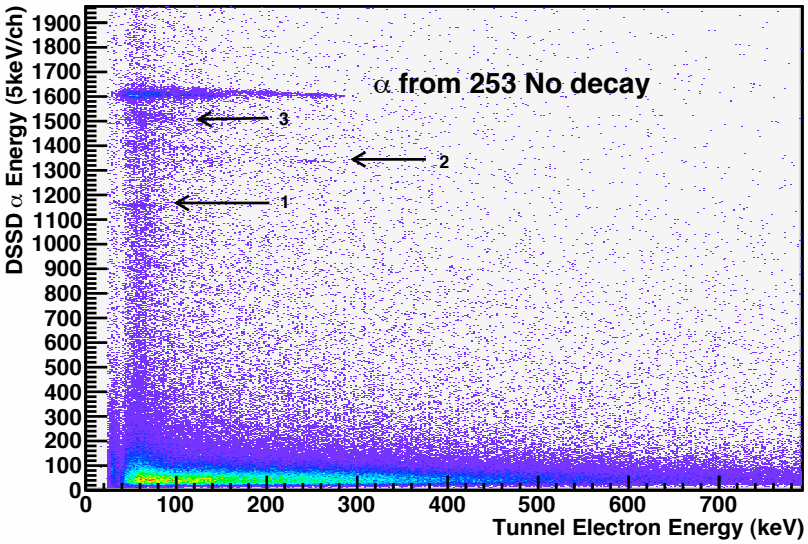

Figure 4.8: Prompt α-electron coincident matrix with background given in Figure 4.10 subtracted. The arrows indicate possible decays.

A transition between two excited states, or an excited state and the ground state, goes by the emission of a γ-ray or a conversion electron. The spectrum in Figure 4.8 shows electrons detected in the tunnel that are found to be in coincidence with an α. The electrons in coincidence with ^{253}No α decays are marked. The arrows 1, 2 and 3 indicate other possible α-electron coincidences. The number of random correlation is relatively high, resulting in an unclean spectrum where true coincidences can be difficult to separate from the background.

To get an accurate estimate of the number of events in a peak, background has to be subtracted from the total peak number. There are several types of background it is essential to be aware of. Firstly, for both the γ and the electron spectrum, there will be background caused by recoils being mislabeled as αs. Additional gating can be done in the software thus reducing this type of background. Figure 4.9 and Figure 4.10 show the α-γ and α-electron coincidence spectra for recoils being mislabeled as αs and being in (random) coincidence with a γ or an electron. The events in these background spectra are subtracted from the corresponding cuts in the total α-electron and α-γ coincidence spectra. In Figure 4.8 the back-

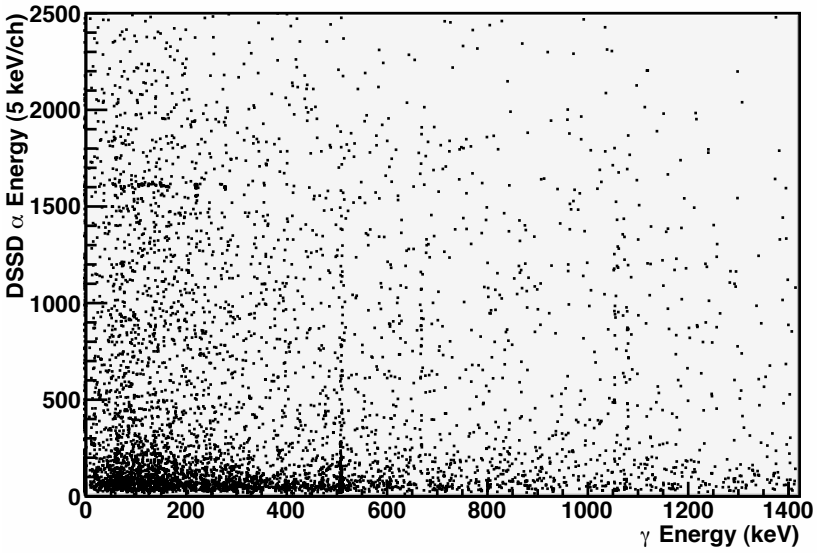

Figure 4.9: Background in the α-γ matrix caused by recoils mislabeled as αs.

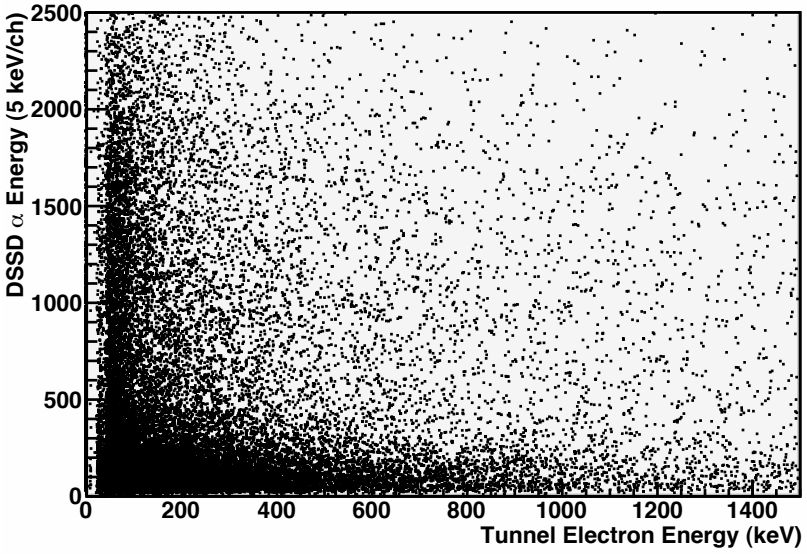

Figure 4.10: Background in the α-electron coincidence spectrum caused by mislabeled recoils.

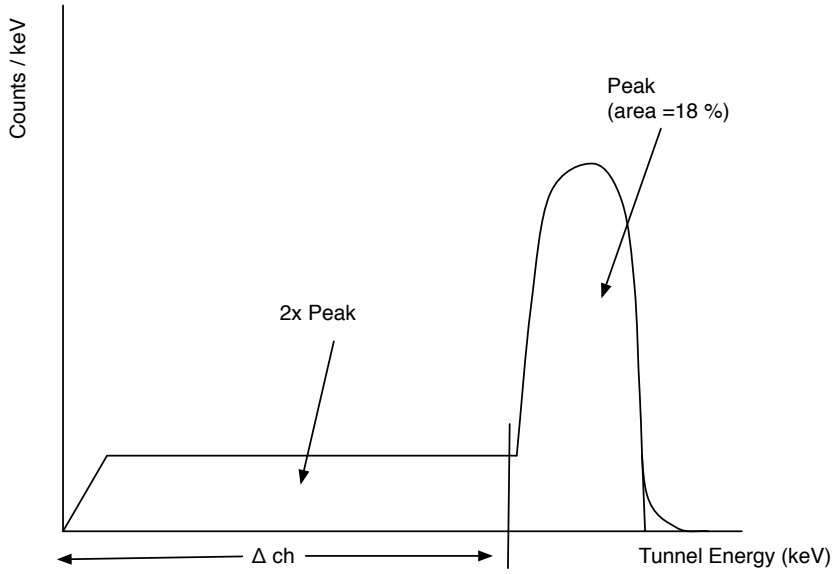

Figure 4.11: Sketch of the tunnels response function. 18 % of the electrons are registered in the peak (the efficiency). The background is approximately constant and contains twice the number of counts present in the peak.

ground spectrum given in Figure 4.10 has been subtracted from the total α-electron coincidence spectrum to make the decay signals clearer. In addition to the general background from mislabeled αs, the peaks lie on top of a background resulting from the summing of all the constant backgrounds stemming from higher lying peaks. For the γ events, background caused by Compton-scattering from higher energy lines are present. For electrons there will also be a variation of the fraction of energy detected. A sketch of the response function of the tunnel detector is given in Figure 4.11. Two times the counts in the peak is approximately linearly distributed over the channels to the left of the peak:

$$background/ch = \frac{2 \cdot peak}{\Delta ch} \tag{4.2}$$

In Figure 4.11, the background is shown going to 0 at low energies due to the threshold of the detector.

Electrons originating in the DSSD will deposit energy in the DSSD. As the electron and α in the situation discussed here are in coincidence and originating at the same position in the DSSD, summing between electrons

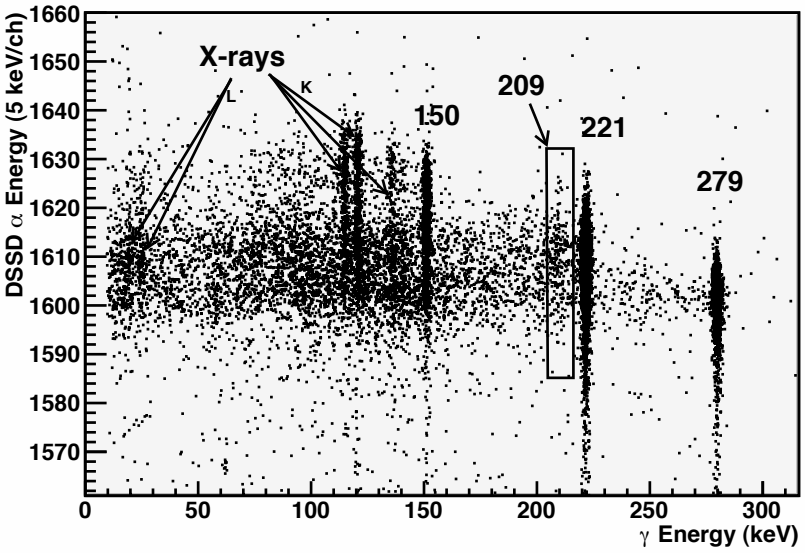

Figure 4.12: The γ-rays in coincidence with ^{253}No α decays.

and α will occur. As may be seen in the Figure 4.16, the clusters representing the α-electron relationship are tilted downward from left to right, as the electron deposit a varying amount of its energy in the DSSD. The DSSD energy is increased by as much as the electron signal is reduced. The amount of energy deposited in the DSSD by the electron depends, like for the α, on the emission angle and the velocity of the particle.

Figure 4.12 shows the γ-rays detected in coincidence with ^{253}No and is an enlarged section of Figure 4.7. There are three strong γ peaks with energy 279, 221 and 150 keV as well as a weaker 209 keV transition marked. The lines around 100-140 and 15-25 keV are caused by characteristic x-rays. The 279 keV transition has a lower position in the spectrum with respect to those of the 221- and 150-keV transitions. If projecting out the energy spectrum for the αs in coincidence with the 221 keV and 279 keV γ-rays, the spectra shown in Figure 4.13 are obtained.

The DSSD had a resolution of $\sigma\sim$2.5 channels. The resolution of the α in coincidence with the 279 keV γ is $\sim$2.8 channels, indicating that there is no converted transition in coincidence with the 279 keV line[3]. By comparing the energy of the α particles in coincidence with γ-rays with the

[3]Remark: If the converted transition is of low energy (<40 keV), the shape of the α peak would not be changed much but shifted to higher energies.

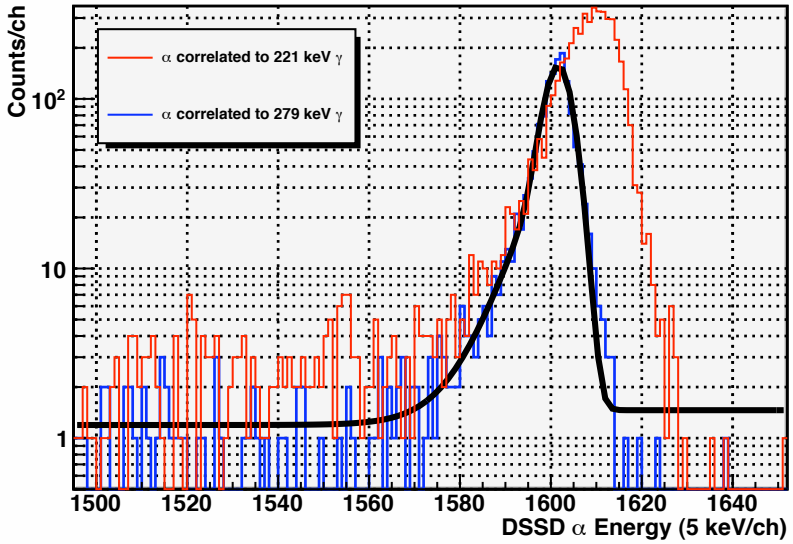

Figure 4.13: The α spectrum for αs from ^{253}No decays in coincidence with 279 keV γ-rays, marked in blue and fitted, and 221 keV γ, marked in red. The centroid of the 279 keV correlated peak is 1601.2$\pm$0.2 and σ=2.8$\pm$0.1 channels while the 221 keV peak has a centroid of 1614$\pm$3 and $\sigma = 3.6\pm0.3$ channels.

highest energy observed in the total α spectrum of ^{253}No the transition can be identified as going to the ground state[4]. The α-energy feeding the 279 keV state is 8006$\pm$1 keV. In comparison, the resolution of the α spectrum coincident to the 221 keV γ, marked in red in the figure, is wider and the centroid is shifted to higher energy, resulting in a peak centered around channel 1614 with a resolution of $\sigma\sim$3.6

In Figure 4.12, several x-ray lines are marked. When an atom is left in an excited state due to vacancies in inner atomic orbits, for instance following decay by internal conversion, it will decay to the ground state by the emission of x-rays, Auger electrons or the combination of the two. Auger electrons have low energy and will deposit most, if not all, of their energy in the same pixel as the α particle in the focal detector. The x-rays with energy above 100 keV are K x-rays, while the two lines marked far to the left of the spectrum are x-rays following the emission of L-shell electrons.

[4]The peak of the 279 keV decay is of the same energy as the first maxima in the total α spectrum for the ^{253}No decay, as discussed in Appendix C.

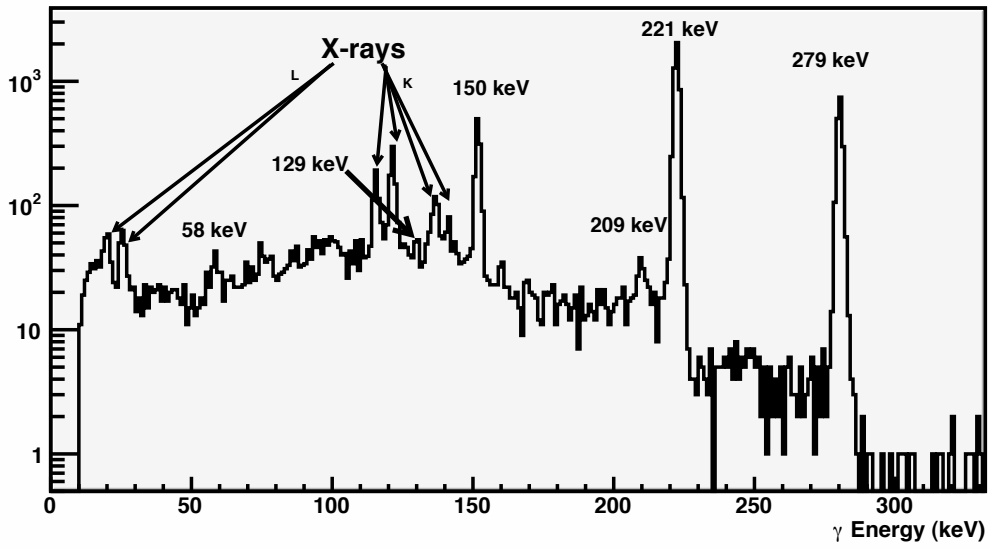

Figure 4.14: Spectrum of γ-rays in coincidence with the α decay of ^{253}No.

Correlation of α-events to prompt following radiation

Figure 4.14 shows the projection of Figure 4.12 onto the γ-ray axis with a condition on the α energy.

In this figure a 209 keV γ peak is detected, a transition not previously directly seen [3]. From conversion electron data the presence of a transition, of energy estimated to be of 211 keV, was predicted since the ratio between the amount of K-electrons and x-rays did not correspond without this assumption. More statistics were obtained during this run rendering the peak in the α-γ coincidence spectrum observable thus making it possible to determine a more accurate transition energy. In addition to the 209 keV signal, weak γ lines are seen with energy 58- and 129-keV.

The α-electron correlated events from ^{253}No α decay are given in Figure 4.15. The binding energies of the first orbitals in Fermium are given in Table 4.1[5]. The binding energy of $N+$ orbitals are such that they will, with

[5]There are several sub-orbitals for the L and M orbitals. The values given in the table are the average binding energies of the orbitals in question. The variation of the binding energy for the different sub-orbitals may vary with several keV, but with the tunnel resolution being as poor as it is, there is no need to take this into further consideration

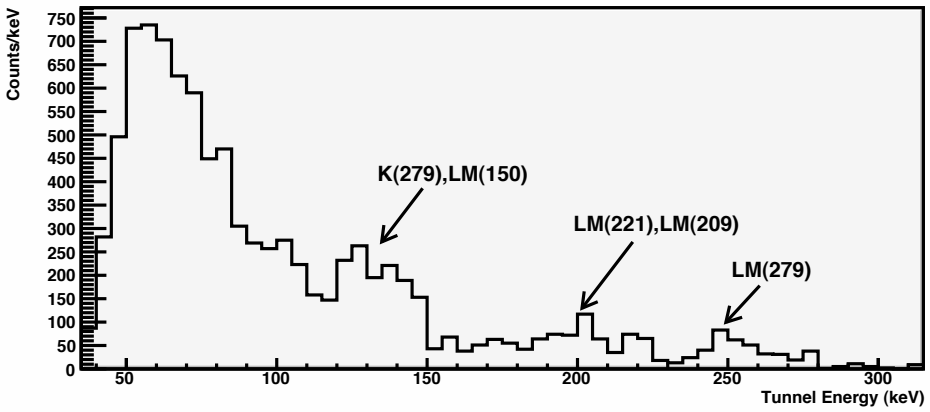

Figure 4.15: Spectrum of conversion electrons in coincidence with the α decay of ^{253}No with no background subtracted.

Orbital	Binding energy (keV)
K	142
$\bar{L}$	24
$\bar{M}$	6

Table 4.1: Binding energy of K, the average energy of L and M orbitals in Fermium [24].

the resolution of this experiment, be included in the M-conversion electron cuts made. Thus, when discussing experimental results, M or LM conversion are in reality $MN+$ and $LMN+$ though just noted as M or LM.

The position of the expected electron signals is given by equation 2.27.

Several structures are visible in the spectrum in Figure 4.15 showing the energy of the conversion electron spectrum with no background subtracted.In Table 4.2 are the kinetic energies of the conversion electrons given. The conversion electrons from the 279 keV L and M orbitals transitions should be found around 250-270 keV, thus likely to be the origin of the structure visible around energy 250 keV. The K conversion electrons of the 279 keV transition have an energy of 137 keV which structure can be seen at energies 120-150. In this area however, LM conversion from

here.

Orbital / *Energy*	279 keV	221 keV	209 keV	150 keV
K	137 keV	79 keV	67 keV	8 keV
L	251 keV	193 keV	181 keV	122 keV
M	272 keV	214 keV	202 keV	143 keV

Table 4.2: Expected energy of conversion electrons

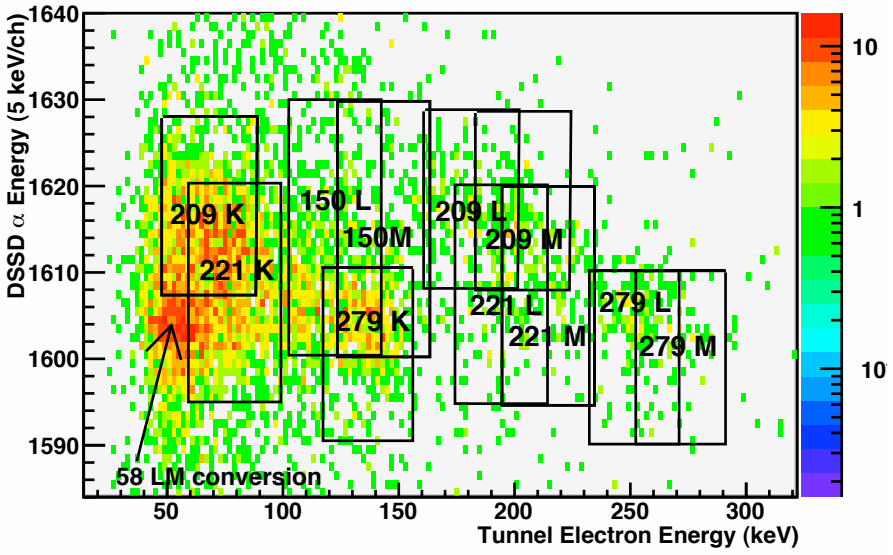

Figure 4.16: Electrons detected in coincidence with α of energy corresponding to the decay of ^{253}No with areas marked for the location of the electrons signals for the *K* and *LM* conversion for the 279- 221- 209- and 150-keV transitions.

the 150 keV transition is also located as these have an energy of ∼120-150. The 221 transition gives rise to 79 keV *K*-conversion electrons. The structure for this conversion can not be identified in this figure, but the *LM* transition can be seen around energy 200 keV. This area is overlapping with the *LM* conversion of the 209 keV transition, whose *K* transition, like for the 221 keV, can not be isolated in Figure 4.15. Figure 4.16 shows the α-conversion electron coincidence matrix with boxes to mark areas where most of the electron counts of a given energy are found. The α energies selected, are determined, except for the 209 keV transition, by looking at the positioning of the corresponding α-γ signals in Figure 4.12. For the 209 keV transition, structures can be seen in the spectrum in Figure 4.16 at the expected electron energy at a α energy of about 8075 keV (channel 1615).

In addition to the overlap of the signals marked in Figure 4.16, other highly converted states are present in the α decay of the Nobelium isotope. The 58 keV conversion is marked. In addition to this, conversion electrons from 71- and 129-keV transitions are present in the cuts made for the conversion electrons of energy lower than around 130 keV, as will be discussed later.

Finding the energy of the α in correlation with the 209 keV transition is somewhat difficult. There is no clear signal in the α-γ coincident spectrum as the signal is more or less drowned in the Compton background from the strong 221 and 279 transitions. Using the α-γ matrix to project out the α energy coincident to the 209 transition results in a wide peak, seen in Figure 4.17 marked in red, with a mean value in channel 1610.8$\pm$0.8 channels. As seen in Figure 4.16, the α energy is expected to be found around channel 1615. The width of the peak indicating a mixing of α energies. A better approximation of the α energy might be obtained by looking at the α-electron correlated events. Though the overlap between the transitions is a problem, the 209 transition is quite strong and will hopefully be dominating at some electron energy cuts. A projection made for α energies in correlation with electron energies between 161 -195 keV is shown by the blue structure in Figure 4.17. In the figure a large peak around channel 1617 can be seen, as well as a smaller structure around channel 1605. The 1605 structure is caused by background from the 279 *LM* transitions. As can be seen in the figure, the α energy obtained is as expected: 8085$\pm$3 keV. The width of the peak is such that summation of α energy due to conversion electrons in coincidence with the transition is highly unlikely, thus indicating the existence of a state of energy 209 being fed by an α of energy 8085$\pm$3 keV.

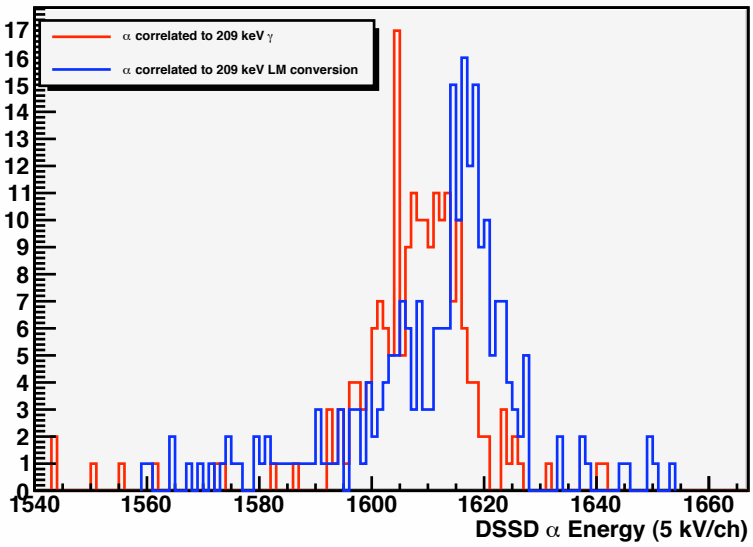

Figure 4.17: Alpha energy of the 209 keV transition, in coincidence with 206-213 keV γ-rays, marked in red, and electrons of 161 - 195 keV, marked in blue and fitted. The centroid of the γ correlated transition is 1610.8$\pm$0.8 and σ=5.2$\pm$0.8, while it is 1616.9$\pm$0.6 and σ=3.1$\pm$0.8 for the electron correlated projection.

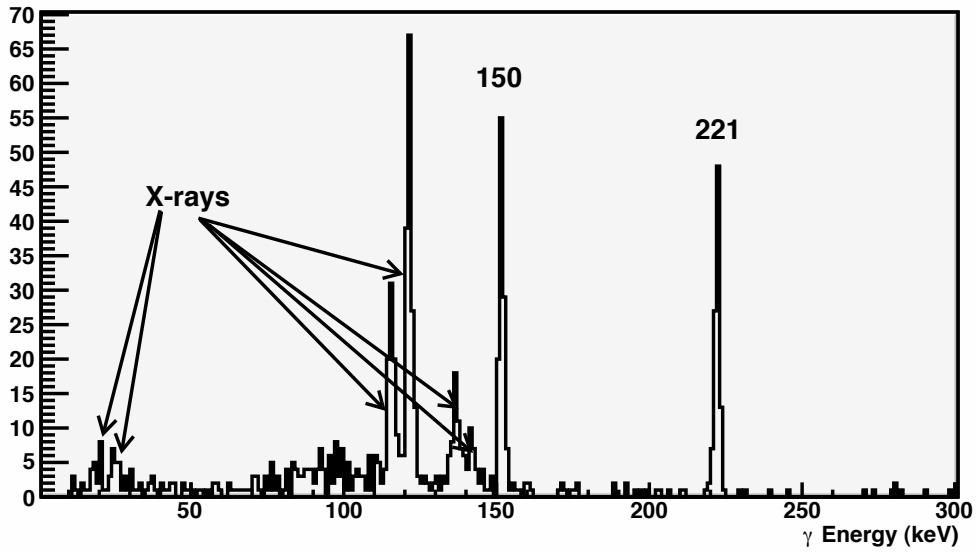

Figure 4.18: Electron-γ coincidences following the α decay of ^{253}No

To determine if the 209 keV transition is in coincidence with a 8085$\pm$3 keV α, using equation (2.18), the Q value for the transitions from the 279 keV band in coincidence with the 8006$\pm$1 keV is found and compared to that calculated on the basis of the 209 keV decay, assuming ^{253}No is the origin of both. The Q-value of the decay to the 279 keV excited state in the ^{249}Fm isotope is 8414$\pm$2 keV, while the value obtained for the 209 keV transition with corresponding α was 8423$\pm$4 keV. The results supports the assumption of the 209 keV state being an excited state in ^{249}Fm.

Determination of cascades

If the γ in coincidence with the α also is required to be in coincidence with electrons, one obtains Figure 4.18. Electron coincidences are observed for the 150- and 221 keV γss but not for the 279 keV γ-ray. For the 209 transition, there are two counts within the coincidence area. These counts may very well be caused by random correlations or Compton scattering from the 221 keV transition. For the 279- and 209 keV transitions, no coincident events are expected as the excited levels are assumed directly fed by their respective α decay before decaying directly to the ground state[6].

[6]This is a truth with modifications. From systematics (level schemes are given in section 4.3.1) both the 279- and 209 keV transitions are expected to have some feeding from

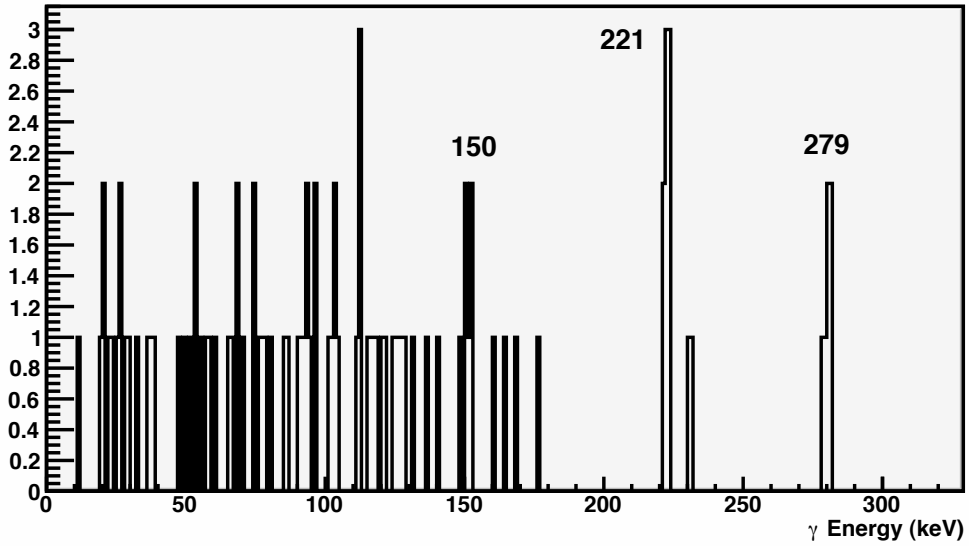

Figure 4.19: The γ-γ coincidences following the α decay of ^{253}No.

Figure 4.19 shows the γ-γ coincident events for the α decay of ^{253}No. Correlations with the 279-, 221- and 150 keV transitions are seen. As the 221- and 150 keV transitions are in cascades, determined by the electron-γ coincidences, correlations may be expected. The 279 keV transition showed no coincidence with electrons in Figure 4.18. The lack of correlated events with conversion electrons would indicate a domination of γ emission of the transitions if a cascade is present. To determine if it is likely that the 279 keV transition is in a cascade, the rate of random coincidences must be determined.

To find out whether the observed γ-γ coincidences come from real events, the probability for how many events, R, that are expected to be random has to be determined. This can be calculated by the following equation:

$$R = 2 * \Delta(t) * \delta(\gamma) * \delta(\alpha\gamma). \tag{4.3}$$

above, i.e. the α decay will for example populate rotational bands built on the states. For the 279 keV transition, the flux from above is expected to be small compared to the directly feeding of the state. For the 209 keV state, the systematic trend is that the population of the 1st member of the band, a 7/2+ state, should be of similar intensity. From our statistics, with problems with the background, it is not really possible to tell the states apart as the 7/2+ to 5/2+ transition will sum up partially or totally with the α and give an apparent α of similar energy and nearly similar widths.

Where $\delta(\gamma)$ is the γ-rate, $\delta(\alpha\gamma)$ is the rate of α-γ coincident events and Δ(t) is the coincidence window. The γ-rate of the experiment was:

$$\delta(\gamma) = 380 \pm 10Hz \tag{4.4}$$

while the α-γ rate was found to be:

$$\delta(\alpha - \gamma) = 0.020 \pm 0.007Hz \tag{4.5}$$

The rate of a random γ-event being in coincidence with a α-γ coincident correlation can be determined by equation (4.3) with a coincidence window Δ(t) of 5 μs[7]. The rate is found to be:

$$R = 8 \pm 3 * 10^{-5}Hz \tag{4.6}$$

The γ rate was 380Hz, and with a total of $4.96{\cdot}10^8$ γ-rays detected, the run-time is found to be 13*10^5 seconds or 15.1 days. Given the total run time, the amount of random coincidences expected is given by the ratio of correlated event per second, R, multiplied by the total amount of seconds. In the α-γ matrix, 6.6 $\pm$ 0.2 % of the events where detected in the 279 γ peak in coincidence with the Nobelium decay. The number of random 279 keV γ coincidences is expected to be 6$\pm$3. The number of γ-γ coincidences shown in Figure 4.19 in the 279 keV transition peak is 6$\pm$1, which correspond to expected random coincidences.

Deexcitation correlations

In the previous section, it was found that the 221- and 150 keV transitions were in coincidence with other transitions. To determine the coincident transitions, the γ-electron spectrum for events correlated to ^{253}No α decay is studied. The spectrum in question is shown in Figure 4.20. The average binding energy of K, L and M transitions were given in Table 4.1. For the N orbital, the binding energy is between 1 and 2 keV [24]. As seen in the figure, the transition with γ energy 221 keV is in coincidence with an electron signal with energy of 53$\pm$20 keV. This energy corresponds to the MN conversion of a 58 keV transition. The binding energy of the K shell is higher than the transition energy resulting in no possible emission of K-shell electrons. The L transition is energetically possible, with an electron energy of about 30 keV, energy that in general will be below the energy threshold of the detector. The 58 keV transition is seen in the γ spectrum (see Figure 4.21). For the 150 keV transition, the highest energy of the electrons is

[7]The coincidence window used in α-γ coincidences

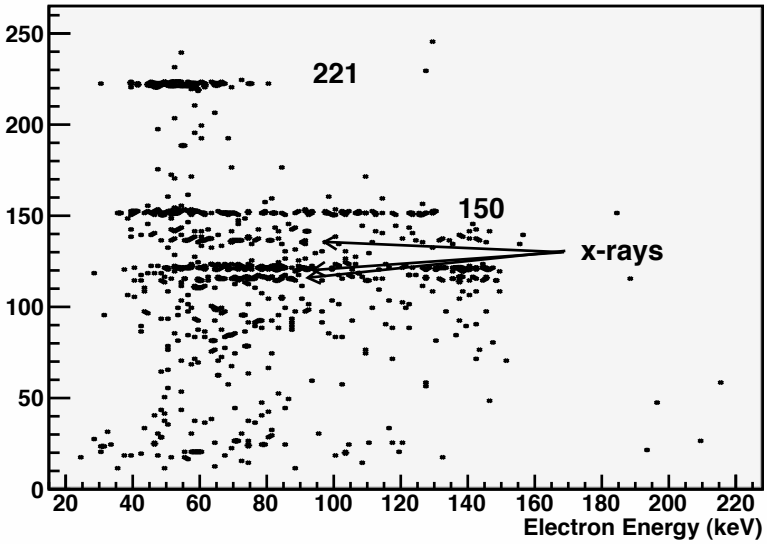

Figure 4.20: Electron-γ coincident events in correlation with ^{253}No α decay.

around 130 keV, indicating the internal conversion of a transition of similar energy. In the α-gated γ-ray spectrum of Figure 4.21, a peak around 129 keV can be seen, which supports the existence of a 129 keV transition in coincidence with the 150 γ-ray. Figure 4.22 shows the electron signals in coincidence with the above mentioned 221- and 150 keV transitions. The structure of the electron energy signal for the 221 keV transition is marked in blue, while the red histogram marks electrons in coincidence with the 150 keV transition. The peak structure of around energy 53 keV for the 58 keV transition is also present in the electron energy spectrum correlated to the 150 keV decay. In a 129 keV decay by conversion, electrons with energy $\sim$100 keV and $\sim$125 keV should be seen, i.e there should be electrons detected with energies from about 80 keV to around the transition energy. The peak structure around 53 keV in the 150 keV transition indicates that there, in addition to the 129 keV decay, is an other transition correlated to the 150 keV decay with transition energy of 58 keV. The 58 keV decay is coincidence with the 150 keV transition should be a lot weaker than the signal from the 221 keV transition as the 221 keV decay is of a higher yield than the 150 keV decay thus indicating 2 low energy transitions with similar electron energies in coincidence with the 150 keV transition. The conversion electron spectrum for the 150 keV correlated events is caused by three transitions of energy: 129-, 71-, and 58-keV. The L conversion of

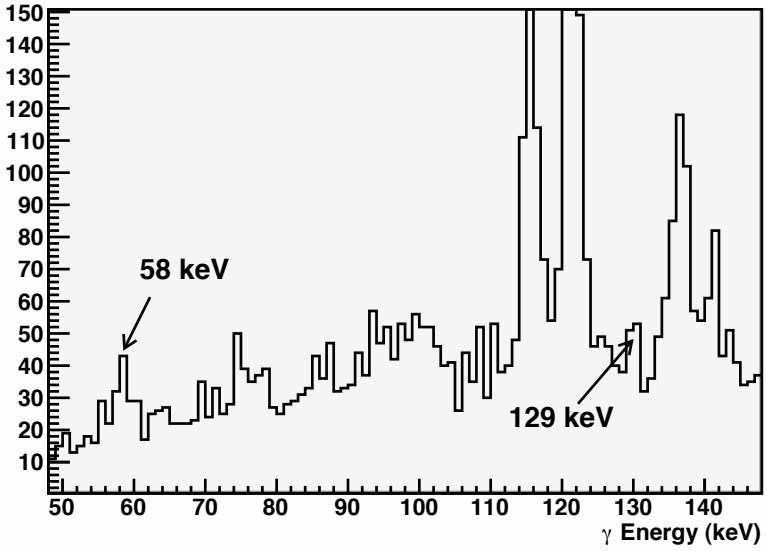

Figure 4.21: Identification of the 58 keV and 129 keV transitions in the γ-spectrum in coincidence with the α decay of ^{253}No.

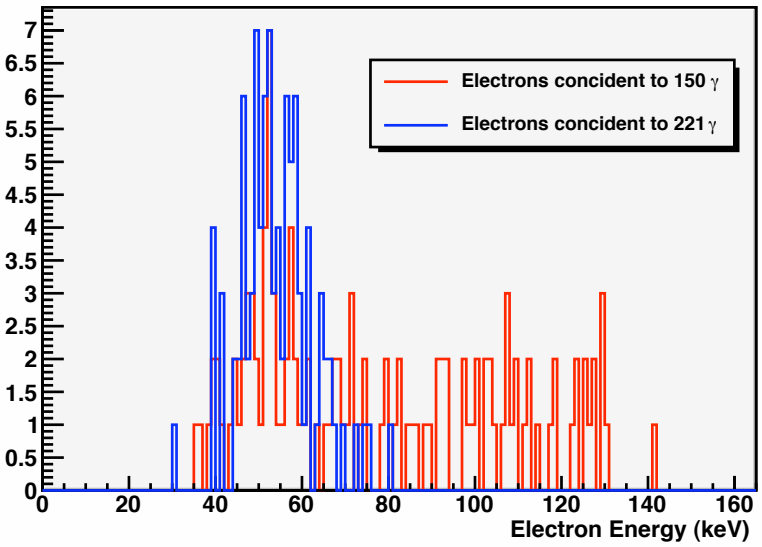

Figure 4.22: Comparison of the spectra of electrons in coincidence with the 150 keV and 221 keV transitions.

the 71 keV transition is of energy 47±20 keV overlapping the 58 keV M transition making the peak around 50 keV as strong as seen in Figure 4.22.

The 221 keV transition is determined to be in coincidence with one of energy 58 keV, summing up to 279 keV which was the excitation of the state fed by the 8006 keV α observed. To verify that the 221 keV transition is fed by this same α, Geant4 Monte Carlo simulations have been done [3]. The simulations were in good agreement with the experimental data. The findings support the picture of a 279 keV state depopulated by both the 279- and 221 kev transitions. It has been suggested that the 150 keV transition also is fed by this α decay [25, 19]. As argued in [3], a 150 keV transition from the 279 keV state implies the existence of a 129 keV state. The 150 keV transition is found to be in coincidence with ∼55 and ∼70 keV conversion electrons in addition to an electron signal of somewhat higher energy, corresponding to the conversion of the 58-, 71- and 129 keV transitions thus indicating 150 keV decay from the 279 keV state.

The α decay directly feeding the lower lying states discussed can be seen in Figure 4.16 as the correlated decays of energy higher than 8150 keV (channel 1630). The energy of the αs feeding these lower lying states can be calculated by rewriting the Q-value equation, (2.18), and are found to be α_{129}=8154±2 keV , α_{58}=8224±2 keV and α_{gs}=8281±2 keV for the feeding of the 129- and 58 keV band and the ground state.

4.2.3 Transition intensities

To find the conversion coefficient of a transition, one has to look at the intensities of the γ-ray and internal conversion electron peaks and find the ratio of these. Since the detectors are not ideal, the efficiency of the different types of detectors has to be taken into account. The efficiency of the tunnel detector and germanium detector array were discussed in section 3.4.2.

Determination of intensities

When determining the conversion coefficients, there are several aspects that have to be taken into consideration: the confidence intervals for γ and electron energies have to be decided, as do the cuts to be used in α energy for the different transitions. The confidence interval chosen is that of 2.35σ or a width of ±FWHM. The widths of the cuts used for the electron

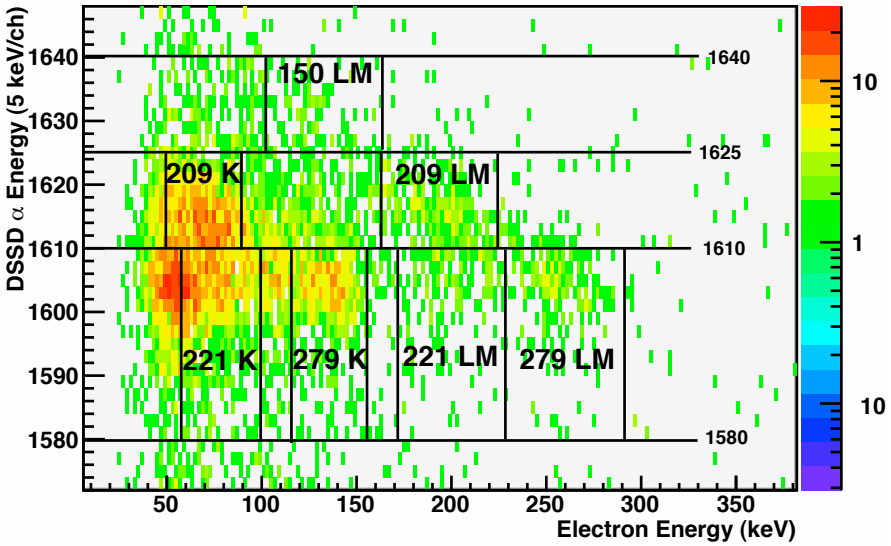

Figure 4.23: Cuts marked to obtain conversion electron intensities for the different transitions.

energy is ±20 keV, while ±3 keV is used in the case of the γ-ray transitions. Within this interval the majority of the true values are likely to be found [8] though overlap between signals will occur. Due to this overlap, *ML* transitions of the same transition energy are combined.

Figure 4.23 shows the electrons in coincidence with α energies corresponding to the ^{253}No decay with the approximate cuts used to find the different conversion coefficients marked. It is somewhat difficult to find an accurate count of the wanted signal due to the overlap of signals resulting in a higher count than the real value. The distinction of some of the signals can only be made by using different α energies. The cuts in the α-γ spectrum (see Figure 4.24) are made at the same energies as in the α-electron matrix. The choice of cuts in α energy will be explained further in the individual cases later in this section.

By being able to identify an area where the electron contribution is caused by a single transition X, the conversion coefficient for transition X can be found. By using this coefficient and the amount of γ-rays registered in

[8] The true value has a probability of ≈95.5% to lie within x± 2σ, where x is the energy of the radiation.

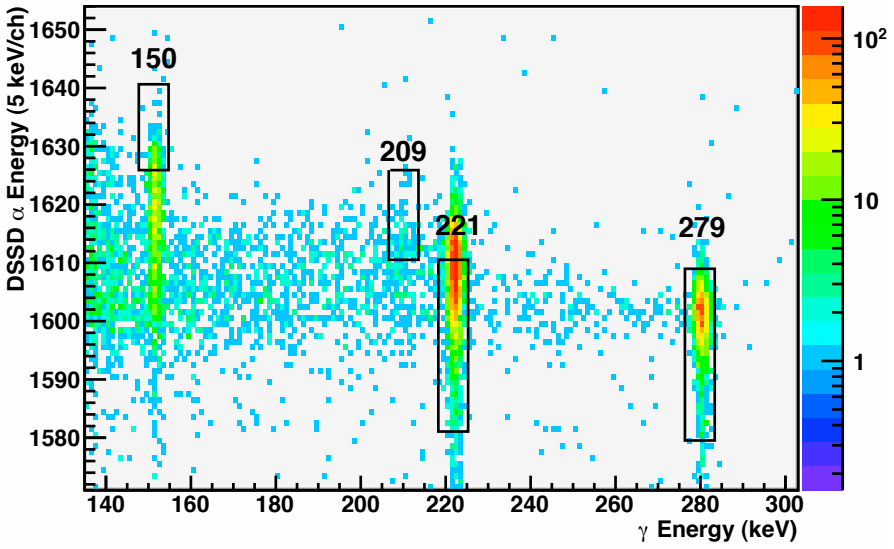

Figure 4.24: Selected areas used to determine the γ-ray intensities of the 150-, 209-, 221- and 279 keV transitions.

areas of overlapping electron signals, the contribution of the conversion X can be estimated and subtracted out. Doing this, it is possible to determine the conversion for the other transition in overlapping areas.

The first coefficient to be determined is the 279(LM) conversion. This conversion has no overlap with other transitions or background caused by transitions lying at higher energy. The γ and electron counts in the cuts (with the background subtracted) and the conversion coefficient found for the transition are given in Table 4.3. The efficiency of the γ rays of interest are given in Table 4.4. Using equation (2.29), the 279(LM) conversion coef-

Transistion	$I_{Electrons}$	I_γ	α_{trans}
279(LM)	181 ± 13	1352 ± 37	0.073 ± 0.017
221(LM)	46 ± 7	1948 ± 44	0.015 ± 0.004
209(LM)	224 ± 26	43 ± 7	3.37 ± 1.35
150(LM)	66 ± 8	209 ± 14	0.06 ± 0.03
279(K)	225 ± 15	878 ± 30	0.14 ± 0.03

Table 4.3: Calculated conversion coefficients for transition energies associated with the α decay of ^{253}No.

γ-Energy (keV)	ϵ (%)
279	9.8±1.0
221	11.3±1.1
209	11.6±1.2
150	13.9±1.4
129	15.0±1.5
71	15.4±1.5
58	13.6±1.4

Table 4.4: Efficiency of the γ-ray detectors for transitions associated with ^{253}No decay.

ficient was found to be 0.073±0.017.

The determination of the 221(ML) conversion coefficient has to be done in correspondence with the determination of the 209 keV conversion. The 209 keV transition is, as discussed in section 4.2.2, in coincidence with a 8085±3 keV α and decays directly to the ground state. As the 8085 keV α is centered around channel 1617 and the α energy resolution is ∼6 channels, by making the 221 cut under channel 1608 the probability of a detected signal in the cut originating from the 209 decay is acceptably low. After the 221 keV conversion coefficient has been determined, the amount of 221 keV γ-rays in the cut used for the 209 keV transition (channels 1610-1625) can be used to determine the corresponding amount of 221 *LM* electrons in the cut. It is then possible to obtain a good conversion coefficient for the 209 keV *LM* decay. A similar approach is used for the determination of the 150 keV *LM* and 279 keV *K* transitions. The 150 keV *LM* cut is made above the 279 keV α-γ coincident events, as shown in Figure 4.23. In this cut, there should not be any background caused by other transitions discussed here, except at high α energies where additional events come from direct feeding of lower lying states; for example the α decay directly to the 129 keV state. An estimation of this background is made by finding an average background per channel in an area to the sides of the 150 *ML* cut and assuming it represents the average background level in the cut. When the 150 keV *LM* conversion coefficient is determined, the 279 *K* conversion can be found by correcting for the amount of 150 keV conversion electrons present in the cut. The results from the calculations are given in Table 4.3.

Looking at Figure 4.23, the determination of the conversion coefficients for the 221(*K*) and the 209(*K*) transitions are problematic. As for the *ML*

transitions, the signals are overlapping. In addition to this, a strong 58 keV conversion signal overlaps both cuts. For the 221(K) conversion, this might be corrected for by assuming a Gaussian distribution of the counts in the cut and use the value of the right half of the cut (80-100) multiplied by two. By selecting a cut which should not include the conversion electrons from the 58- or the 209-keV conversion electrons, a coefficient of 0.18 ± 0.04 is obtained. This value is a too high an estimate as conversion electrons from the 71 keV and 129 keV state will be present in the cut. Though the intensities of these transitions are relatively low, the decays are highly converted resulting in the coefficient obtained being elevated compared to the true value. By not being able to determine the conversion coefficient for the 221(K) transition and not knowing the number of overlapping electrons caused by conversion of the 58- and 71-keV decays, the determination of a conversion coefficient for the 209(K) transition is impossible.

Figure 4.25 shows the experimentally determined conversion coefficients for the LM transitions and how they compare to the theoretical values. The conversion coefficients determined experimentally are marked in green while the blue and red lines are the theoretical values for the 2 first multipoles for magnetic (M) and electric (E) transitions respectively. By comparing experimentally obtained results with the theory, the transition types can be determined. There is a good agreement for $E1$ transition type for the 150 and 221 keV decay, as is in accordance with previous results [3, 19, 25]. Though the conversion coefficient found is somewhat larger than the theoretical value, the 209 keV decay is likely to be of type $M1$ as this is the closest value. The conversion coefficient for the 279 keV transition diverge from the theoretical value, a result in agreement with the findings by Lopez-Martens *et al*, [3]. While irregularities for the 209 keV decay, in parts could be explained by low statistics, overlap of signals in the electron spectrum and high level of background, these possible sources of error are not valid for the 279 keV transition. The decay is of high intensity, the background low, and the LM conversion is clearly separated from other signals. Also, the K conversion for the 279 keV decay, as shown in Figure 4.26, again has a large conversion coefficient. The transition is believed to be an $E1$ transition due to systematics as will be further discussed in section 4.3.1. Looking at the LM conversion, the value is closest to $E1$ but the K conversion is closer to $E2$, making these the likely candidates for the transition. However, for $E2$ transitions the

$$\frac{K}{L} < 1 \tag{4.7}$$

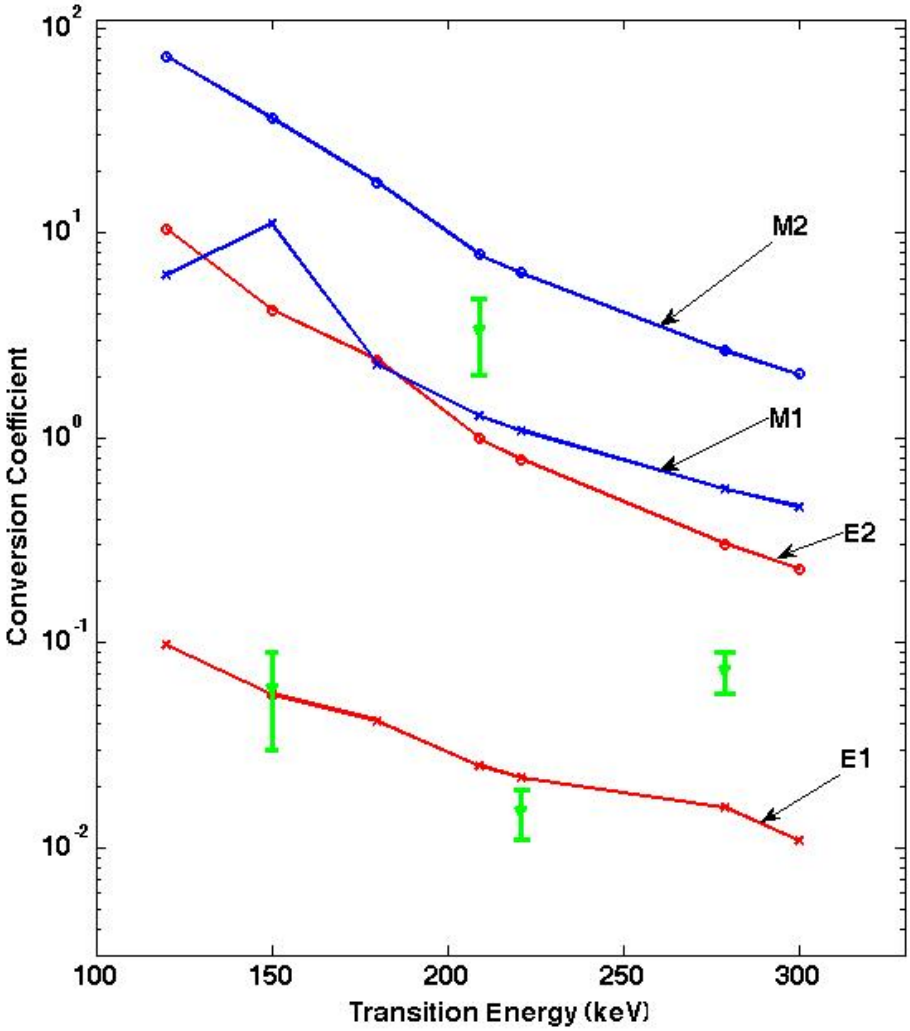

Figure 4.25: Theoretical *LM* conversion coefficients for E1, E2, M1 and M2 transitions and experimental results.

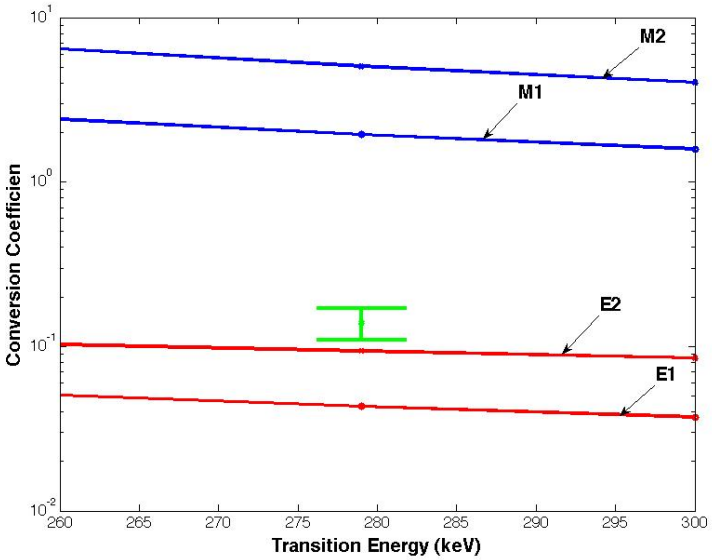

Figure 4.26: Theoretical K conversion coefficients for E1, E2, M1 and M2 transitions and experimental result for the 279 keV K conversion.

K x-rays	Raw count	efficiency	Total counts
$\sim$ 115 keV	379$\pm$19	0.157$\pm$0.02	2395 $\pm$363
$\sim$ 120 keV	605$\pm$25	0.155$\pm$0.02	3903$\pm$549
$\sim$ 140keV	396$\pm$20	0.143$\pm$0.01	2766$\pm$416
Total			9064$\pm$778

Table 4.5: Amount of x-rays detected

relationship is valid. As noted in Table 4.3, the K conversion coefficient is larger than that of LM, excluding $E2$ transition as a candidate. A possible explanation for a large $E1$ conversion could be the existence of an other highly converted transition of similar energy. However, the existence of $E1$ transitions with large irregularities compared to the theoretical values is not uncommon in heavy deformed nuclei, like the nucleus in question, as is further discussed in Appendix B. The two possible scenarios can be separated by looking at the x-rays. The theoretical conversion coefficients α_K are taken from the BRICC database [7]. From this information and the experimental γ-ray intensities, the amount of x-rays can be estimated and should correspond to the experimental value. Table 4.5 gives the amount of K x-rays detected and the expected total amount of x-rays with the de-

tector efficiency taken into consideration. This number is to be compared to the estimated number of x-rays calculated from the number of γ-rays in the peaks and the conversion coefficient. The total number of x-rays expected is found by the summation of x-rays of all transitions.

$$\begin{array}{l} \mathrm{I}_{\gamma_{279}} \rightarrow \mathrm{I}_{K_{279}} \\ \mathrm{I}_{\gamma_{221}} \rightarrow \mathrm{I}_{K_{221}} \\ \mathrm{I}_{\gamma_{209}} \rightarrow \mathrm{I}_{K_{209}} \\ \mathrm{I}_{\gamma_{150}} \rightarrow \mathrm{I}_{K_{150}} \\ \hline \Sigma\text{x-ray} \end{array}$$

To find the expected number of x-rays for the different transitions, the intensity of the γ peak, γ_{peak}, and the total amount of γs expected to have been emitted, γ_{total}, found by correcting for the detector efficiency, ϵ, for the given γ energy.

$$\gamma_{total} = \gamma_{peak} \cdot \epsilon \tag{4.8}$$

Using the conversion coefficient, α_K, it is possible to estimate the total amount of x-rays, $x - ray_{total}$, being emitted from the given transition:

$$x - ray_{total} = \gamma_{total} \cdot \alpha_K \tag{4.9}$$

The character of the 279-, 221-, and 150 keV transitions are $E1$ while the conversion coefficient of the 209 keV transition indicates a $M1$ character. The values found can be seen in Table 4.6. The total amount of x-rays emitted, is 9064$\pm$778. The expected value of x-rays, using the BRICC conversion coefficients is 7740$\pm$1155, which does not match the experimental result. By using the experimentally determined coefficient for the 279 keV decay, the amount of x-rays emitted corresponds well to the expected value of 9369$\pm$1654 events. This result indicates that the 279 keV transition has an anomalous $E1$ character.

Strength of the transitions

The branching of the transitions can be determined by looking at the intensities of the transitions. In Table 4.7 the data used in the calculations are given. The total strength of a transition, I_{tot}, is given by the number of γ-rays detected, I_γ, corrected for detector efficiency, ϵ_γ, and conversion,

Energy trans.	# γ	efficiency	$\alpha(\mathrm{K})_{BRICC}$	x-ray
[1]279 keV	1695 ±41	0.098±0.010	0.0431	725± 163
[2]279 keV	1695 ±41	0.098±0.010	0.14±0.03	2353±1195
221 keV	4453±67	0,113± 0.011	0.0776	2989 ±643
209 keV	80±9	0,116±0,012	4.36	2922±911
150 keV	983±31	0,139±0,014	0.1607	1105±256
[1]Total				7740±1155
[2]Total				9369±1654

Table 4.6: Amount of X-rays expected using all BRICC coefficients ([1]) and using calculated conversion coefficient from the 279 keV transition ([2]).

Transition (keV)	I_γ	ϵ_γ	α_{tot}	I_{tot}
279($E1$)	1729±42	0.098±0.0098	0.21±0.095	21333±12186
221($E1$)	4536±67	0.113±0.011	0.0922	43948±5047
150($E1$)	984±31	0.139±0,014	0.217	8589±1133
129($E2$)	28±5	0.150±0.015	8.249	4189±927
58(M1)	80±9	0.136±0.014	51.37	40014 ±4964
58(E2)	80±9	0.136±0.014	345.4	264672 ±30397

Table 4.7: The amount of γ-rays detected, I_γ, the efficiency, ϵ_γ, conversion coefficient, α_{tot}, and the calculated total amount of γ-rays emitted, $I_{\gamma(tot)}$, for the given transitions of characters marked in parenthesis.

Transition, x, (keV)	S_x (%)
279	29 ±9
221	59±17
150	12±4

Table 4.8: The strengt of the different transitions from the 9/2- state.

α_{tot}. The total number of emitted γ-rays, $I_{\gamma(tot)}$, from the given transition is:

$$I_{\gamma(tot)} = \frac{I_\gamma}{\epsilon_\gamma}. \tag{4.10}$$

The total strength of the transitions, I_{tot} is the sum of γ-rays, $I_{\gamma(tot)}$, and conversion electrons, I_{ce}, emitted

$$I_{tot} = I_{\gamma(tot)} + I_{ce} \tag{4.11}$$

The 279, 221 and 150 keV transitions are, as previously discussed, transitions from the same state of energy 279 keV. The data for the decay from this state or in coincidence with transitions from this state is given in Table 4.7. The total number of decays from the 279 keV state, I_{state}, is the summation of the total decay for each of the three energies, giving a total of

$$I_{state} = I_{tot(279)} + I_{tot(221)} + I_{tot(150)} \tag{4.12}$$

The strength, S_x, of the decay x can be determined by

$$S_x = \frac{I_{tot(x)}}{I_{state}}. \tag{4.13}$$

Results for the 279, 221 and 150 keV decays are given in Table 4.8. The dominant transition is the 221 keV decay with a transition probability of 59±17 %. The second strongest decay is that of 279 keV with S_{279}=29 ±9% while the 150 keV transition accounts for 12±4 % of the total decays from the state.

In Table 4.7 and Table 4.8, theoretical conversion coefficients are used except for the case of the 279 keV transition for which the experimentally determined value gives a better representation of the data.

The 150 keV decay branches, and can either go straight to the ground state of decay by an 129 keV transition or via the first excited state with 71 keV

and 58 keV transitions. As discussed in section 4.3.1, the transition types of these decays need to be of type $M1$ or $E2$. The 129 keV decay is most likely an $E2$ transition. The fraction of decay by the 129 keV transition, assuming $E2$ decay, is 20±8 % rendering the 71 keV + 58 keV transition a probability of ∼80%.

As the strongest transition is that of the 221 keV decay and it is feeding a 58 keV state with no branching, the majority of the 58 keV γ-rays seen will come from this transition. The number of 58 keV γ-rays expected to be seen in the spectrum from the 221 keV decay can be estimated by

$$I_{\gamma(tot(58))} = I_{tot(221)} \frac{1}{1+\alpha_{tot58}} \tag{4.14}$$

where $I_{\gamma(tot(58))}$ is the total number of γ-rays emitted from the transition. This value needs to be corrected for detector efficiency. $I_{tot(221)}$ is the total number of 221 keV γs and α_{tot58} is the total conversion coefficient for a 58 keV transition in Fermium. The 58 keV transition must, as preciously mentioned, be a $M1$ or $E2$ transition. As can be seen in Table 4.7, the conversion coefficients for these types of transitions are very different. First assuming a $M1$ transition and just looking at the 221 keV transition, one should expect to see 114±25 γ-rays of energy 58 keV. As the 150 keV transition also feeds the 58 keV state, the total number of 58 keV γs should be somewhat larger (198±69 γs)[9]. The 58 keV peak detected in the α-γ coincident spectrum for the Nobelium decay has a total count with background subtracted of 80±9. The number of 58 keV γs expected to be seen are significantly smaller than expected from a pure $M1$ transition. If assuming the 58 keV transition is of type $E2$, the expected number of γ-rays seen is 30±10 with feeding from 150 keV transition also taken into consideration, witch again is a too low estimate. The results indicate a mixed $M1$ and $E2$ state with a dominating $M1$ component.

No clear γ-peak from the 71 keV decay could be detected, though a hint of a peak is seen. This indicates a highly converted transition type. If assuming a branching of the decay from the 150 keV transition as found here, the number of γ-rays expected to be seen is 35±13 for a $M1$ transition and 8±5 for a $E2$ transition. The 71 keV seems to most likely be a mixed $M1(E2)$ transition. As the decay signal can not be separated sufficiently from background in either the γ or electron spectrum in coincidence with the correlated α decay, this result is based on what is not seen and making the result highly uncertain. The likelihood of decays by emission of γ-rays

[9] Estimate assumes branching as determined here and a 129 keV transition of type $E2$.

Trasition and character	fraction γ-decay (%)
279 keV ($E1$)	82±22
221 keV ($E1$)	92±21
150 keV ($E1$)	82±22
129 keV ($E2$)	11±6
71 keV ($E2$)	0.8±1
71 keV ($M1$)	0.0002±0.0002
58 keV ($M1$)	1.9±0.6
58 keV ($E2$)	0.3±0.1

Table 4.9: The fraction of γ-decay emission for decay of excited states in ^{249}Fm.

ID	α-energy	γ -energy
1	7615±35	670±4
2	6889±9	570±3
3	6282±9	352±2
4	6670±8	272±2
5	7565±45	24±3
6	7100±28	353±3

Table 4.10: The α-particle and γ-ray energies of the coincidences marked in Figure 4.7.

for the different transitions are given in Table 4.9.

In the α decay of ^{253}No, the 9/2- state is fed ∼90% of the time, while decay to the 5/2+ state has a ∼10% probability of occurring. The decay from the 5/2+ state will 15±5 % of the time decay by γ-ray emission.

4.2.4 Identification of other decays

As marked in Figure 4.7, other α-γ correlated decays can be seen in the matrix. The positions and corresponding energies of the marked correlations are given in Table 4.10. One of the main tools in identifying the nucleus undergoing the decay observed, is calculating the Q-value of the decay. When a given (α-γ) coincidence is observed, one can guess at the identity of the decaying nucleus by examining the Q-values of the nuclei likely to

be produced. By then calculating the Q-value, using equation (2.18), and comparing this to the table value of the decay, one will get an indication if it is a likely identification or not.

The signal marked 1 in Figure 4.7 corresponds to an α-particle energy of 7615$\pm$35 keV and a γ-ray energy of 670$\pm$4 keV. Looking at known α and γ decay combinations of nuclei in the area likely to be produced, no possible alternatives are found. This transition may be associated to the decay of another state in ^{249}Fm, populated in the α-decay of ^{235}No. **A Q-value calculation based on this assumption renders a Q-value of 8417$\pm$35 keV, wich is in correspondence with the Q-value found for the α decay of ^{253}No of 8414$\pm$2 keV , making the 670 keV transition a likely transition to the ground state in ^{249}Fm.** If looking at decay schemes of similar nuclei, which will be discussed in section 4.3.1, this transition would be the decay from a single particle excitation state and expected to be seen in ^{253}No α decay with high statistics. There are no signals in the conversion electron spectrum in Figure 4.8 at energies corresponding to K or LM conversion of Fermium, indicating a transition dominated by γ ray emission. For the given γ energy in question, γ decay is the dominant channel in all transition types [7]. The number of K-electrons expected to be seen for $M2$ and $M1$ transitions are respectively 7$\pm$4 and 3$\pm$2 count while no electrons are expected to be seen for K-transitions of type $E1$ or $E2$: making an electric character more likely, though a $M1$ transition could also be possible.

The decay marked 2 is that of an α with energy 6889$\pm$9 keV in coincidence with a 570$\pm$3 keV γ. The energy of this correlation fits with the decay of ^{211}Po produced in the run. However, seen in the level-scheme for the ^{211}Po α decay, as given in Appendix G, a higher lying orbital of 898 keV is fed by the α decay. The 569 keV transition is fed by an α of energy 6892 keV while the 898 keV transition is in coincidence with a 6568 keV α. The 570 keV and 898 keV γ-rays in the ^{211}Po α decay are emitted with similar intensities [20]. Figure 4.27 shows the α signal in coincidence with the 570 keV γ ray. The number of counts in the peak is 10$\pm$3. Correcting for the variation of γ detector efficiency at different γ energies, the number of counts expected to be detected for the 898 keV γ in coincidence with the 6892 keV α is 7$\pm$3. Figure 4.28 shows the α spectrum coincident with a 898 keV γ for the area where the α from the ^{211}Po decay should be located, at channel 1314. As is marked in the figure, no signal is detected, indicating that the 6889 keV - 570 keV α-γ signal is of a different origin than the ^{211}Po decay or that the number of counts in the 898 keV peak deviates by $\geq 2\sigma$.

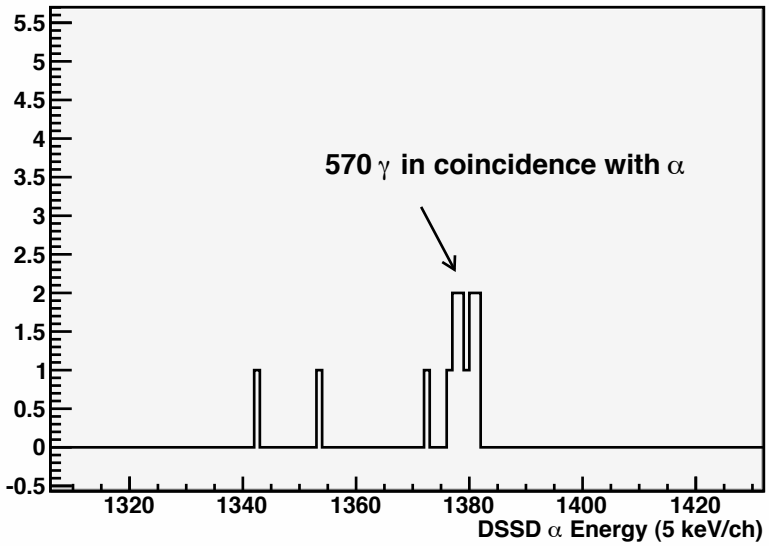

Figure 4.27: Energy spectrum of the α particles in coincidence with a 570 keV γ-ray.

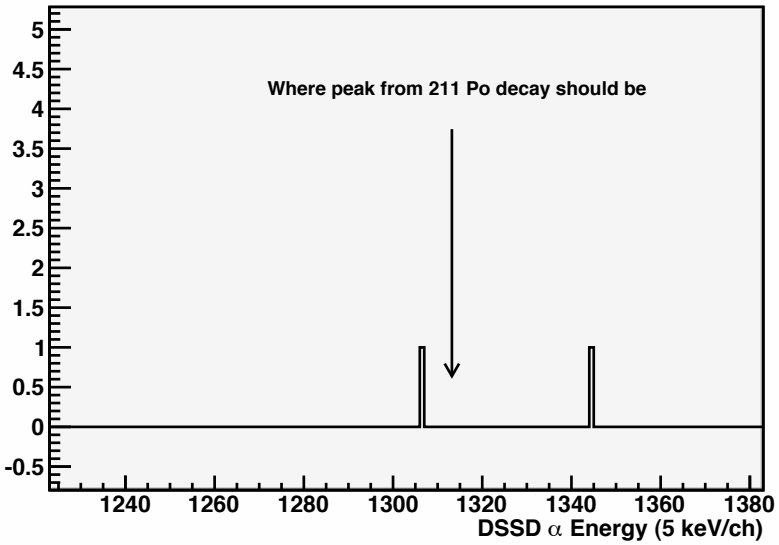

Figure 4.28: Energy spectrum of the α particles in coincidence with a 898 keV γ-ray

It has been proposed that the α of 7100$\pm$28 keV with its correlated γ of 353$\pm$3 keV could come from α decay of ^{253}Md [26]. ^{253}Md is an isotope created by electron capture of ^{253}No. The Q-value of this possible ^{253}Md decay is 7568$\pm$28 keV. Summed up, the energy detected from this decay is similar to the 570 keV and 6889 keV decay, indicating a possible connection. **Calculating the Q-value for the γ(570 keV) and α(6889 keV) decay assuming a ^{253}Md α decay, the value obtained is 7570$\pm$9 keV. The results indicates the 570 keV-6889 keV transition may be a transition in ^{253}Md not previously seen.** Looking at the intensities though, the 6889 keV α-particle - 570 keV γ correlation is a lot more intense than the other correlation mentioned, something that would upset the systematics of the α decay of the odd Md isotopes [27].

The 6282$\pm$9 keV - 352$\pm$2 keV decay signal marked as 3 is a decay from ^{211}Bi while signal number 4 of α energy 6670$\pm$8 keV and γ energy of 272$\pm$3 keV is from the α decay of ^{253}Fm to ^{249}Cf. For the Fermium decay, conversion signals can be detected and are marked 2 in Figure 4.8. The conversion coefficient calculated for this decay has K and LM transition of 0.35$\pm$0.16 for the LM transition and 0.22$\pm$11 for K. The total conversion coefficient of the decay is the sum of the K and LM transitions as the LM cuts made include conversion of electrons of all higher lying orbitals. The total conversion of this decay is found to be 0.57$\pm$0.2. Looking at the total conversion coefficients for californium for the transition energy in question, the theoretical coefficients for likely transitions are as follows:

$$\alpha_{tot(E1)}=0.0592$$
$$\alpha_{tot(M1)}=1.73$$
$$\alpha_{tot(E2)}=0.3716$$
$$\alpha_{tot(M2)}=7.139$$

Comparing the experimentally obtained results to the theoretical values [7], the transition is likely to have a $E2$ character. For the $E2$ transition the LM transition is of higher convergence than the K transition[10], which corresponds well with the data obtained. Looking at the level scheme of this decay [28], the 271.8 keV transition is the one of highest yield in the α decay of ^{253}Fm and is noted as having an $E2$ character. For the ^{211}Bi decay, no clear conversion signal can be detected.

In Figure 4.7, the decay signal marked 5 corresponds to the energy of α

[10] $\alpha_{E2(K)}$=0.09482, $\alpha_{E2(LM)}$=0.27688

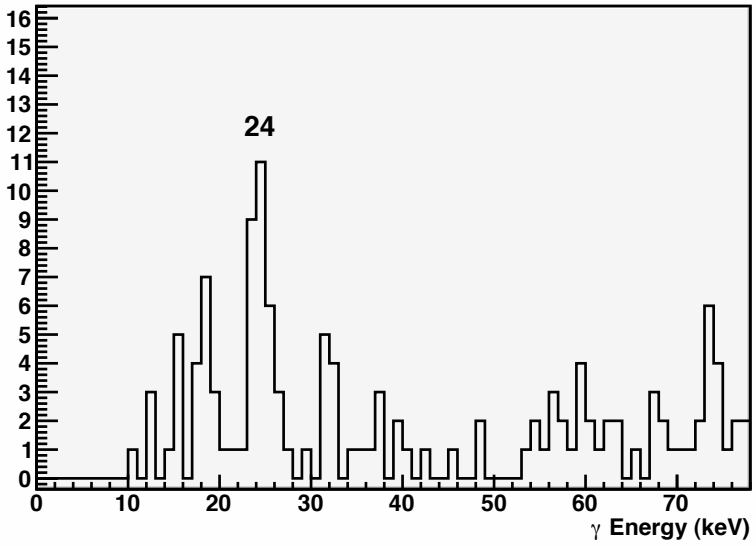

Figure 4.29: γ-rays in coincidence with α of energy $\sim$7.5 MeV

decay of ^{249}Fm. Hessberger *et al* [25] argued that ^{249}Fm in parts decays to a low lying level (55 keV) in ^{245}Cf that nearly exclusively decays by conversion. In the experiment discussed in this article, no α-γ correlated events for the decay was registered and the assumption of the feeding of the excited state in ^{245}Cf was based on a study of the α spectrum. The data presented in this thesis contains higher statistics and α-γ correlated events are detected for the Fermium decay in question. Figure 4.29 shows γ-rays detected in coincidence with the α decay of ^{249}Fm. A relatively strong peak can be seen around 24 keV in addition to a weaker line below 20 keV. This lowest energy peak is in fact a 21 keV line. The positioning of the peak is slightly off as the ADC is possibly non linear at the very bottom of its range. The 21 keV peak has less counts than the 24 keV peak because its intensity is seriously attenuated[11]. The two lines seen are L x-rays following a converted transition in ^{245}Cf. The transition is most likely an $E2$ transition, as a transition of $M1$ character would have given a γ peak. Also, $M1$ conversion favors $L1$ orbitals, which would mainly have given a peak at 24 keV. The $E2$ transitions favors $L2$-$L3$ which would give two peaks at 24-

[11]The attenuation is caused by interactions in the Si DSSD, the Al back-flange of the chamber and/or the Al cap of the Ge detector. The attenuation varies tremendously between the two γ-rays. The half thickness of a 20 keV γ in Al is 0.7 mm while it for a 30 keV γ is 2 mm of Al. The 21 keV peak is as, if not more, intense than the 24 keV in raw intensities, but gets cut off by the material.

and 20 keV. The fact that 2 peaks are seen indicates an $E2$ transitions. The results found support the decay scheme established by Hessberger [25].

4.3 Discussion

In this discussion section the results of the α decay of ^{253}No will be discussed in the light of the systematics of single-particle levels in N=149 isotones and compared to theoretical calculations.

4.3.1 Systematics

^{249}Fm is a N=149 isotone like ^{247}Cf, ^{245}Cm and ^{243}Pu. It is interesting to compare the 149 isotones where the protons are paired up (A is odd). The level schemes of isotones around ^{249}Fm should have a similar structure as they should consist of rotational bands built on top of single particle states caused by the excitation of the unbound neutron.

The level schemes of the isotones ^{247}Cf, ^{245}Cm and ^{243}Pu are given in Figure 4.30, Figure 4.31 and Figure 4.32. The groundstate of the nuclei and mother nuclei if interest are 7/2+ and 9/2- respectively. The fist two excited states in the isotones are rotational bands built on the groundstate with spin parity of 9/2+ and 11/2+ and energy of $\sim$55 keV and $\sim$125 keV. These states are by part fed by the decay from the 9/2- single particle excited state, and are marked in red in the figures. The strongest α-decay line is from the 9/2- groundstate in the mother nucleus to an excited 9/2- state in the daughter nucleus. The identical spin and parity of the states makes this transition as strong as it is. The 9/2- excited state can decay to the ground state or one of the first two excited states previously discussed. The strongest transition is to the 9/2+ first excited state, while the 11/2+ second excited state and the ground state is populated approximately equally strong by the decay from the 9/2- level. The transitions from the 9/2- state are all $E1$ and the energy of the state is about 300-400 keV.

A low lying excited single particle state, marked in green, is a 5/2+ state decaying by a $M1$ or mixed $M1$+$E2$ transition mainly to the ground state. Decay from this state to the ground state is the strongest transition after the ones caused by the decay from the 9/2- state. A third excited single particle state, 7/2-, is weakly populated and has an energy of about 600-700 keV.

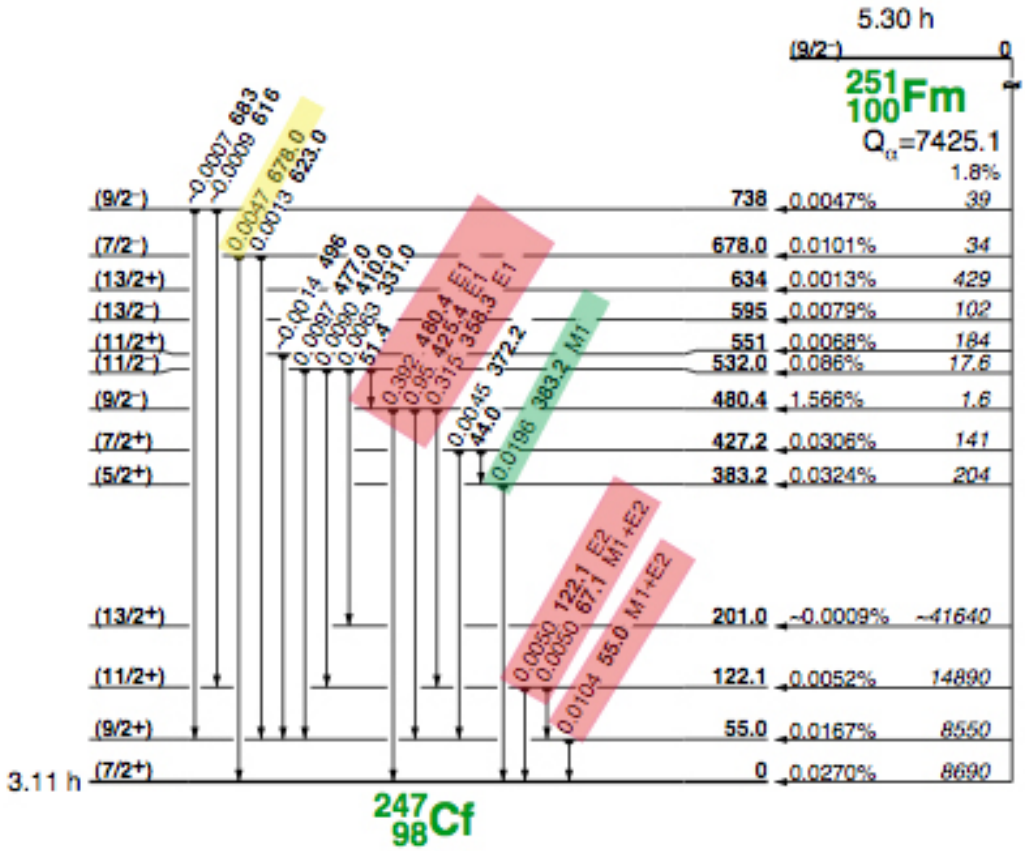

Figure 4.30: Level scheme of ^{247}Cf [28]. The transition de-exciting the first excited single-particle state populated in the α-decay of ^{251}Fm is marked in green while those involved in the decay of the 2nd and 3rd single-particle states are marked red and yellow.

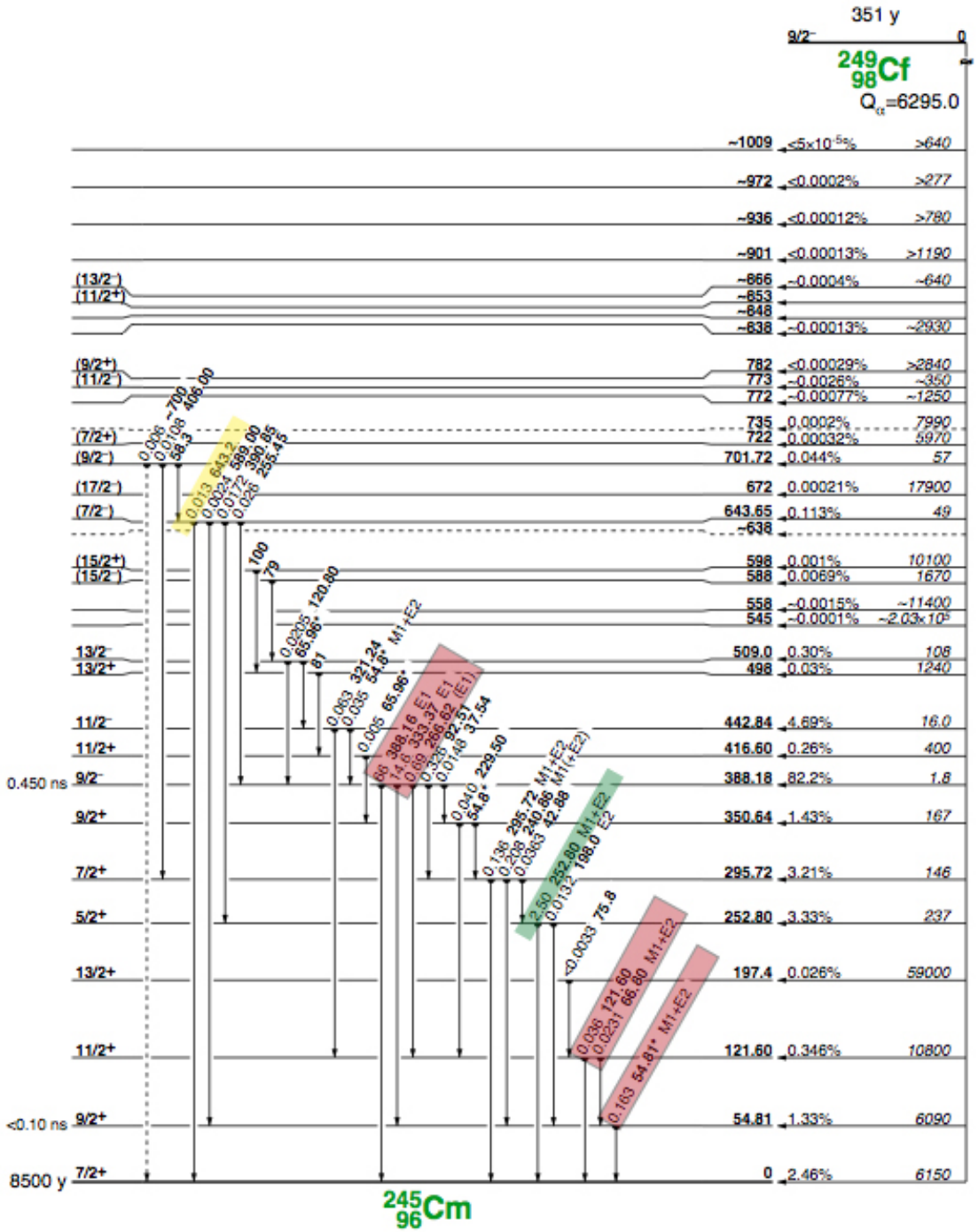

Figure 4.31: Level scheme of ^{245}Cm [28]. The transition de-exciting the first excited single-particle state populated in the α-decay of ^{249}Cf is marked in green while those involved in the decay of the 2nd and 3rd single-particle states are marked red and yellow.

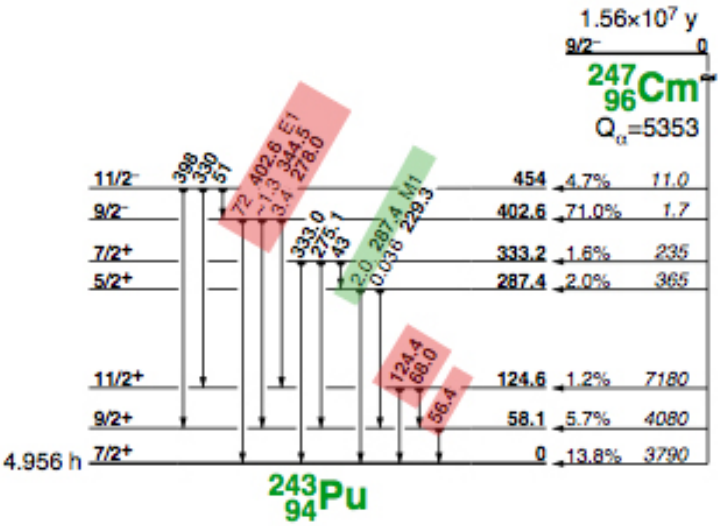

Figure 4.32: Level scheme of ^{243}Pu [28]. The transition de-exciting the first excited single-particle state populated in the α-decay of ^{247}Cm is marked in green while those involved in the decay of the 2nd and 3rd single-particle states are marked red and yellow.

To determine how the theories correspond to the experimental results, the Nilsson predictions are compared to the experimental results.

4.3.2 Nilsson

Figrure 4.33 shows the Nilsson diagram for neutrons in the area of interest. The diagram shows how the spin-orbit splitting of the different neutron levels depends on deformation of the nuclei. A basis for the diagram is a potential well of the nucleus with quantified levels obtained by solving the Shrödinger equation for the system. In the diagram shown in Figure 4.33 the Wood Saxon potential was used as a basis. The solutions obtained renders the oscillator shells N=0, 1, 2... These shells will split into $l(l+1)$[12] sub-levels by orbital splitting. Giving s(l=0), p(l=1), d(l=2), f(l=3), g(l=4), h(l=5), i(l=6), j(l=7) and so on, the N=0 shell will, by orbital splitting, give rise to a 1s level, while the level obtained due to N=1 is 1p. At higher oscillator shells, several levels are obtained per shell; 1d and 2s for N=2, 1f and 2p for N=3 and so on. An even numbered shell, can only be split into even numbered sub-shells, s, d, g, i, who are of positive parity. Further splitting of the orbitals occurs due to spin s. The total angular momentum j=$l\pm s$ will for instance split the 1p shell into 1p3/2 and 1p1/2 levels. The orientation of the spin in deformed nuclei push the levels away from each other as can be seen by the change of energy of levels with deformation.

In Figure 4.33, each sub-level is identified by three quantum numbers in brackets, $[N..]$, where the important number is the first, N. The orbitals of interest in this discussion are green. As can be seen of the first quantum number N of theses states, their origin is mainly the 6^{th} shell in the Wood Saxon potential. An exception from this is the $j_{15/2}$ state of negative parity from the N=7 shell that is pressed down into the 6th oscillator shell. The energies, ordering and spacings of the levels in Figure 4.33 are the result of a calculation and may vary with different parametrisations of the nuclear force potential.

In the diagram, there is room for two particles in each orbital and the circled numbers represent neutron numbers of predicted large shell gaps. The y scale in the diagram also represents single particle energy. ^{249}Fm has an even number of protons and an odd number of neutrons, making one neutron uncoupled and giving rise to excited states caused by neu-

[12] l is the angular momentum of the level.

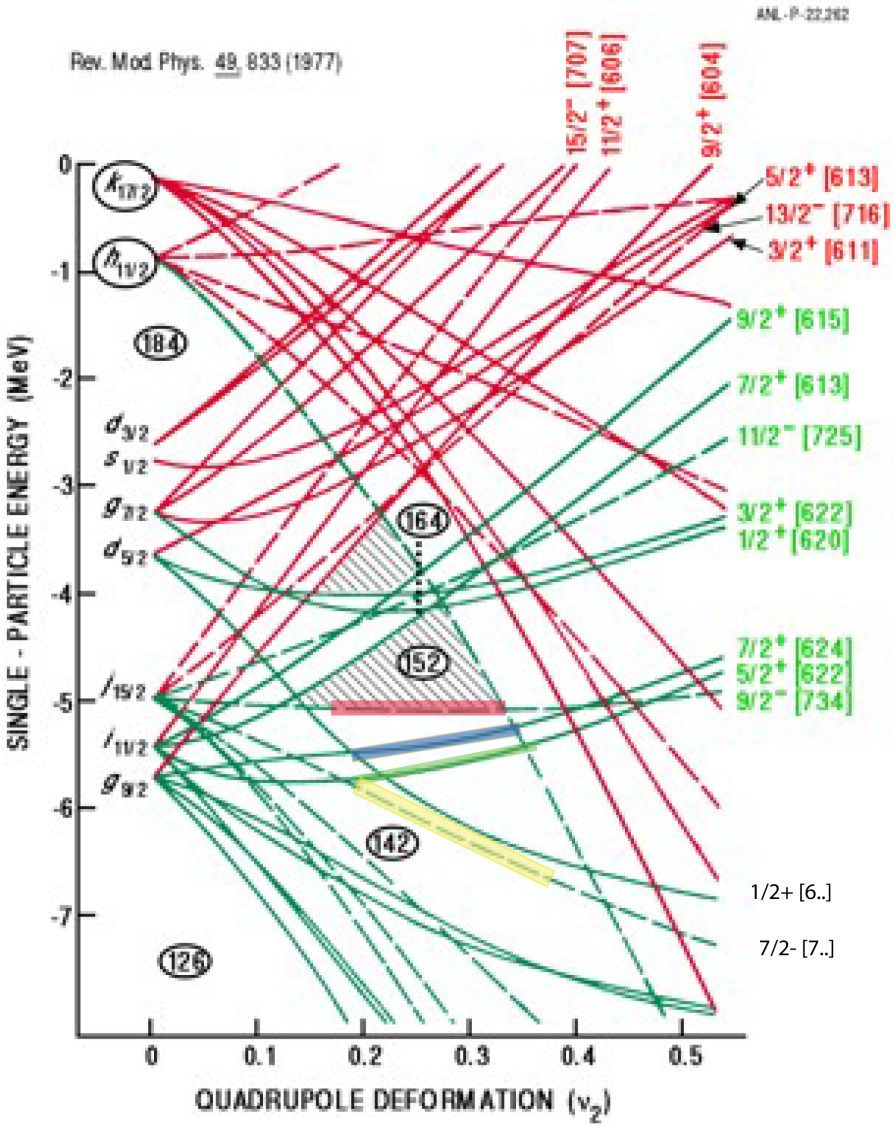

Figure 4.33: Nilsson diagram for neutrons in the region of interest.

tron excitation. The following discussion is valid for nuclei similar to that of ^{249}Fm, i.e. consisting of 149 neutrons and an even number of protons.

When reading this Nilsson diagram, one enters at the neutron ground state, determined by the number of neutrons and the deformation of the nucleus. The neutron number of interest is 149, as is the number of neutrons in ^{249}Fm. From the gaps visible in the Nilsson diagrams for neutrons (and protons, see Figure 4.37), theory predicts a deformation $\sim$0.2 to $\sim$0.4. This corresponds to the 7/2+ orbital marked in blue which fits with the experimental data. Within the mentioned deformation range, the ordering of the single particle states for the low single particle states are well reproduced by theory. Excited states can be obtained by exciting the single neutron up to a higher lying orbital, a particle excitation, or by the excitation of a particle of a lower lying states up to the orbital with the single neutron or higher, an hole excitation. The first single particle excited state should be the state that lies closest to the ground state in the Nilsson diagram at the given deformation. In this case, the first excited single particle state would be a hole excitation from the 5/2+ state. This state is marked green. The following single particle excitation state will be the red marked 9/2- state or the yellow 7/2- state depending on the deformation of the nucleus. The Nilsson diagram predicts a 1/2 orbital very close to the 7/2- but this is extremely weakly populated in the α decay and was not observed.

As discussed, the Nilsson diagram gives the single particle excitation states and, since the nucleus is deformed, the first state observed in the Nilsson diagram is not likely to be the first excited state as rotational orbitals are built on the single particle states. These types of excited states will have the same parity as the orbitals they are built on and an increase of spin by one per level. For instance, the first rotational band built on the ground state will have spin-parity of 9/2+, the second 11/2+ and so on. For this theory, the correspondence with the experimental results is good. The Nilsson scheme presented here is able to predict, at least, the first three single particle excited states.

4.3.3 Fermium

In the following section the level scheme of the α decay of ^{253}No to ^{249}Fm will be discussed on the background of the experimental data.

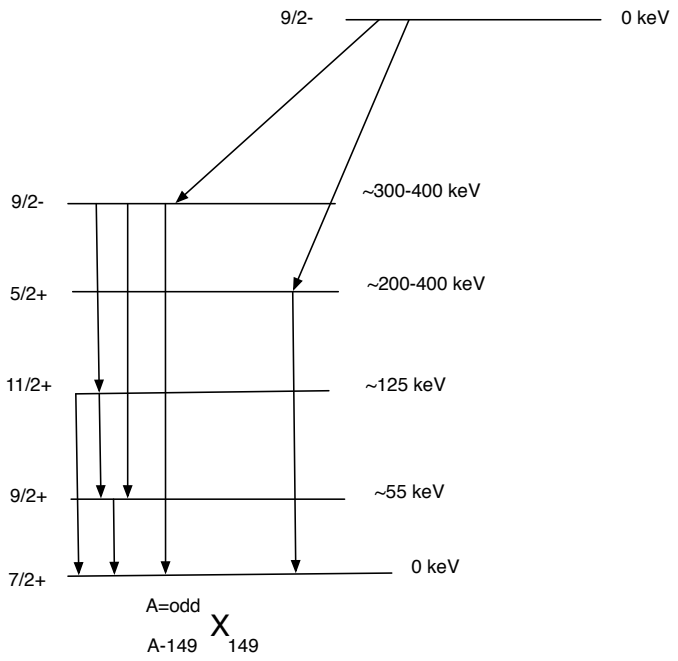

Figure 4.34: Expected levels (populated by α decay) in odd A, N=149 isotones.

Based on the systematics discussed in section 4.3.1, the expected levels with approximate energies are given in Figure 4.34. The transitions from the 9/2- stated are all expected to be $E1$, as was the case for all the isotones discussed. The transition from the first excited state to the ground state is a 9/2+ to 7/2+ transition. As the spin changes with one and there is no parity change, the possible transitions are likely to be $M1$ or $E2$[13]. The transition from the second excited state to the ground state carry a spin of two and no parity change, thus making it a probable $E2$ transition. The de-excitation of the second to the first excited state has a change of spin of one and no parity change; making it a probable $M1$ or $E2$ transition, as also is valid for the decay from the first excited particle state, 5/2+, to the ground state.

The ground state of ^{249}Fm is likely to be the 7/2+[624] orbital by comparing to the systematics. There is experimental evidence also supporting this: looking at the spacing of the ground state bands, see equation (2.6),

[13]The probability of transitions with higher order of polarity become increasingly less likely.

the spin projection fits with a 7/2 state and the relative $M1(E2)$ over $E2$ intensities of the decay from the first and second rotational bands to the ground state agree with theoretical rate estimates given a 7/2+[624] configuration[14]. The ground state in ^{253}No is a 9/2- state. The strongest α decay will feed a state that decays by 3 $E1$ transitions to the members of the ground state bands. This fits well with the observation of a strong α branch to a state which decays by a 279-, 221-, and 150 keV $E1$ transitions.

A low-lying 5/2+ state that decays by a $M1$ transition to the ground state is expected to be seen and is identified as the 209 keV transition. There is a 7/2+ band close (30-60 keV) to the 5/2+ in the other isotones. This 7/2+ state is a rotational band built on the 5/2+ state and does also fed the 5/2+ state. If the band populated is the 7/2+, transitions from the 5/2+ state would also be expected to be seen. As only one transition is seen and in the systematics the 5/2+ state has a higher population than the 7/2+ state, the 209 keV decay is believed to be from a 5/2+ state.

The 670 keV γ line believed to originate from the ^{253}No α decay based on Q-value calculations would correspond to a 3rd single particle excitation of spin-parity 7/2-. This state is present also in ^{247}Cf and ^{245}Cm with similar energy making this a likely identification.

The results are presented in a level scheme in Figure 4.35. The single particle states are in different colors with their rotational bands built on top having the same color. About 90$\pm$14% of the α decays feed the 9/2- state while the feeding of the 5/2+ state occurs approximately 10$\pm$3% of the time. The width of the arrows of the α decay and transitions reflect the strength of the decay. Further, the probability of emission of γ-rays versus conversion electrons are indicated in the figure. The pink section represent γ-ray emission while the peach part shows the number of the decay where conversion electrons are emitted.

Using equation (2.6), the excitation energies of the rotational bands can be calculated. The

$$\frac{\hbar^2}{2\mathcal{I}} \tag{4.15}$$

[14]It it possible to estimate the $M1(E2)/E2$ ratio if the quadrupole deformation of the nucleus and the gyromagnetic factor of the configuration of interest is known. Assuming a deformation standard for the region and a 7/2+[624] ground state (thus using the gyromagnetic factor for this configuration and a spin projection of 3.5) the theoretical mixing ratios obtained are in agreement with the experimentally obtain results.

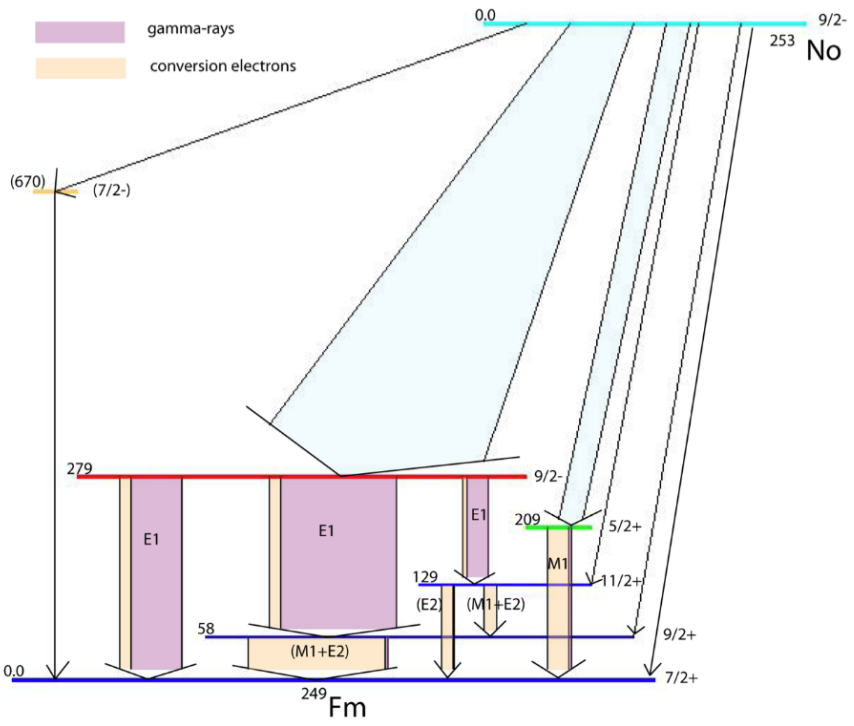

Figure 4.35: Level scheme obtained on the basis of experimental results. The change in color of the states indicate single particle states while the rotational bands built on top of these are of the same color as the band head. The width of the arrows indicated the strength of the transition and the color used inside the arrows, the amount of conversion.

therm is constant for the rotational band built on the same state, and can be calculated by using the energy difference between the ground state and the first excited state. The expected energies of the second, 11/2+, and third, 13/2+, excited rotational bands are found to be at 129- and 212 keV. The 11/2+ state has the same energy as the predicted one. The 13/2+ is of similar energy as the 5/2+ state and would likely decay to the 11/2+ state, a transition of 83 keV. At this energy, no γ peak is detected in the spectrum. This being said, the 13/2+ level would be weakly populated[15] and the transition to the 11/2+ state would probably be a highly converted $M1$ making it unlikely to detect such a γ.

4.3.4 Discussing of systematics and conclusion

In Figure 4.36 the levels in the discussed isotones are plotted. The first two excited states are very similar in all nuclei presented. Further the 5/2+ state and higher excited states in ^{247}Cf are shifted compared to the other isotone. A possible reason for such a shift will be discussed below. The 5/2+ state seen in Fermium is of a lower energy than in the other isotopes, but assuming ^{247}Cf to be a special case and looking at ^{243}Pu and ^{245}Cm, the energy of the state seems to follow the trend: it comes down with increasing proton number. Also the 9/2- state is lowered with higher Z and comes quite a bit down in energy in ^{249}Fm, while the 7/2- state seems to be slightly increasing in energy with added protons.

By looking at the systematics, one can see how the orbits change when more protons are added, and see if and how the gaps in the Nilsson diagram may change. The motivation for experiments like the one discussed in this thesis is to find the Nilsson shell gaps and determine the sequence of orbitals and how this sequence varies with Z and N (on this study the variation in Z was looked at, but N is equally interesting).

When plotting systematics, one can see a shift in ^{247}Cf. The theory is that this shift is caused by a vibrational state that couples to the odd neutron. The vibrational 2^- state is a phonon state caused by the coupling of two protons or two neutrons. In the case of ^{247}Cf, the vibrational state is likely to be caused by the coupling of two protons. The ^{247}Cf isotope has 98 protons, filling the 3/2- orbital. Assuming the Nilsson scheme for protons shown in Figure 4.37 gives a relatively good representation of the real

[15] The 9/2- state does not to any extent feed the 13/2+ state as this would imply an $M2$ transition.

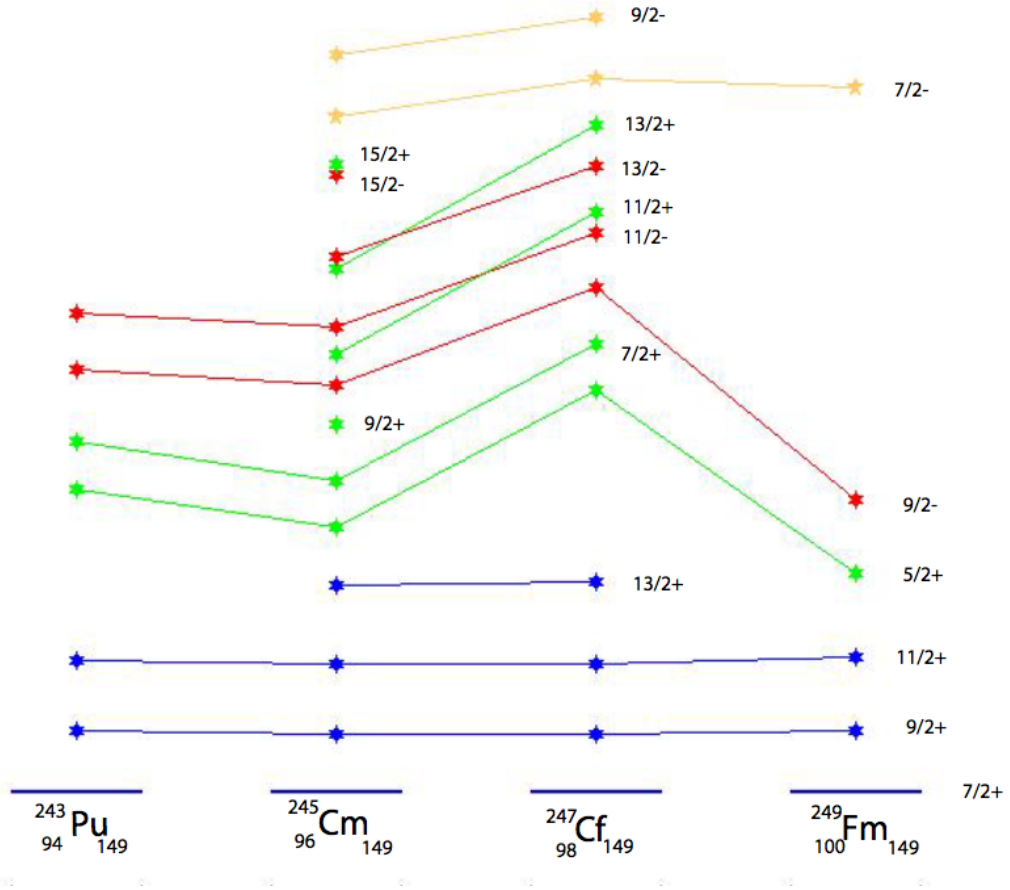

Figure 4.36: A systematic overview of the levels of the 149 isotones discussed. The hight of the levels, marked with stars, are indicative of the energy of the state. Rotational bands are of the same color as the states they are built on. The ground state is marked in blue, the first excited single-particle state in green, second in red and third in yellow [29, 30].

system, the first single particle excitation state, 7/2+ is relatively close in energy to the proton ground state. Thus, single particle excitation to the 7/2+ level is likely, resulting in one particle and one hole in both the 3/2- and the 7/2+ orbitals. A coupling of the protons in these states will create a vibrational 2- phonon state [16]. This vibrational state can couple with the $9/2^-$ state creating $5/2^+$ state:

$$\frac{9}{2}^- + vib(2^-) \rightarrow \frac{5}{2}^+ \tag{4.16}$$

The 5/2+ state resulting from the particle -phonon state coupling interacts with the 'real'[17] single-particle state as they will repel each other due to like spin and parity. Similarly, the interaction of the 5/2+ and the phonon state will upset the positioning of the 9/2- and other related states. This repulsion may explain the shift of the single particle states seen in Figure 4.36.

To try to understand why this can occur in ^{247}Cf and not its neighboring isotones, one must look at the Nilsson schematics for the protons. For californium, with its 98 protons, it will cost less energy to make a vibrational state due to its proton number. Looking at the scheme given in Figure 4.37, as mentioned single particle excitation resulting in a hole and a proton in two orbitals resulting in a 2- vibrational state is likely. In ^{249}Fm, with its 100 protons, this effect will occur at higher energy. In this isotope, levels up to and including the 7/2+ state are filled. A configuration resulting in a 2- vibrational state may be obtained by the excitation of one proton from the 7/2+ state and one proton from the 3/2- state to the 7/2- state, resulting in the excitation of two particles over a large energy gap as such a gap is predicted at Z=100 by the theory used as a basis of the Nilsson scheme. Thus, the creation of this state may only occur at higher excitation energies, and thereby not effect the levels seen.

[16] $\frac{7}{2}^+$ - $\frac{3}{2}^- = 2^-$

[17] The 'single-particle' 5/2+ state is no longer 'pure' single particle state since it just interacted with a particle-phonon state.

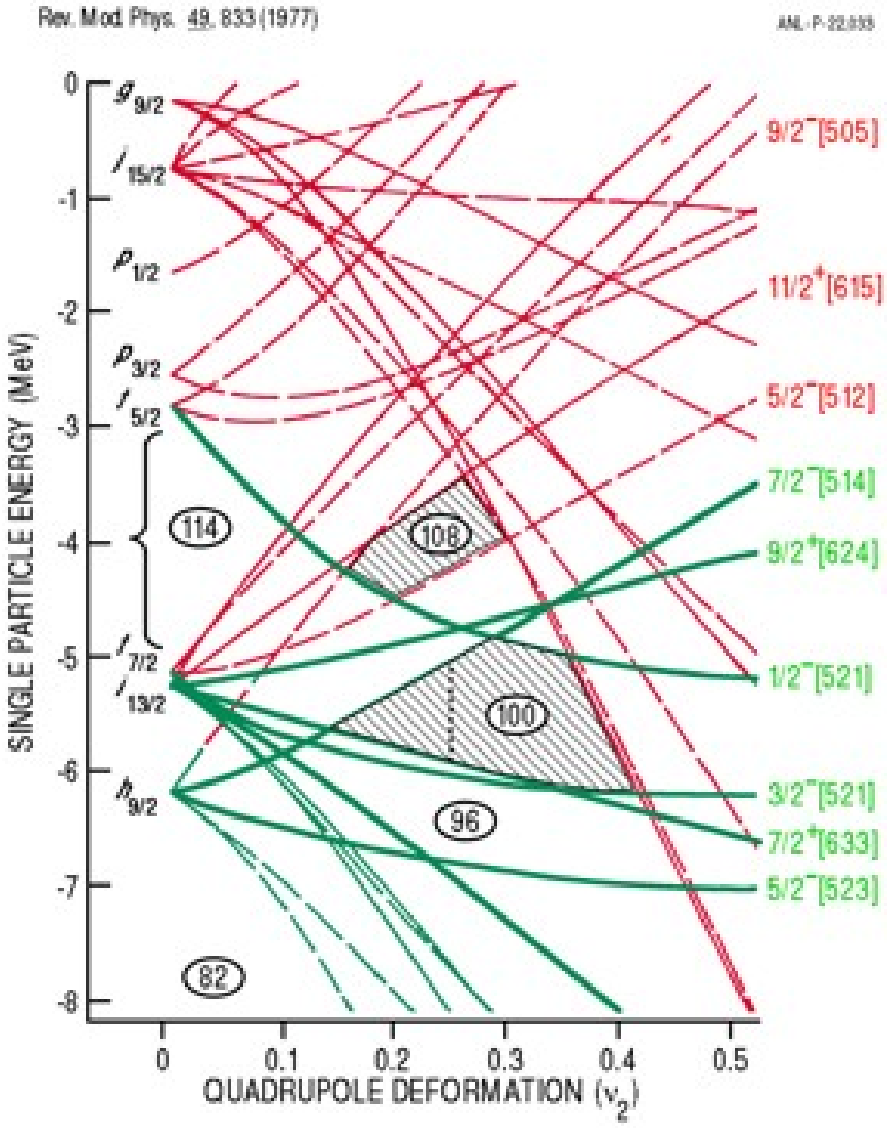

Figure 4.37: Nilsson diagram for the proton range of interest.

Chapter 5

Concluding remarks

To sum up the main results presented in this thesis: the reaction studied is the α decay from ^{253}No to ^{249}Fm. In ^{249}Fm 5 excited states where identified. The rotational band including the 9/2+ and 11/2+ states of energy 55- and 129 keV built on the ground state, and 3 single particle states, a 5/2+ state of energy 209 keV, one 9/2- state at energy 279 keV and a 7/2- state at energy 670 keV were observed. Neither the 5/2+ or the 7/2- state have previously been seen, though the existence of the 5/2+ state had been predicted. The states most strongly fed by the α decay are the 9/2- and 5/2+ states, where the 9/2- state is by far the dominating. Conversion coefficients for the 279-, 221-, 209- and 150 kev LM transitions were determined as well as the K conversion coefficient of the 279 keV. The characters of the transitions were in agreement with earlier results. The results are in accordance with what was expected on the basis of systematics in relevant isotopes.

In conclusion; the level scheme proposed in [3] has been confirmed at a higher statistical level, with the 5/2+ state verified and a new 7/2- state believed identified.

The setup at JINR will over the next few years be further improved, including: a separator upgrade, a bigger focal plane detector and the detector array will be made more compact to maximize photon efficiency and recoil detection. With these improvements, the transmission for ER produced (in very asymmetric reactions) is assumed to be 5-6 times bigger. In future experimentes, the pursuit of the N=149 (and N=151) isotopes further up in Z would be interesting. Also, it would be interesting to try to obtained a better understanding of what is going on in the Californium isotopes as similar accidents as the one discussed for the 149 isotopes are

seen in other Californium nuclei, for instance for energies of single-particle levels in Cf with N=151. In particular the energy of the 5/2+ state reaches its lowest in the isotonic chain. There is some discussion of what the cause of this shift is. The possible explanation given in 4.3.4 is only a theory (though a good one) and may not be the correct explanation. It would be interesting to study Californium isotopes, for example looking at ^{245}Cf and the 147 isotones or ^{249}Cf and the 151 isotones to try to obtain a better understanding of what is happening in structure of Z=98 nuclei.

Appendices

Appendix A

Lifetime determination

The decay probability of nuclear states and half-lives were discussed in section 2.2. The number of decays per unit time is the time derivative of equation (2.8), giving the equation

$$\frac{dN(t)}{dt} = N_0 \lambda e^{-\lambda t} \tag{A.1}$$

The mean lifetime τ or the half-life $t_{1/2}$, is measured by sorting the spectrum into time-intervals, Δt, such that each channel contains the number of decays observed in the time interval $t_i + \Delta t$ after implantation. By using logarithmic time bins where

$$\frac{\Delta t}{t} = constant \tag{A.2}$$

and the change of variables

$$\theta = log_2(t) = \frac{ln(t)}{ln(2)}, \tag{A.3}$$

the number of decays per time bin is given by

$$\frac{dN(\theta)}{d\theta} = N_0 ln(2) \lambda 2^{\theta} e^{-\lambda 2^{\theta}}. \tag{A.4}$$

This equation will peak at θ_{max}, which is related to the lifetime of the state by

$$\tau = 2^{\theta_{max}}. \tag{A.5}$$

Using this variable change, into a logarithmic scale, will make life time determinations in cases of low statistic possible as well as inspection of decay times over a large time interval.

Appendix B

Anomalous conversion coefficients

There are several known cases where the experimental conversion coefficient is larger than the theoretical value for $E1$ transitions in the actinide[1] region [32]. A common feature between the transitions with the anomalous transition was a retardation factor of the γ-ray [33]. A theory of anomalous conversion coefficients was developed by Nilsson and Rasmussen [34]. Calculations of conversion coefficients assume the atomic nucleus to be a point, thus not, among other things, take into account that the atomic electrons can penetrate within the nucleus. The electrons wave function possible existence within the nuclear volume give rise to additionnel terms in the calculation of the conversion coefficient [35]. In general this additional term is smal in comparison with the original expression. In the cases when a transition is retarded, the original expression will be effected making the additional penetration term significant.

Among istopes where anomalous conversion coefficients have been observed are in ^{245}Cm and ^{247}Cf which are of similar structure as ^{249}Fm. In ^{245}Cm the transitions from the 9/2- state to the ground state (7/2+), the first excited state (9/2+) and the second excited state (11/2+) are all anomalous, while there in ^{247}Cf only is the 9/2- state to the ground state, 7/2+, that varies significantly from the theory[2]. This is the same transition as the one in ^{249}Fm that differs from the theoretical value.

[1] $90 \leq Z \leq 103$

[2] Anomalous $E1$ coefficients in the actinide region listen in [32]

Appendix C

Amount of ^{254}No

Figure C.1 shows the α spectrum of the Nobelium isotopes created compared to a simulated ^{253}No spectrum marked with blue squares. As can be seen in the figure, there are parts of the ^{253}No peak experimentally obtained result that are not reproduced by the simulation. This deviation at the right side of the α peak is caused by the production of ^{254}No. By comparison of simulation and experimental results, the amount of ^{254}No produced is about 10% of the total Nobelium peak. The ^{254}No is made from the presence of small quantities of ^{208}Pb in the ^{207}Pb target.

The α peak from the ^{253}No decay has a structure on the top consisting of two maxima. The second peak is caused by summation with electrons in converted decays and the ratio of the peaks is highly dependent on the implantation depth of the ERs. The experimental results where reproduced as seen with an implataion depth of $\sim 2\mu$m.

In the figure, a bump can be seen at channel $\sim$1655 which is also reproduced by the simulations thus being caused by the ^{253}No decay. This is caused by summation of the α decay by a highly converted 209 keV transition as well as summation of electrons/auger/x-rays and α from the decay to the 9/2-state in ^{249}Fm.

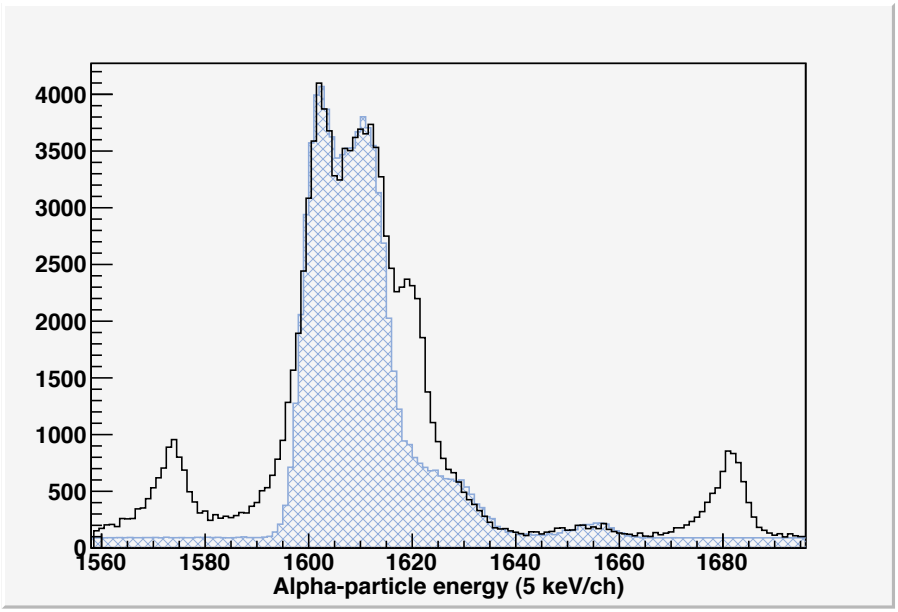

Figure C.1: Simulated and experimental α spectrum. Courtesy of A. Lopez-Martens.

Appendix D

Problems DSSD

In the DSSD used, the area close to the front strips are p-doped and the strips collect the positive charges (holes) while the negative charges (electrons) will drift through the silicium (Si), through the n-doped area to det vertical back-strips. Between the Aluminium strips in the front side of the detector there is insulating material (SiO_2). In this area no net current may flow, giving rise to a positive charge build up at the surface of this area. The positive charge build up is distributed symmetrically about the midpoint of the gap and is sufficient to repel further holes. The potential crated between the front stripes drives the holes to the nearest strip, thus making the probability of all holes collected in one strip high. However, for the collection of electrons problems occur.

There are several aspects of the DSSD detector which gives rise to errors of detected charge. In figure 3.11, horisontal stripes are present on the left side of the diagonal. This is due to charge sharing between the back strips or charge losses in the dead zones on the sides of the detector.

If a demand of just one back and one front signal registered within the coincidence window, Figure D.1 is obtained. The strong horisontal lines previously seen are removed but angled lines become apparent. The slanted lines mean charge loss at the back and the front. This effect is due to the presence of positive charge build-up in the interstrip surface between the front strips. This charge creates a local potential well (it does not go deep into the surface which is why the effect is not visible when ions implant deeply into the detector and why it is such a big effect for heavy nuclei which have little recoil energy and implant shallowly) which may attract and trap all or some of the electrons. The flow of electrons towards the interstrip reduces the signal on the back strip which in turn reduces the

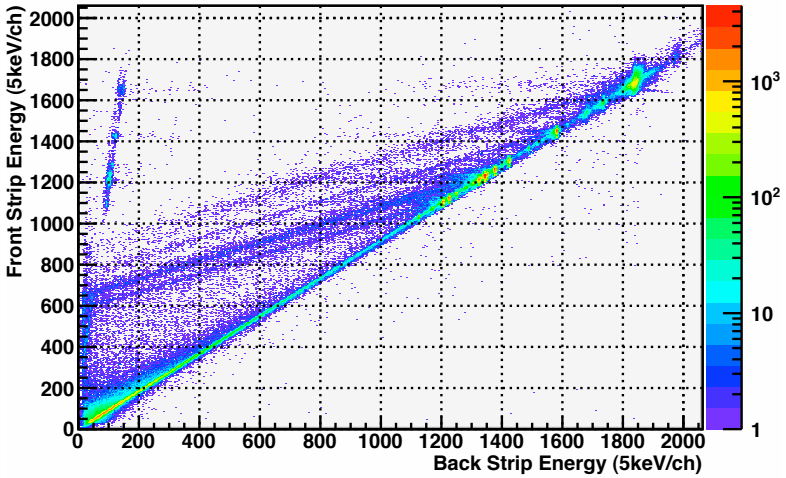

Figure D.1: Plot of the energy detected in the coincident front vs back strips in the case of only 1 front and 1 back strip firing

hole signal on the front strips, [31].

One other problem of not full charge registration arises when charge is deposited close to the side edges in the detector. Here the fields are not linear and charge may be lead out of the detector (to the sides) thus not be gathered in the strips.

In addition to this, when large amount of energy is deposited in the DSSD, the energy detected will be significantly lower than the kinetic energy deposited. This is caused by the large amount of electron-hole pair created. These will shield parts of the electrons and holes from the field resulting in recombination and thus a reduced detected energy. This is particularly valid for the recoils implanted, resulting in an effective energy range extending a little higher than 20-25 MeV and not up to 50 MeV.

Appendix E

ADC

ADC	Name	Description
1	EAm1	Energy from frontdetector 1, strips: 1-15
2	EAm2	Energy from frontdetector 2, strips: 16-31
3	EAm3	Energy from frontdetector 3, strips: 32-47
4	EAm4	Energy from backdetector 1, strips: 1-15
5	EAm6	Energy from backdetector 2, strips: 16-31
6	EAm7	Energy from backdetector 3, strips: 32-47
7	TTOF	Time of flight
8	Veto	Veto compton from shields
9	EAb11	Energy alpha-range, tunnel, side 1
10	EAb12	Energy alpha-range, tunnel, side 2
11	EAb21	Energy alpha-range, tunnel, side 3
12	EAb22	Energy alpha-range, tunnel, side 4
13	EBe11	Energy Beta-range, tunnel, side 1
14	EBe12	Energy Beta-range, tunnel, side 2
15	EBe21	Energy Beta-range, tunnel, side 3
16	EBe22	Energy Beta-range, tunnel, side 4
17	BGO	not used

Table E.1: Assignment of the ADCs used.

ADC	Name	Description
18	Gam1	gammadetector 1
19	Gam2	gammadetector 2
20	Gam3	gammadetector 3
21	Gam4	gammadetector 4
22	Gam5	gammadetector 5
23	Gam6	gammadetector 6
24	Gam7	”shorty”
25	High time	not used
26	ERe1	Energy Recoil, frontdetector 1, strips: 1-15
27	ERe2	Energy Recoil, frontdetector 2, strips: 16-31
28	ERe3	Energy Recoil, frontdetector 3, strips: 32-47
29	ERe4	Energy Recoil, backdetector 1, strips: 1-15
30	ERe5	Energy Recoil, backdetector 2, strips: 16-31
31	ERe6	Energy Recoil, backdetector 3, strips: 32-47
32	ERb11	Energy Recoil, alpha-range, tunnel side 1, coincidence TOF
33	ERb12	Energy Recoil, alpha-range, tunnel side 2, coincidence TOF
34	ERb21	Energy Recoil, alpha-range, tunnel side 3, coincidence TOF
35	ERb22	Energy Recoil, alpha-range, tunnel side 4, coinsidence TOF
36	ERb11	Energy Recoil, Beta-range, tunnel side 1, coincidence TOF
37	ERb12	Energy Recoil, Beta-range, tunnel side 2, coincidence TOF
38	ERb21	Energy Recoil, Beta-range, tunnel side 3, coincidence TOF
39	ERb22	Energy Recoil, Beta-range, tunnel side 4, coincidence TOF
40	MKP1	Time plate 1 of TOF
41	MKP2	Time plate 2 of TOF
42	MKP3	Time plate 3 of TOF
43	MKP4	Time plate 4 of TOF
44	MKP2+4	conisidence MKP2 and MKP4
45	All	rate all detectors
46	Betta	rate in tunnel
47	Dets	rate in Ge

Table E.2: Assignment of the ADCs used, continued.

Appendix F

Level scheme of ^{152}Eu

The long-lived ^{152}Eu nucleus, with a half life of 13.542 years, may decay via β to ^{152}Gd or by EC to ^{152}Sm. β- is the dominant decay form, with a yieal of 72.08 %, while the yield of EC decay is 27.92 % [28]. To predict the transitions likely to be detected by γ-ray spectroscopy, the decay charts, given in Figure F.1, Figure F.2 and Figure F.3, for ^{152}Eu are studied. The β decay giving the highest yields are investigated. The transitions with the highest yields are marked in the level schemes. The strongest γ line seen in the γ-ray spectrum should be 1408 keV $E1$ transition from the 2- state from EC decay. Other strong lines are the 964 ($M1$+$E2$) and 1086($E2$) keV transitions from the 2+ state and 1112($M1$+$E2$) keV transition from the 3+ state in the EC decay and the 779($E1$($M2$)) keV transition from the 3- orbital and the 344($E2$) keV transition from the 2+ state for β decay. In addition to these, from the decay by EC, the lines of energy 867, 444, 1213 and 1458 keV and from the β- decay 1299, 1089 and 411 keV transitions should be seen. The 1089 keV decay is close to the strong 1086 keV transition and may not be distinguishable from the stronger peak.

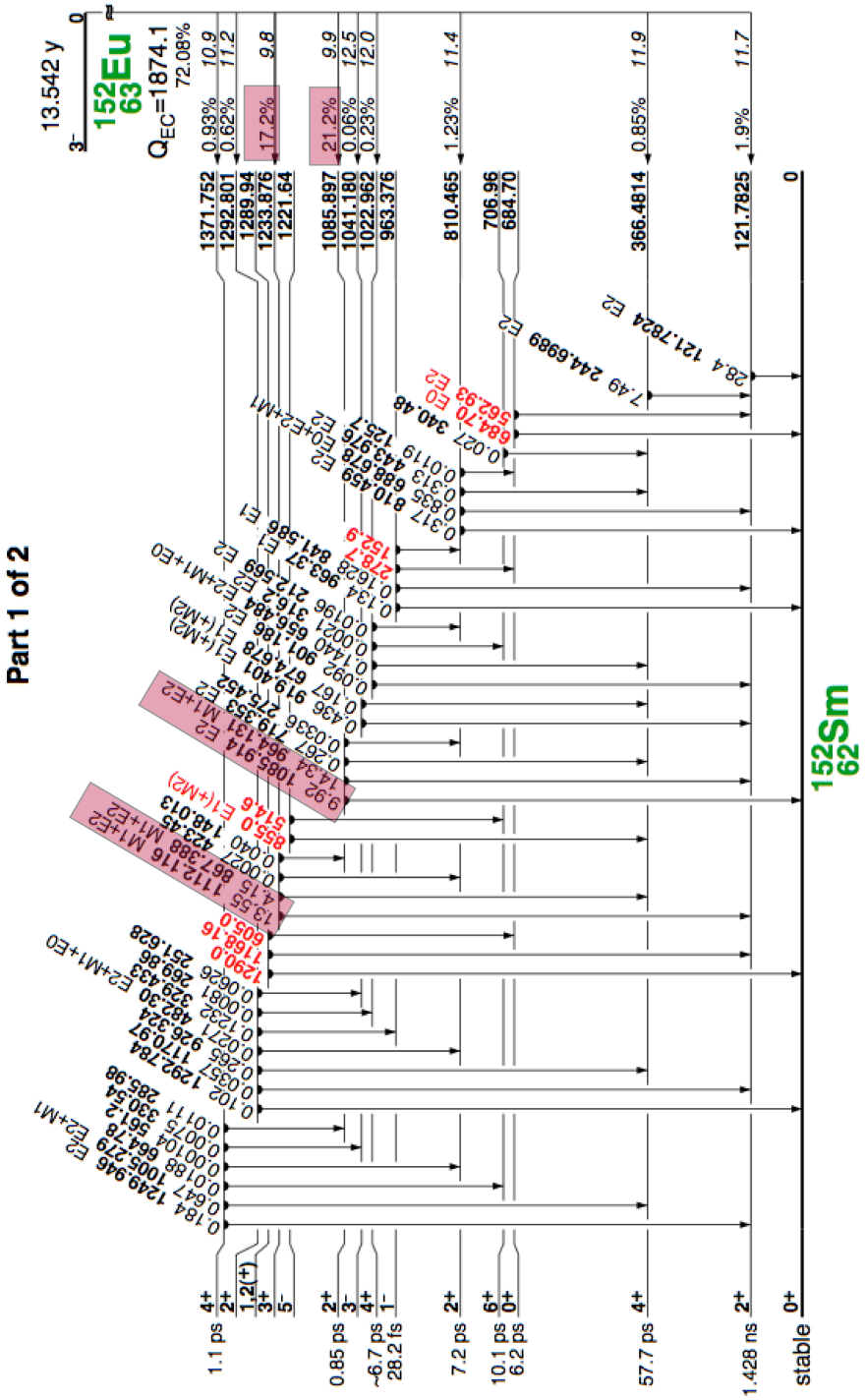

Figure F.1: Level scheme no.1 for ^{152}Eu decay by electron capture [28].

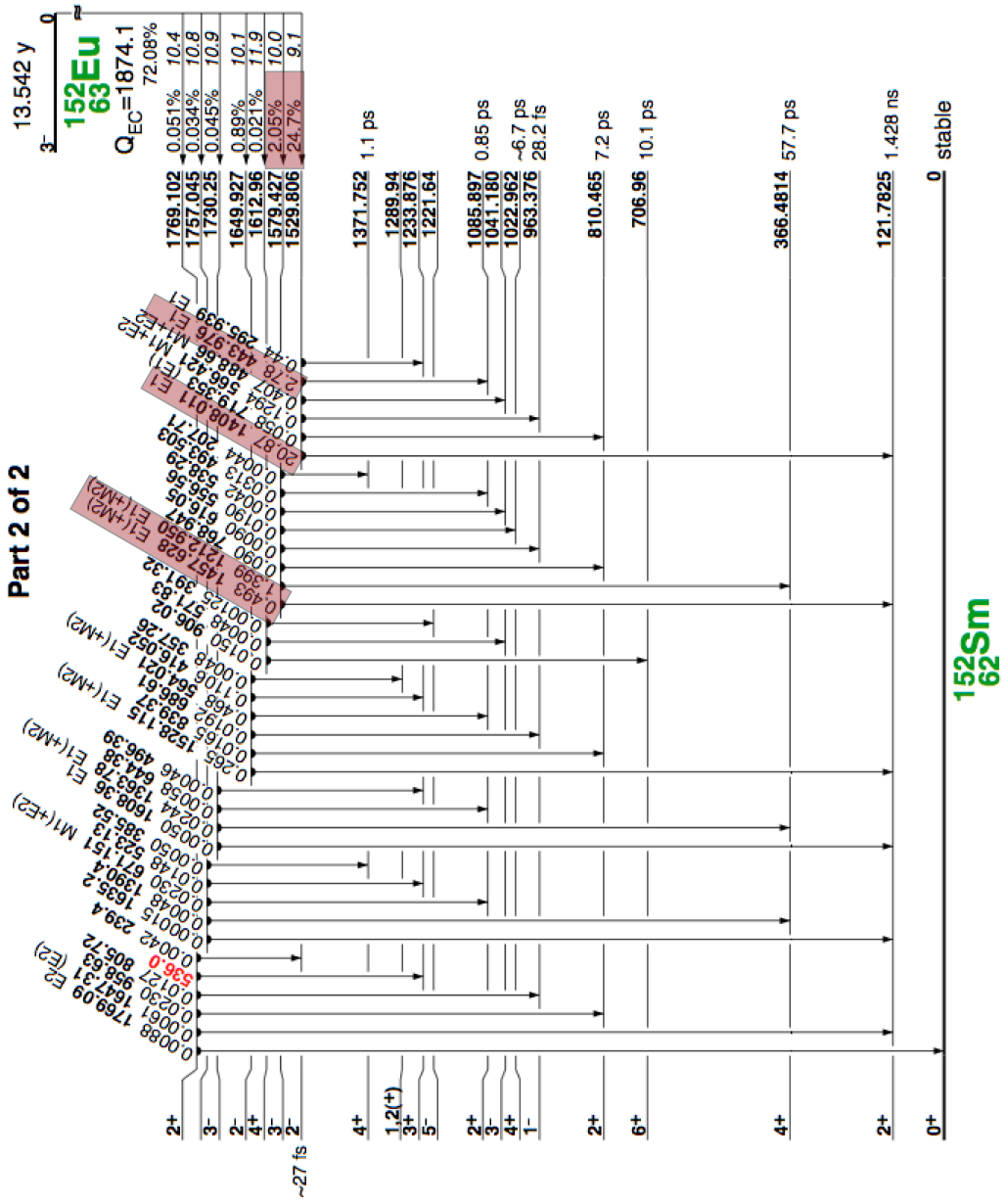

Figure F.2: Level scheme no.2 for ^{152}Eu decay by electron capture [28].

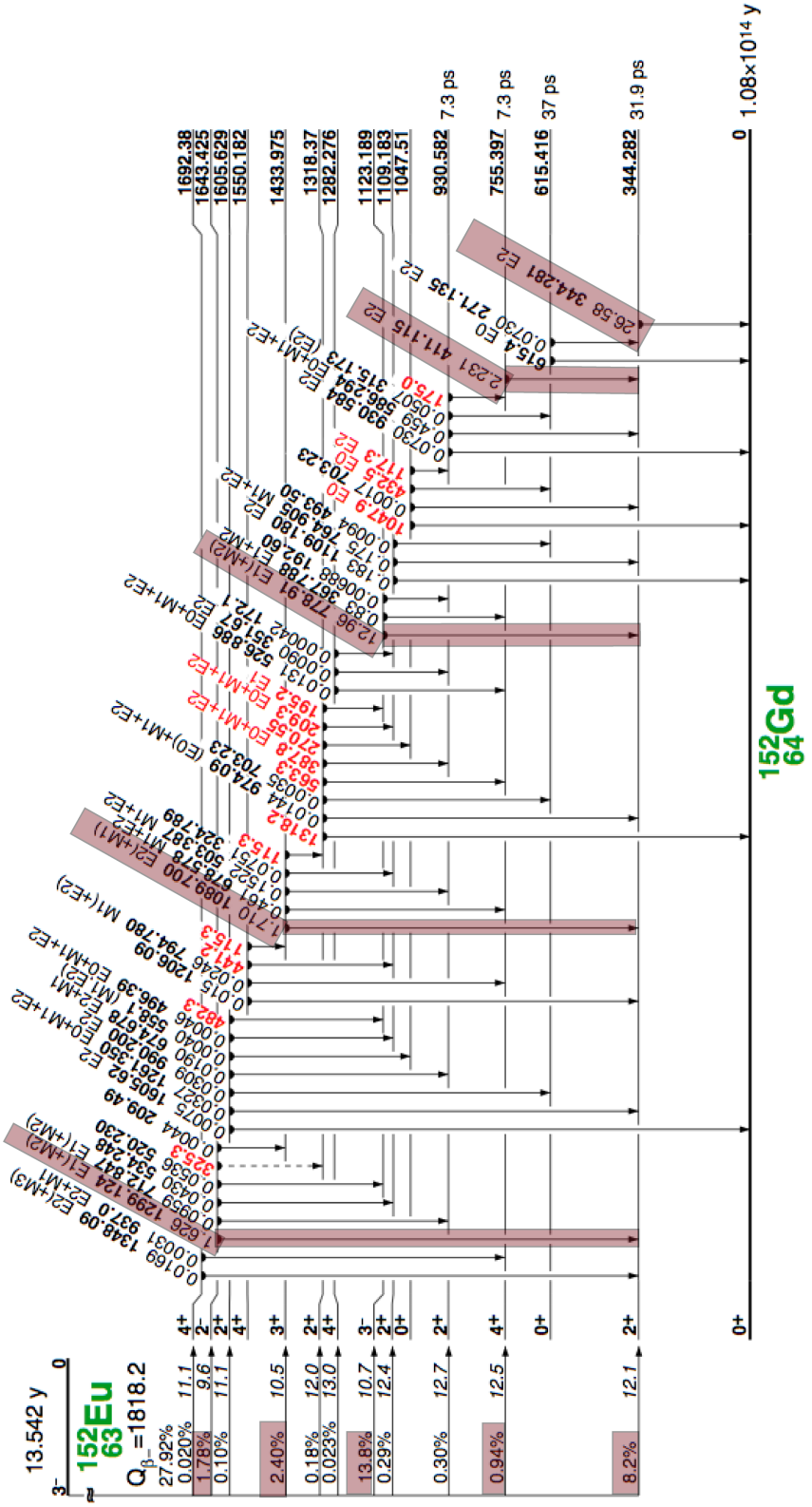

Figure F.3: Level scheme for ^{152}Eu by β- decay [28].

Appendix G

Level-scheme for the ^{211}Po α decay

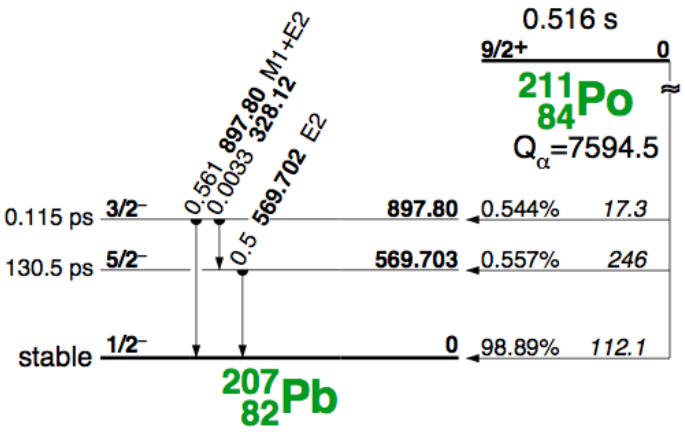

Figure G.1: Level-scheme for the ^{211}Po α decay [28].

Bibliography

[1] Data taken from the NNDC database, http://www.nndc.bnl.gov/masses/mass.mas03

[2] D. Seweryniak *et al.*, Nucl. Phys. A **834**, (2010) 357c

[3] A.Lopez-Martens *et al.*, Phys. Rev. C **74**, (2006) 044303

[4] H. A. Bethe and R.F. Bacher, Rev. Mod. Phys **8**, (1936) 82

[5] C. F. Weizäcker, Z. Phys **96**, (1935) 431

[6] K. S. Krane, *Introductory Nuclear Physics*, John Wiley& Sons, Inc., 1988.

[7] Data taken from the BRICC database, http://physics.anu.edu.au/nuclear/bricc

[8] A.V. Belozerov *et al*, Eur. Phys. J. A **16**, (2003) 447-456

[9] Y. Oganessian *et al*, Phys. Rev. C **64**, (2001) 054606

[10] A.V. Eremin, A.G. Popeko, Physics of Particles and Nuclei, Vol. 35, No. 4, (2004)

[11] K.Hauschild *et al*, NIMA **560**, (2006) 388

[12] ROOT, http://root.cern.ch/drupal/

[13] G.D. Jones, Nucl. Ints. and Meth. A **488**, (2002) 471

[14] A. Lopez-Martes *et al.*, EPJ A **32**, (2007) 245

[15] K.M. Schmidt, EPJ A 8, (2000) 141

[16] I. Dezanka *et al*, PRC **10**, (1974) 766

[17] A.R. Poletti, NPA **440**, (1985), 118

[18] J. Magill, G. Pfennig, J. Galy *Karlsruher Nuklidkarte, Chart of the nuclides* 7^{th} Edition (2006)

[19] R.D Herzberg, J. Phys. G **30**, (2004) R123

[20] Data taken from The Berkeley Laboratory Isotopes Project's - Exploring the Table of Isotopes,
http://ie.lbl.gov/education/isotopes.htm

[21] F. P. Hessberger *et al*, Eur. Phys. J. A, **26**, (2005), 233-239

[22] Bemis *et al* PRC **15**, (1977), 705

[23] A.Ghiorso *et al*, Phys. Rev. Lett. **18**, (1967) 401

[24] J. Kantele, *Handbook of Nuclear Spectrometry* Academic Press Limited (1995)

[25] F. R. Hessberger, Eur. Phys. J. A. **22**, (2004) 417-427

[26] F. R. Hessberger *et al.*, Eur. Phys. J. A **26**, (2005), 233

[27] R.D. Herzberg, P.T. Greenlees, Progress in Particle and Nuclear Physics **61**, (2008) 674720

[28] R.B. Firestone, V. S. Shirley *Table of Isotopes* CD ROM Edition, Version 1.0 (1996)

[29] I. Ahmas *et al* PRC **8**, (1973) 2

[30] W.-D. Schmidt-Ott *et al* Z. Physik, **245**, (1971)

[31] J. Yorkston *et al* NIAM **264**, (1987) 353

[32] R. R. Chasman *et al*, Rev. Mod. Phys. **49**, (1977) 833

[33] F. Asaro *et al*, Phys. Rev. **117**, (1960) 492505

[34] S. G. Nilsson, J. O. Rasmussen, Nuclear Phys. **5**, (1958) 617

[35] E.L. Church, J.Weneser Phys. Rev. **104**, (1956) 13821386

Information from remaning references have not specifically been refered to in the text.

[36] Per Ariasen, Inga Bostad, Steinar Mathisen and Øyvind Rabb. *Lœrebok i filosofi og vitenskapshistorie* Unipub AS, Oslo (2006)

[37] K.H. Lieser *Nuclear and Radiochemistry -Fundamentals and Applications* Second, Revised Edition. WILEY-VCH Verlag GmbH. Weinheim, Germany (2001)

[38] Rolf-Dietermar Herzberg *Spectroscopy of superheavy elements* Topical review, 2004

[39] A.V Yeremin *et al*, *The kinematic separator VASSILISSA preformance and experimental results* Letter to Editor, 28 March 1994

[40] A. V. Yeremin *Regularities of Formation and Survival Probability of Compound Nuclei in the Region of $Z \geq 82$ Study of Copmlete-Fusion Reaction with Heavy Ions Using the Kinematic Separator VASSILISSA* Physics of Particles and Nuclei, Vol.38, No. 4 (2007)

[41] Attix, Frank Herbert *Introduction to Radiological Physics and Radiation Dosimetry*, WILEY-VCH (2004)

[42] H. Park *et al*, Development of Double-Sided Silicon Strip Position Sensor -IEEE Nuclear Science Symposium Conference Record, (2005) N14-174

[43] Greenwood, Norman N *Recent developments concerning the discovery of elements 101-111* Pure &Appl. Chem.,Vol 69, No. 1, (1997) pp. 179-184

[44] W.R. Leo *Techniques for Nuclear and Particle Physics Experiments 2. Revised Edition* Springer-Verlag Berlin Heidelberg, Germany (1987, 1994)